Institut für Erd- und Umweltwissenschaften
Geophysik

Detection and Kirchhoff-type migration of seismic events by use of a new characteristic function

Dissertation

zur Erlangung des akademischen Grades
"doctor rerum naturalium"
(Dr.rer.nat.)
in der Wissenschaftsdisziplin "Geophysik"

eingereicht an der
Mathematisch-Naturwissenschaftlichen Fakultät
der Universität Potsdam

von
Andri Hendriyana

Potsdam, Juli 2017

Published online at the
Institutional Repository of the University of Potsdam:
URN urn:nbn:de:kobv:517-opus4-398879
http://nbn-resolving.de/urn:nbn:de:kobv:517-opus4-398879

Abstract

The classical method of seismic event localization is based on the picking of body wave arrivals, ray tracing and inversion of travel time data. Travel time picks with small uncertainties are required to produce reliable and accurate results with this kind of source localization. Hence recordings, with a low Signal-to-Noise Ratio (SNR) cannot be used in a travel time based inversion. Low SNR can be related with weak signals from distant and/or low magnitude sources as well as with a high level of ambient noise. Diffraction stacking is considered as an alternative seismic event localization method that enables also the processing of low SNR recordings by mean of stacking the amplitudes of seismograms along a travel time function. The location of seismic event and its origin time are determined based on the highest stacked amplitudes (coherency) of the image function. The method promotes an automatic processing since it does not need travel time picks as input data.

However, applying diffraction stacking may require longer computation times if only limited computer resources are used. Furthermore, a simple diffraction stacking of recorded amplitudes could possibly fail to locate the seismic sources if the focal mechanism leads to complex radiation patterns which typically holds for both natural and induced seismicity.

In my PhD project, I have developed a new work flow for the localization of seismic events which is based on a diffraction stacking approach. A parallelized code was implemented for the calculation of travel time tables and for the determination of an image function to reduce computation time. In order to address the effects from complex source radiation patterns, I also suggest to compute diffraction stacking from a characteristic function (CF) instead of stacking the original wave form data. A new CF, which is called in the following mAIC (modified from Akaike Information Criterion) is proposed. I demonstrate that, the performance of the mAIC does not depend on the chosen length of the analyzed time window and that both P- and S-wave onsets can be detected accurately. To avoid cross-talk between P- and S-waves due to inaccurate velocity models, I separate the P- and S-waves from the mAIC function by making use of polarization attributes. Then, eventually the final image function is represented by the largest eigenvalue as a result of the covariance analysis between P- and S-image functions. Before applying diffraction stacking, I also apply seismogram denoising by using Otsu thresholding in the time-frequency domain.

Results from synthetic experiments show that the proposed diffraction stacking provides reliable results even from seismograms with low SNR=1. Tests with different presentations of the synthetic seismograms (displacement, velocity, and acceleration) shown that, acceleration seismograms deliver better results in case of high SNR, whereas displacement seismograms provide more accurate results in case of low SNR recordings. In another test, different measures (maximum amplitude, other statistical parameters) were used to determine the source location in the final image function. I found that the statistical approach is the preferred method particularly for low SNR.

The work flow of my diffraction stacking method was finally applied to local earthquake data from Sumatra, Indonesia. Recordings from a temporary network of 42 stations deployed for 9 months around the Tarutung pull-apart Basin were analyzed. The seismic event locations resulting from the diffraction stacking method align along a segment of the Sumatran Fault. A more complex distribution of seismicity is imaged within and around the Tarutung Basin. Two lineaments striking N-S were found in the middle of the Tarutung Basin which support independent results from structural geology. These features are interpreted as opening fractures due to local extension. A cluster of seismic events repeatedly occurred in short time which might be related to fluid drainage since two hot springs are observed at the surface near to this cluster.

Abstract

Klassische seismologische Verfahren zur Lokalisierung seismischer Ereignisse basieren auf der Bestimmung der Ankunftszeiten von Raumwellenphasen, der Berechnung von Strahlwegen in Untergrundmodellen sowie der Inversion der Laufzeitdaten. Um mit dieser Methode zuverlässige und genaue Lokalisierungsergebnisse zu erhalten, werden Laufzeitdaten mit kleinen Unsicherheiten benötigt. Folgerichtig müssen Seismogramme mit sehr geringen Signal-zu-Rausch Verhältnissen (S/N) häufig verworfen werden. Geringe S/N können einerseits durch schwache Signale am Empfänger, z.B. wegen großer Entfernungen zur Quelle und/oder bei Quellen mit kleiner Magnitude, und andererseits durch einen hohen Rauschpegel verursacht werden.

Eine alternative Methode zur Herdlokalisierung ist die sogenannte Diffraktions-Stapelung. Hierbei werden die Amplituden der aufgezeichneten Wellenformen entlang von vorhergesagten Laufzeitfunktionen aufgestapelt. Durch konstruktive Aufsummation können auch Signale von Seismogrammen mit geringem S/N zur Lokalisierung beitragen. Als Teil des Verfahrens wird eine sogenannte Image-Funktion berechnet, deren maximale Amplitude (Kohärenz) mit dem Ort und der Zeit des Bebenherdes verknüpft ist. Die Methodik ist für eine Implementation von automatisierten Überwachungssystemen geeignet. Von Nachteil ist der relative hohe Rechenaufwand. Außerdem müssen bei der Diffraktions-Stapelung die komplizierten Abstrahlcharakteristika im Quellbereich und deren Auswirkungen auf die Signale an verschiedenen Empfängern im Unterschied zur Laufzeit-Inversion mit berücksichtigt werden.

In meiner Arbeit habe ich eine neue Methodik zur Lokalisierung von Bebenherden unter Verwendung einer Diffraktions-Stapelung entwickelt. Zunächst werden Laufzeiten (Green's Funktionen) für potentielle Herdlokationen mit Hilfe eines parallelisierten Algorithmus berechnet. Eine erste Vorbearbeitung der Seismogramme mit der Otsu-Thresholding Methode im Zeit-Frequenz-Bereich dient zur Unterdrückung von nicht-stationären Rauschanteilen. Anschliessend wird eine neu entwickelte charakteristische Funktion (CF) berechnet, um P- und S-Welleneinsätze in den gefilterten Daten noch stärker hervorzuheben. Die vorgeschlagene CF basiert auf einer modifizierten Version des Akaike Kriteriums. Die neue CF liefert stabile Resultate, die im Unterschied zum klassischen Akaike-Kriterium nicht von der subjektiv festzulegenden Länge des Analysefensters abhängig sind. Die Verwendung der CF ist darüber hinaus entscheidend, um den unerwünschten Einfluss der

Abstrahlcharakteristik auf die gemessenen Amplituden bei der Diffraktions-Stapelung zu eliminieren. Eine finale Image-Funktion wird mit Hilfe einer Kovarianzmatrix-Analyse von P- und S- Image-Funktionen bestimmt, um daraus schließlich die Herdlokation zu ermitteln.

Das neue Verfahren wird an Hand von synthetischen Daten getestet. Zuverlässige und genaue Resultate konnten selbst bei sehr geringen S/N von 1 erzielt werden. Tests mit verschiedenen Seismogramm-Varianten (Verschiebung, Geschwindigkeit, Beschleunigung) ergaben, dass bei hohem S/N Beschleunigungs-Seismogramme und bei sehr niedrigen S/N Verschiebungs-Seismogramme die besten Ergebnisse lieferten.

Schliesslich wurde das Verfahren auf Daten aus einer Lokalbebenuntersuchung auf Sumatra (Indonesien) angewendet. Über einen Zeitraum von 9 Monaten wurde mit einem Netzwerk aus 42 Stationen die Seismizität im Bereich des Tarutung-Beckens an der Sumatra-Störung (SF) erfasst. Die Methode bildete hierbei ein lineares Segment der SF ab. Im Tarutung-Becken wurde eine komplexere Bebenverteilung abgeleitet. Ein Vergleich mit strukturgeologischen Daten liefert Rückschlüsse auf das tektonische und geothermische Regime im Untersuchungsgebiet.

Contents

Chapter 1

Introduction

1.1 Background

Most earthquakes do not occur in random locations, but are distributed around plate boundaries. The occurrence of earthquakes at plate boundaries is considered as energy-releasing due to strain accumulation related to plate motion. In general, a relatively large amount of energy is released by earthquakes associated with tectonic stress since the rupture interfaces may extend over large areas within the lithosphere. For example, the 26 December 2004, Sumatra-Andaman Earthquake which had a moment magnitude of 9.15, released an energy equivalent to 6.5×10^{22} Newton·meters (Park et al., 2005), and ruptured the 1600 km Sunda megathrust, slab interface between the Indo-Australian and Eurasian plates (Lay et al., 2005). Besides the Sunda megathrust, there is another important seismogenic zone in the overriding plate in the middle of Sumatra Island due to the right-lateral movements and strike-slip deformation along the Sumatran Fault (SF). Although the crustal earthquakes occurring in this area are in general of smaller magnitude compared with seismicity at the Sunda megathrust, the potential damages could be disastrous as well since the Sumatran island is highly populated and earthquakes occur at shallow depths.

The detection and localization of earthquakes is one of the major tasks in seismology. Seismicity maps representing a distribution of earthquakes can be useful in identifying and delineating active faults, particularly when these are not exposed at the surface. Furthermore, the identified faults, may be included in the assessment of potential hazards in a particular area. On a local scale, local seismicity recorded by a dense network of

stations can be used to accurately determine the location of seismic sources occurring within the crust under the network. To give some examples, the distribution of seismic events have been used to image complex crustal structures of the equatorial bifurcation at the SF (Weller et al., 2012) and duplex fault structures within the Tarutung Basin located some 100 km further north (Muksin et al., 2014). Observation and precise mapping of seismicity provides important information on the behavior of volcanoes. One example for such applications is the monitoring of magma ascent (Houlié & Montagner, 2007). There is also a considerable potential to make benefit from seismicity mapping in relation with the monitoring of geothermal and hydrocarbon reservoirs. For example, Julian et al. (2007) considered microseismicity to improve the understanding of physical processes accompanying fluid injection into a geothermal reservoir. Various applications of passive seismic monitoring and seismicity mapping in geothermal exploration are discussed in Duncan & Eisner (2010). However, extracting information from seismicity distributions is reasonable and efficient only if methods for a reliable and precise event localization are available.

A first requirement for reliable and accurate event detection and localization is the usage of dense networks with a sufficient coverage. For this purpose, the seismometers have to be installed at the surface rather than in boreholes. In addition, local earthquakes usually have low magnitudes. Seismic events with magnitudes smaller than 0 are usually found in the passive seismic monitoring of the Carbon Capture and Storage (CCS) projects (Takagishi et al., 2014). These two factors–the limited number of surface seismometers, and the low magnitudes of seismic events–result in a significant challenge to the processing of recorded seismograms due to low quality data. In case of low magnitude seismicity, high quality seismograms could be recorded only by borehole seismometers which eventually enable one to locate a seismic event accurately.

The classical method or the travel-time based methods rely on the information of the first arrival of seismic waves (both P and S), which are either extracted manually or automatically from the registered seismograms. The location and origin time of earthquakes are determined by minimizing the residual between observed and computed arrival times (i.e., Waldhauser & Ellsworth, 2000; Lomax et al., 2000) by using inversion. In case of low data quality, the classical seismic event location method may produce insufficient results, as arrival times of P and S phases are difficult to determine.

Migration-based seismic event localization methods are solutions to this problem which is used to deal with seismic data with obscured onset of arrival times as these methods do not require arrival time picks. These methods work well even for data sets with very low Signal-to-Noise Ratio (SNR) (Gajewski & Tessmer, 2005; Chambers et al., 2010). It has been shown that the accuracy of seismic event location derived from surface seismometers can be as accurate as those derived from borehole seismometers when both a dense network of surface seismometers and migration-based localization methods are applied as a tool to increase the SNR(Lakings et al., 2006).

In general, there are two typess of migration-based seismic event localization methods: the time-reverse migration (Gajewski & Tessmer, 2005) and the Kirchhoff-like diffraction stacking methods (Gajewski et al., 2007). A diffraction stacking method was selected to represent a more general term including source-scanning algorithm (SSA) (Kao & Shan, 2004, 2007). The SSA method is well-suited for locating seismic events from seismic tremor recordings which are characterized by an unclear onset of body waves. The source distribution of the tremors was successfully inferred from the four-dimensional image function, known as the brightness function (coherency-like). The diffraction stacking method exploits waveforms by measuring the coherency (i.e. semblance, stacking, and median) of waveforms along the theoretical arrival time. For a two-dimensional homogeneous velocity model this coherency operator is represented by a diffraction curve. The highest coherency is related with the location of a seismic event.

As described by the scaling law (Gutenberg & Richter, 1954), for each event with a large magnitude there will be number of smaller events which increase exponentially. Hence, the targeting of a local events by deploying a dense seismic network leads to the recording of countless events with low magnitudes and with relatively low SNR. To deal with this kind of data, a diffraction stacking will be considered as a promising technique and will be discussed in more detailed in this thesis.

The diffraction stacking method discussed in this thesis is characterized by following:

- The method does not require the picking of arrival times, therefore the diffraction stacking is well-suited for automatic seismic event localization.

- An automatic localization enables one to process large amounts of seismic data (Hansen & Schmandt, 2015).

- The method considers a three-dimensional velocity model.

1.2 Motivation

The application of a migration-based seismic event localization requires more computer resources than the classical localization method affords. There are several reasons why this method is working much more time consuming. One reason is that the coherency has to be calculated for all potential nodal points and origin times in a discretized spatial and temporal domain. The spatial domain corresponds to the subsurface model and the temporal domain is associated with the recording time of the seismograms. Another reason for the high processing power demand is that the coherency is calculated along a coherency or stacking operator which depends on the travel time function which is also called Green Function Table (GFT). To increase the calculation speed, a processor parallelization is implemented in the GFT computation code in this study by using the Message Parallel Interface (MPI) library.

By applying amplitude stacking, the SNR of considered waveforms will be improved as random noise stacks destructively while coherent signals stack constructively. However, practitioners of reflection seismic processing, usually apply random noise filtering prior to applying the amplitude stacking. The need for pre-processing of passive seismic data is more important in case of local passive seismic data because of relatively low SNR related with weaker signals and degrading influence of anthropogenic noises. A particular effect which has to be considered in the pre-processing (filtering) of passive seismic data is related with the relatively long time windows to be filtered. The length of the time window should cover P and S phase arrivals. Compared with active seismic reflection experiments, the observation distances between sources and receivers can be quite large within passive seismic networks, which leads to longer time delays between P and S phases. As a consequence, time windows of data processing including filtering must be chosen relatively long. This, again, requires filtering methods which considers the non-stationary properties of the time series to be filtered. In my work I applied the Otsu thresholding (Otsu, 1979) for the filtering of the non-stationary data before the diffraction stacking is carried out. To apply this filtering technique the original data have to be transformed to the time-frequency domain by using the S transform (Stockwell et al., 1996).

Another aspect which has to be considered in the diffraction stacking of passive seismic data is the influence of the earthquake source radiation pattern on the signals to be stacked. In seismic reflection data, for which the diffraction stacking was developed, the signals to be stacked are generated by approximately isotropic sources such as hammer, explosions or vibroseis. After application of different processing steps such as static corrections and amplitude corrections, the signals are rather comparable and can be stacked by simple mean or other statistical methods. In passive earthquake seismic recordings a much more complex source mechanism has to be assumed. The double-coupe (DC) source model is an approximation model representing the actual force radiated by an earthquake source. In addition, some seismic events have a significant amount of non-DC component if the fault plane is not planar. The non-DC component can be found for example in seismic events recorded in a volcanic area (Julian, 1983). A source model of passive seismic may be well represented by a mixture of explosion/implosion, DC and compensated linear vector dipole (CLVD) (Vavryčuk, 2015) which further leads to the variation of phase polarities and amplitudes at the onset of P and S waves. In such case, the coherency (semblance, stacking, and median amplitudes) computed from the recorded seismogram will be low (Staněk et al., 2015). In a pure DC source model, the resultant stacking amplitude may be zero, caused by the cancellation of positive and negative polarities (Zhebel, 2013).

Numerous techniques of computing coherency which consider the source radiation pattern of passive seismic data have been suggested, such as pair-wise cross-correlation (Zhebel, 2013). Anikiev et al. (2014) conducted automatic moment tensor inversion prior to stacking the amplitudes; hence the stacking was applied to the corrected polarity onset of the P wave. Avoiding low coherency values can also be achieved by transforming the seismogram amplitudes to a characteristic function. Kao & Shan (2007) employed stacking to the absolute amplitude of seismogram. An envelope of amplitudes was also used by Kao & Shan (2007) and Gharti et al. (2010). Other characteristic functions were also proposed to highlight the onset of P or S waves such as Short-term amplitude to long-term amplitude (STA/LTA) ratio (Grigoli et al., 2013, 2014; Hansen & Schmandt, 2015) and kurtosis (Langet et al., 2014). In this thesis I have used a new characteristic function modified from the Akaike Information Criterion (AIC) (Maeda, 1985),termed the modified AIC (mAIC).

In order to improve the accuracy of seismic event locations, coherency may be calculated from both P and S waves, either separately or simultaneously. Gharti et al. (2010) computed the coherency simultaneously from seismograms in the LQT coordinate system. The P velocity model was used to compute the coherency of L-component seismograms, while the coherency of the Q and T components was computed using the S velocity model, since these contained SV and SH components, respectively. The final coherency was a result of summing up the coherency of the three components LQT of the seismograms. In another approach, Grigoli et al. (2013) suggested multiplying the coherency computed from P and S components. Transforming the seismogram into ray coordinate LQT requires knowledge of the back-azimuth and incident angle. These two angles should be computed for each grid point as they are potential source locations. If the computed angles contain large uncertainties (caused by noises or complex velocities), the separation of P, SV, and SH would not be optimal. Hence in this thesis, the P and S waves were treated separately in computing the coherency. The final coherency was obtained from the covariance analysis of the P and S coherency functions. The P and S wave signals were derived from the mAIC characteristic function in combination with attributes from polarization analysis such as rectilinearity and angle of incidence.

In summary of this introduction, the following workflow for a seismic event localization is proposed in my thesis:

1. Generate the GFT based on P and S wave velocity models using a parallelized code.

2. Denoise the seismograms in the time-frequency domain using Otsu Thresholding.

3. Transform the filtered seismograms to the P- and S- characteristic functions by using a modified AIC function and polarization attributes.

4. Compute the image function or the coherency of the P and S characteristic functions.

5. Calculate the final image function by applying covariance analysis between P- and S- image functions.

6. Estimate the seismic event location by applying the maximum value of image function (Gajewski et al., 2007; Chambers et al., 2013; Grigoli et al., 2013) or, alternatively, by using a statistical approach (Anikiev et al., 2014).

The performance of the proposed diffraction stacking procedure was then evaluated by analysis of synthetic seismograms. Moreover, the method was applied to local earthquake data collected around the Tarutung Basin at the Sumatran Fault in Indonesia. The results from Tarutung were finally compared with those resultant from the classical seismic event localization method.

1.3 Structure of the thesis

In chapter 2, the methodology of the proposed workflow is described. Different methods for the filtering and denoising of the original seismograms are described. A key step in the workflow is the introduction of a new characteristic function which is used as the input signal for the stacking. Finally, the approach for the event localization is presented in this chapter. Chapter 3 is demonstrating the application of the workflow to synthetic data. A hypothetic experiment was assumed and synthetic data were generated in order to test the performance of the algorithm under known conditions. Different strategies and different parameters in the subsequent steps of the workflow are tested and discussed in this chapter. Chapter 4 is showing the application of the method to real data from Indonesia. The data set was collected within the framework of a German-Indonesian scientific cooperation on geothermal exploration and exploitation technologies. Local earthquake tomography was applied to study the velocity structure and the seismicity distribution within a tectonically active region at the Sumatran Fault. The method developed in this thesis is applied to this data set and the seismicity distribution derived by the new approach is compared with a classical inversion for velocity structure and seismic event location. In chapter 5, the methodology and results from the application of the approach are discussed. In the first part, different aspects of the workflow are considered based on the tests with synthetic data. In the second part, the results from the Tarutung data set are evaluated. The seismicity distribution derived by the new method is discussed together with the velocity structure and in relation to the distribution of geothermal manifestations in the target region.

Chapter 2

Methods

The S-transform denoising approach, the characteristic function, and the diffraction stacking method for seismic event localization will be discussed in this chapter. The main objective of seismogram denoising is to increase the Signal-to-Noise ratio (SNR) by reducing random and environmental noises from the recorded seismogram so that the information of the arrival of direct waves can be revealed. As a result, the SNR of the seismogram is improved, particularly around the onset of waves, and might lead to more accurate seismic event location. The imaging methods apply the amplitude stacking of the registered seismogram recorded across the seismic network. Then, in principle, random noises could be reduced by the application of this amplitude stacking in the imaging process. However, to achieve an effective stacking, an accurate velocity model is required. Due to the poor knowledge of velocity model, signals may not constructively interfere. The seismogram denoising also can be regarded as a data pre-conditioning before the employment of imaging technique.

Noises and signals are often separated in the frequency domain. However, since signals show non-stationary behavior, it is critical to consider the time-frequency representation of a signal rather than only its frequencies. In this study, the denoising of the recorded seismograms will be conducted using the so-called Otsu thresholding (Otsu, 1979).

Another representation of seismograms is the characteristic function, which allows us to perform automatic seismic event location by means of diffraction stacking. In this chapter, the so-called modified Akaike Information Criterion (mAIC) will be introduced. The proposed characteristic function does not depend on the length of the seismogram window and can be used to simultaneously identify P- and S- waves.

Diffraction stacking is a migration-based seismic event localization technique that can be used for various types of data, such as tremors (Kao & Shan, 2004), mining operation-induced seismicities (Gharti et al., 2010), volcanic events (Langet et al., 2014), and local earthquakes (Grigoli et al., 2014).

2.1 Seismogram denoising

In field surveys, passive seismic data will always be affected by random noise. On the other hand, reducing random noise from signals (denoising) is particularly challenging because of the nature of the passive seismic data. In most cases, noise and signals are well separated in the frequency domain; hence, frequency-domain filtering is commonly used in denoising. In this chapter, I discuss a denoising method that applies Otsu thresholding (Otsu, 1979) to the magnitude of time-frequency representation of seismograms.

2.1.1 Frequency representation of seismograms

The passive seismic data consist of multiphase seismic signals propagating at different frequencies. Because each seismic phase travels with different velocities, the seismic signals arrive at the seismometer at different times, causing the frequency component of the seismogram to vary significantly with time. Obviously, this non-stationary characteristic of the seismogram cannot be captured by using a traditional signal analysis tool, such as Fourier Transform (FT). FT is only well-suited for stationary signals, which will never occur in passive seismic data. A means of estimating the time-localized frequency spectra of a signal is by employing short-time Fourier Transform (STFT), as described by Schafer & Rabiner (1973). With this method, we can divide the original seismogram into smaller segments and then apply STFT to all segments, using the following equation:

$$X_{STFT}(\tau, f) = \int_{-\infty}^{\infty} x(t)\overline{w}(t-\tau)\exp\left[-i2\pi f t\right] dt \tag{2.1}$$

where $\overline{w}(t)$ is the complex conjugate of a window function $w(t)$. The window function has a constant window size across the seismogram records. The window function is moving over the signals as it is translated by factor τ. Although this method works well in transforming seismograms to their time-frequency representation, the use of a constant window size introduces a resolution problem: how to balance a reasonable resolution in

both the frequency and time-domain simultaneously. A good resolution in the frequency-domain is typically obtained by using a large window size, while a small window size is needed for better resolutions in the time-domain. Hence, the optimum window size should be selected by finding the best compromise between the time and frequency-domain resolutions.

To address the fundamental trade-off between time and frequency resolutions, another tool was proposed, known as wavelet transform (WT) (Daubechies, 1990). In this method, a wavelet function, $\psi(t)$, is used as the window function. The shape of the wavelet is adjusted by a scale factor (dilation), σ. Similar to the window function in the FT, the wavelet function moves over the signal, so that the wavelet also has a translation factor τ. The WT can be expressed in the following equation:

$$X_{WT}(\tau,\sigma) = \int_{-\infty}^{\infty} x(t)\frac{1}{\sqrt{\sigma}}\overline{\Psi}\left(\frac{t-\tau}{\sigma}\right)dt \tag{2.2}$$

Please note that the dilation factor somewhat represents the inverse of frequency. When $\sigma < 1$, it leads to a compressed wavelet (i.e., high frequency wavelet), and when $\sigma > 1$, the wavelet is stretched (low frequency wavelet).

Another method, the S- transform (Stockwell et al., 1996), takes advantage of both STFT and WT by measuring local frequency as in STFT and by providing an improved resolution as offered by WT. Equation 2.3 describes the mathematical expression of the S-transform:

$$S(\tau,f) = \int_{-\infty}^{\infty} x(t)\frac{|f|}{\sqrt{2\pi}}\exp\left[-\frac{(\tau-t)^2 f^2}{2}\right]\exp\left[-i2\pi ft\right]dt \tag{2.3}$$

In this method, the continuous $x(t)$ function (i.e., seismogram) is transformed into a complex S-spectrum (or wavelet coefficient in WT). The transformation makes use of a normalized Gaussian as the window function (blue term). τ denotes the center of this Gaussian window function. The S-transform also uses a sinusoidal function (red term) as its kernel, which is similar to classical Fourier Transform. As in Fourier Transform, the S-transform gives the magnitude ($|S(\tau,f)|$) and the phase ($\arg(S)$) of a signal. The continuous function $x(t)$ can be recovered from the complex S coefficient, $S(\tau,f)$ (Stockwell et al., 1996).

Stockwell et al. (1996) suggested that the S-transform be computed in the frequency domain. Equation 2.4 shows that the S-transform operation can be conducted in the FT

of the $x(t)$ function, $X(f)$.

$$S(\tau, f) = \int_{-\infty}^{\infty} X(\alpha + f) \exp\left[-\frac{2\pi^2\alpha^2}{f^2}\right] \exp\left[i2\pi\alpha\tau\right] d\alpha \quad f \neq 0 \tag{2.4}$$

To numerically compute the S-transform, the continuous form of S-transform (Equation 2.3) must be converted to its discrete form. By letting $\alpha = \frac{m}{NT}$, $f = \frac{n}{NT}$ and $\tau = jT$, Equation 2.4 becomes:

$$S\left(jT, \frac{n}{NT}\right) = \sum_{m=0}^{N-1} X\left(\frac{m+n}{NT}\right) \exp\left[-\frac{2\pi^2 m^2}{n^2} + \frac{i2\pi mj}{N}\right] \quad n \neq 0 \tag{2.5}$$

with:

$$X\left(\frac{n}{NT}\right) = \frac{1}{N} \sum_{k=0}^{N-1} x(kT) \exp\left[-\frac{2\pi nk}{N}\right] \tag{2.6}$$

The summation form, as shown in Equation 2.5, allows one to compute the S-transform numerically. Firstly, the seismogram is transformed into its frequency domain $X(f)$ (Equation 2.6). This operation demands $Nlog(N)$ operation if FFT is used. Then the S-transform can be calculated using Equation 2.5. It can be roughly estimated that using this equation to calculate the S-transform requires N^3 operation, which is computationally demanding.

Brown et al. (2010) proposed an alternative strategy for computing the S-transform by introducing the so-called α domain. The α domain is obtained by applying the Fourier Transform to the S-transform equation (along the τ-axis). Then, the α domain is defined as follows:

$$\alpha(f', f) = \int_{-\infty}^{\infty} S(\tau, f) \exp\left[-i2\pi f'\tau\right] d\tau \tag{2.7}$$

By recalling Equation 2.3, Equation 2.7 can then be written as follows (more detailed steps deriving Equation 2.8 from 2.7 are included in the Appendix):

$$\alpha(f', f) = X(f' + f)W(f', f) \tag{2.8}$$

$X(f)$ is the Fourier Transform of a seismogram, $x(t)$. $X(f' + f)$ represents the shifted $X(f)$ by f' unit. Hence, the elements of each row of the matrix $X(f' + f)$ are the FT of the $x(t)$ function with certain shifting depending on its row number. $W(f)$ is the Fourier Transform of the Gaussian window function whose elements are composed of the row of matrix $W(f', f)$. $W(f', f)$ can be expressed as:

$$W(f', f) = \int_{-\infty}^{\infty} \frac{|f|}{\sqrt{2\pi}} \exp\left[\frac{-f^2\gamma^2}{2}\right] \exp\left[-i2\pi\gamma f'\right] d\gamma \quad \gamma = \tau - t \tag{2.9}$$

Once the α-domain has been successfully computed, the S-transform coefficient can be estimated by applying an inverse Fourier Transform to the α domain:

$$S(\tau, f) = \int_{-\infty}^{\infty} \alpha(f', f) \exp\left[i2\pi f'\tau\right] df' \tag{2.10}$$

Therefore, performing the S-transform in the frequency domain requires two steps: building the matrix α (Equation 2.8), and then applying an inverse Fourier Transform to that matrix in order to obtain the S-transform component (Equation 2.10).

The S-transform operation is graphically depicted in a more detailed workflow in Figure 2.1. This transformation is also called a discrete S-transform (DST). DST is commonly conducted in the frequency domain, using the following steps:

1. Calculate the Fourier Transform of the seismogram, $X(f) = \mathcal{F}\{x(t)\}$. The boxcar function has been chosen as an example of an input (real) signal.

2. Build the matrix $X(f' + f)$ where each row i is occupied by the shifted $X(f)$ by one sample relative to row $i \pm 1$ (i being the one row).

3. Compute the Gaussian weighting function with different frequencies and apply Fourier Transform to each function to compose the $W(f', f)$ matrix.

4. Construct matrix α-domain by employing point-to-point multiplication according to Equation 2.8.

5. Apply the inverse Fourier Transform to each row in α-domain (Equation 2.10). The resulting matrix is the S-transform coefficient, $S(\tau, f)$.

Figure 2.2 shows one example of the vertical component of the seismogram recorded during the passive seismic experiment at Tarutung, Sumatra Island, Indonesia. The event is associated with tectonic activities of the Sumatran Fault (Muksin et al., 2013). At least three seismic events can be seen in this figure. This figure also shows the time-frequency of the seismogram computed using the DST method previously described. The frequency spectrum of the seismogram is also shown for comparison. As can be seen from the figure, only low level ambient noises contaminate the seismogram since the signal of wave arrivals can still be identified. The frequency spectra of the seismogram reveals two peak frequencies: at around 20 Hz and lower than 10 Hz. The frequency spectra as resulted from the Fourier Transform cannot explain the origin of the two peaks. However, after

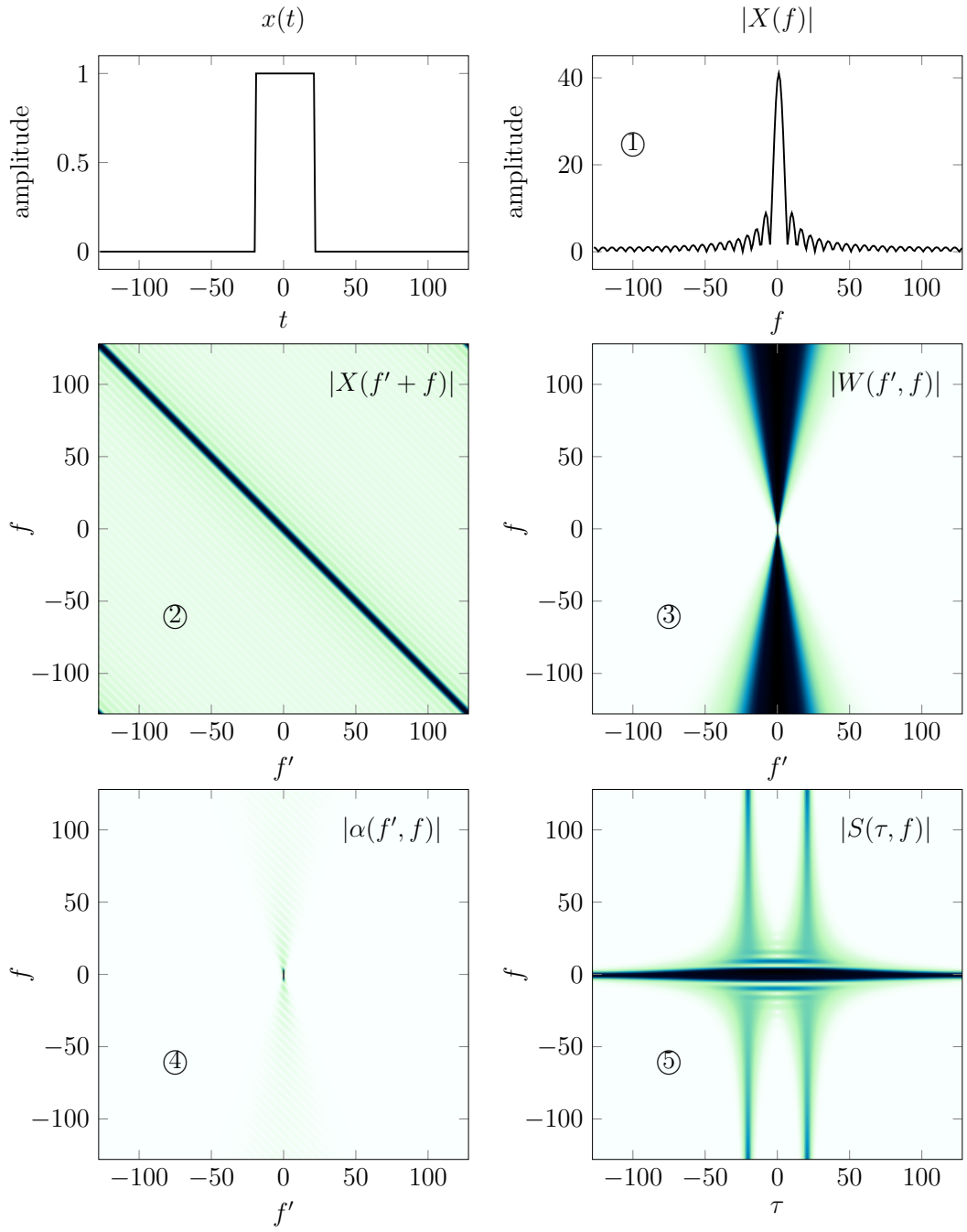

Figure 2.1: Workflow of discrete S-transform: (1) Apply the Fourier Transform of the input signal, $x(t)$, (2) compose the $X(f'+f)$ matrix by shifting the $X(f)$, (3) take the Fourier Transform of the Gaussian window function and compose the $W(f',f)$ matrix, (4) multiply the $X(f'+f)$ with $W(f',f)$ to compute α matrix and (5) apply the inverse Fourier Transform of α matrix to estimate S-coefficients, $S(\tau,f)$. Please note that all the complex functions are represented in magnitude for simpler description. A dark color represents a high value.

applying localized frequency analysis, one can easily recognize that these two peaks are associated with P- and S- waves since the P and S waves arrive at different times. This is the motivation for using filtering in the time-frequency domain. Although signals and noises overlap in their frequency range, the separation of signal and noise can still be performed in the frequency domain while preserving the original features of the signals.

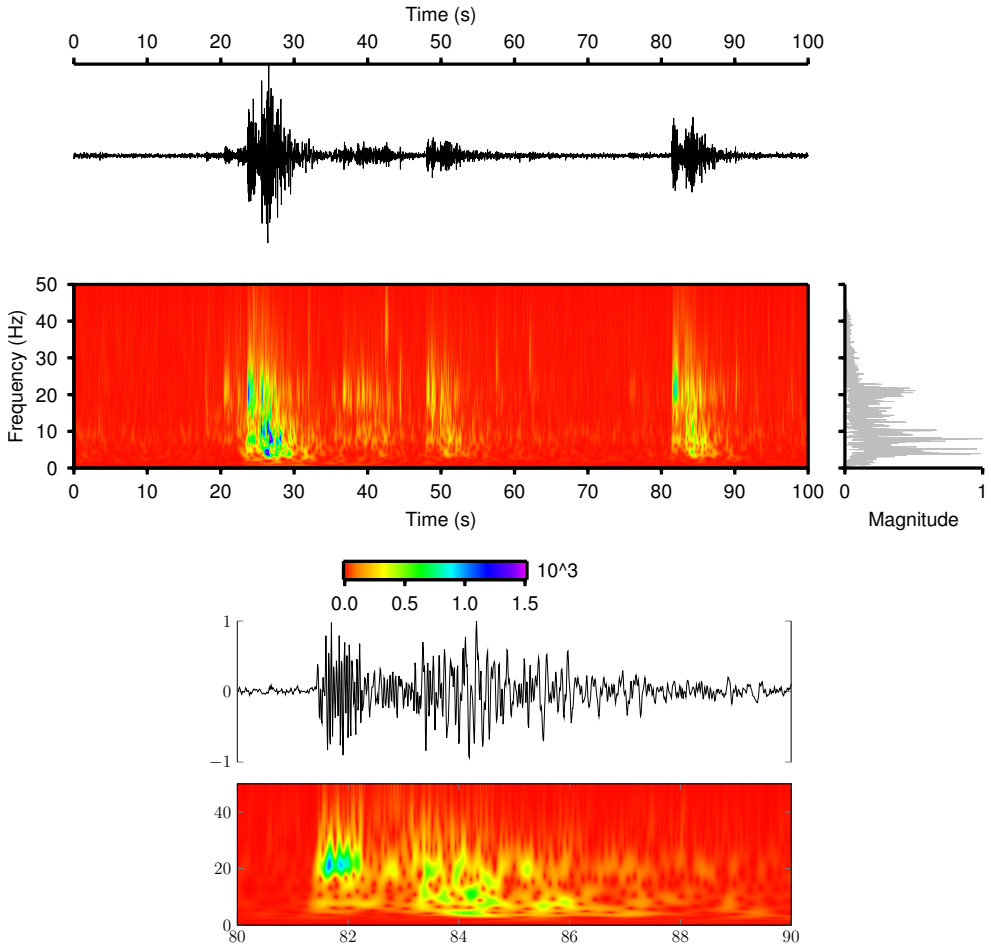

Figure 2.2: (Upper) A passive seismic seismogram (raw data) showing at least three seismic events. (Middle) The time-frequency and frequency spectrum of the seismogram computed using DST and traditional FT. (Lower) Seismogram shown between 80-90s and its corresponding time frequency.

2.1.2 Time-frequency denoising

The process of recovering signals from noisy data sets (or filtering), with the objective of increasing the signal-to-noise ratio, is often operated in the frequency domain. It is

easier to separate signals and noises in the frequency domain since, in general, signals and noises have different frequency spectra. Band-pass filtering, the most common filtering method used, is conducted by first transforming the seismogram to its frequency spectrum using Fourier Transform, and applying band-pass filtering to that spectrum. Finally, the filtered frequency spectrum is transformed back to the time domain to estimate the noise-less seismogram. However as previously mentioned, most seismic recordings are non-stationary, so it is better to conduct frequency filtering by considering the local time-frequency content. In this study, a filtering technique in the time-frequency domain was developed.

Signals and noise was separated in the magnitude of the S spectra (time-frequency domain). To separate signals and noise, a threshold needs to be defined. An optimal threshold should be selected, which will lead to successful filtering. The commonly used approach to determine the threshold value is the universal threshold, $\lambda = \sigma^{noise}\sqrt{2\log(N)}$ (Donoho & Johnstone, 1994). This requires the estimation of noise variance, σ^{noise}. Another frequently used thresholding is the Otsu threshold (Otsu, 1979). In this study, the Otsu thresholding will be used as it does not require a priori information such as noise variance. Even though noisy parts of a seismogram can be easily found, such as before the onset of a P wave arrival, it is still ambiguous since one needs to determine the number of samples considered as noise. Choosing a too large N might excessively smooth the seismogram (Chang et al., 2000).

Otsu thresholding

Tselentis et al. (2012) made use of the Otsu thresholding method to separate signal and noise clusters in the time-frequency domain. Since the value of S-spectra is complex, Tselentis et al. (2012) proposed the application of Otsu thresholding independently to each real and imaginary component of the S-spectra. In this study, I proposed another alternative approach by employing thresholding on the magnitude of the S-spectra, $\sqrt{Re(S)^2 + Im(S)^2}$. The main purpose of this strategy is to preserve the phase of the S-spectra. By independently applying thresholding to each real and imaginary component of the S-spectra, the phases might be changed, since the real and imaginary threshold values are most likely different. The phase changes might result in changing the wave onset and will affect the arrival time information.

Denoising a seismogram by using a thresholding method can be simply conducted by following these two consecutive steps:

1. Determining the threshold value based on the Otsu method (Otsu, 1979).

2. Applying S-spectra filtering by imposing the hard thresholding rule (i.e., Donoho & Johnstone, 1994; Aghayan et al., 2016).

Determining the threshold

I adopted the Otsu thresholding technique (Otsu, 1979), which was used to separate background noise from an image (signal). In the end, the method produces an optimal threshold value, t^*. In this study, this threshold t^* was used to classify the magnitude of S-spectra into two classes: one class associated with the background noise, C_0 and the other corresponding to the signal C_1. This classification can be expressed as follows:

$$\begin{aligned} C_0(t^*) &= \{|S| \leq t^*\} \\ C_1(t^*) &= \{|S| > t^*\} \end{aligned} \tag{2.11}$$

$|S|$ is the S-spectra of a seismogram. The study uses an assumption that C_0 is noise while C_1 is the signal. This assumption will be valid for cases where the seismograms have a signal-to-noise ratio higher than 1 (SNR > 1). To determine the Otsu threshold, firstly the $N = N_f \times N_t$ (number of frequency and time samples, respectively) samples of S-spectra are transformed into a histogram with L bins or levels $[1, 2, \ldots, L]$. Hence, the range of $|S|$ values of each level is:

$$\Delta = \frac{|S|_{max} - |S|_{min}}{L} \tag{2.12}$$

Figure 2.3 illustrates the hypothetical histogram of an S-spectra. If the magnitude of the S-spectra at each level is n_i, then the S-spectra histogram is defined by:

$$h_i = \frac{n_i}{N} \quad \text{with} \quad h_i \geq 0 \quad \text{and} \quad \sum_{i=1}^{L} h_i = 1 \tag{2.13}$$

h_i can also be regarded as the probability density function or probability of occurrence. Any threshold t divides the S-spectra histogram into two classes; for each class, the statistical measures such as probability of occurrence (ω), and mean (μ), respectively, can

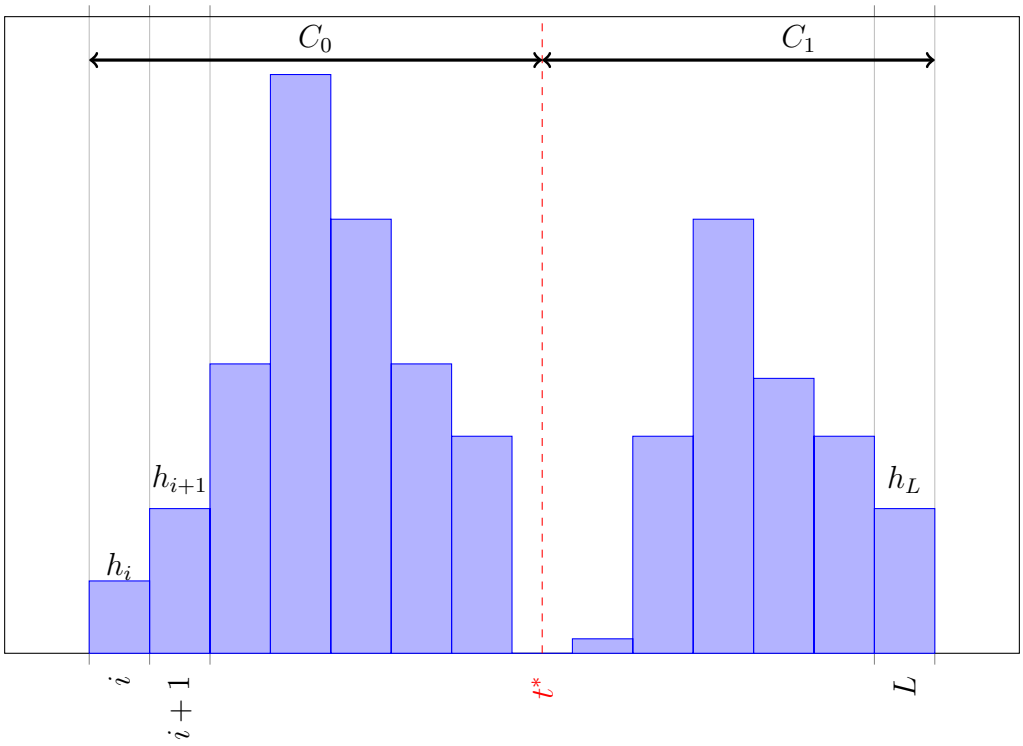

Figure 2.3: An illustration of the use of Otsu thresholding. The histogram of the magnitude of S-spectra is first computed; then the histogram is used to produce two classes of histogram: C_0 and C_1

be defined as follows:

$$\begin{aligned} \omega_0 &= \omega(t) = \sum_{i=1}^{t} h_i \\ \omega_1 &= \sum_{i=t+1}^{L} h_i = 1 - \omega_0 = 1 - \omega(t) \end{aligned} \tag{2.14}$$

and

$$\begin{aligned} \mu_0 &= \mu(t) = \sum_{i=1}^{t} \frac{ih_i}{\omega_0} \\ \mu_1 &= \sum_{i=t+1}^{L} \frac{ih_i}{\omega_1} \end{aligned} \tag{2.15}$$

Total mean μ_T can be easily defined by:

$$\mu_T = \sum_{i=1}^{L} \frac{ih_i}{\omega_0 + \omega_1} = ih_i \tag{2.16}$$

By considering Equation 2.15, it can be proven that the total mean can be expressed by:

$$\mu_T = \omega_0\mu_0 + \omega_1\mu_1 \tag{2.17}$$

Variance, another statistical measure, can also be defined for each class C_0 and C_1 respectively, as follows:

$$\begin{aligned}\sigma_0^2 &= \sum_{i=1}^{t} \frac{(i-\mu_0)^2 h_i}{\omega_0} \\ \sigma_1^2 &= \sum_{i=t+1}^{L} \frac{(i-\mu_1)^2 h_i}{\omega_1}\end{aligned} \tag{2.18}$$

In accordance with the thresholding goal of separating the histogram into two distinct classes, the evaluation of the optimal threshold is conducted by maximizing one of the following objective functions (Otsu, 1979):

$$\begin{aligned}\lambda &= \frac{\sigma_B^2}{\sigma_W^2} \\ \kappa &= \frac{\sigma_T^2}{\sigma_W^2} \\ \eta &= \frac{\sigma_B^2}{\sigma_T^2}\end{aligned} \tag{2.19}$$

where

$$\sigma_W^2 = \omega_0 \sigma_0^2 + \omega_1 \sigma_1^2 \tag{2.20}$$

$$\sigma_B^2 = \omega_0 \omega_1 \left(\mu_1 - \mu_0\right)^2 \tag{2.21}$$

$$\sigma_T^2 = \sum_{i=1}^{L} \left(i - \mu_T\right)^2 p_i = \sigma_W^2 + \sigma_B^2 \tag{2.22}$$

σ_W^2, σ_B^2 and σ_T^2 are within class variance, between class variance and the total variance, respectively. η provides an efficient way to determine an optimal threshold comparing to λ and κ since σ_B^2 involves only the first-order statistics (only required to compute mean required, rather than variance for each class) and σ_T^2 has a fixed value for any threshold t. The objective function now becomes much simpler: to only maximize σ_B^2. The optimal threshold t^* can be formulated as:

$$\sigma_B^2(t^*) = \max_{1 \le t < L} \sigma_B^2(t) \tag{2.23}$$

The optimal threshold can be found by using a grid search. Each bin is regarded as a potential threshold, and $\sigma_B^2(t)$ is calculated for each bin. The largest $\sigma_B^2(t)$ is searched for, since it corresponds to the optimal threshold, t^*.

Thresholding Rule

Once the optimal threshold has been obtained, the segregation of the S-spectra into signal and noise components can be carried out based on a Thresholding Rule. Two well-known Thresholding Rules, hard and soft thresholding (Donoho & Johnstone, 1994), are considered in this discussion. In hard thresholding, the values of S-spectra lower than the optimal threshold is reduced to zero, while preserving the rest of the S-spectra (values higher than the threshold). Then, the denoised S-spectrum S^{den} resulting from hard thresholding can be expressed by the following equation:

$$S^{\text{den}}(\tau, f) = \begin{cases} S(\tau, f) & \text{if } |S| \geq |S|^* \\ 0 & \text{if } |S| < |S|^* \end{cases} \tag{2.24}$$

where,

$$|S|^* = |S|_{min} + t^* \cdot \Delta \tag{2.25}$$

Δ is the bin interval of S-spectra value for each level (Equation 2.12). The other well-known thresholding is soft-thresholding, which is defined as follows:

$$S^{\text{den}}(\tau, f) = \begin{cases} S(\tau, f) - |S|^* & \text{if } |S| \geq |S|^* \\ 0 & \text{if } |S| < |S|^* \end{cases} \tag{2.26}$$

The relation between raw and denoised S-spectra (only for positive values and values higher than threshold value) in both hard and soft thresholding is graphically depicted in Figure 2.4. From Figure 2.4, it can easily be seen that the soft thresholding rule lowers

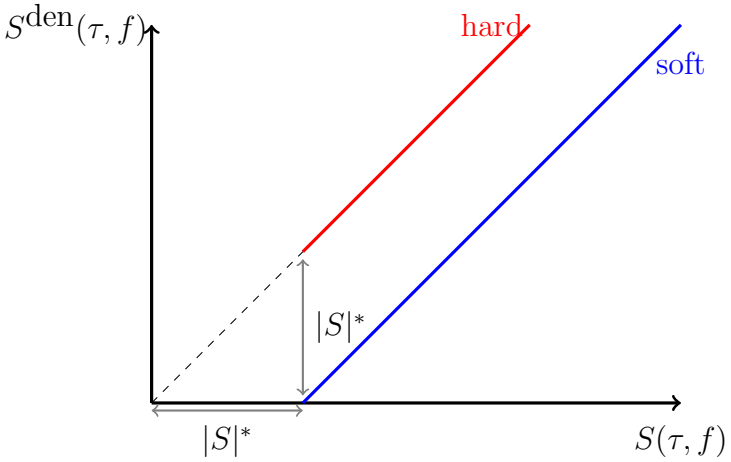

Figure 2.4: Graphic illustration of hard (red) and soft (blue) thresholding.

the S-spectra that have a value larger than the threshold. Lowering this class of S-spectra

might imply lessening the amplitude of the important signal. On the other hand, hard thresholding also has shortcomings as the method introduces some artifacts in the denoised results (Chang et al., 2000). To avoid shrinkage of the signal due to soft-thresholding and at the same time reduce the artefact that might result from hard-thresholding; in this study, I propose to use a smoothed version of hard-thresholded S-spectra. The triangle filtering (Claerbout & Fomel, 2014) has been chosen as a smoothing method. Hence, the thresholding rule used in this study is:

$$S^{\text{den}*}(\tau, f) = TF\left\{S^{\text{den}}(\tau, f)\right\} \tag{2.27}$$

TF is the triangle filtering for smoothing the filtered S-spectra.

The proposed filtering technique was tested on a seismogram taken from the field (Figure 2.5, A) in order to evaluate its performance. Figure 2.5 (A) shows raw data, in which some noise exists and obscure the time of the P wave onset. The raw data was then transformed to its S-spectrum (Figure 2.5, B) using the Discrete S-transform method, resulting in an estimation of the time-frequency map of the seismogram. The time frequency shows complicated or heterogeneous S-spectra. Varying frequencies are observed in the S-spectra, which indicates a non-stationary behavior of the signal. This non-stationary feature might make traditional band-pass filtering (using only Fourier Transform) ineffective in removing undesired signals. Therefore, Otsu thresholding was applied to the S-spectrum. The range of magnitudes of the S-spectrum is $9.2 \times 10^{-2} - 3.3 \times 10^{3}$. The number of bins used to represent the S-spectrum in histogram form is 1024 (See Figure 2.6). Using the code I developed (Attached in the Appendix), the Otsu threshold was approximated to be 604.

As mentioned before, the thresholding was applied to the S-spectra; thus, the S-spectra values lower than 604 were reduced to zero and the remaining values were kept (hard-thresholding). To avoid artifacts caused by the abrupt change near the threshold value, triangle smoothing is applied to create a smooth transition between the zero value (denoised region) and its surroundings (higher than zero). The final result of the denoised S-spectrum is shown in Figure 2.5(C). The denoising removes the low intensity S-spectrum which is assumed to be background noise (in the case of SNR higher than 1). Finally, a new seismogram which was obtained by transforming the filtered S spectra back to its corresponding time-domain is depicted in Figure 2.5(D). The back transformation uses the original phase information since the thresholding was not applied to the phase

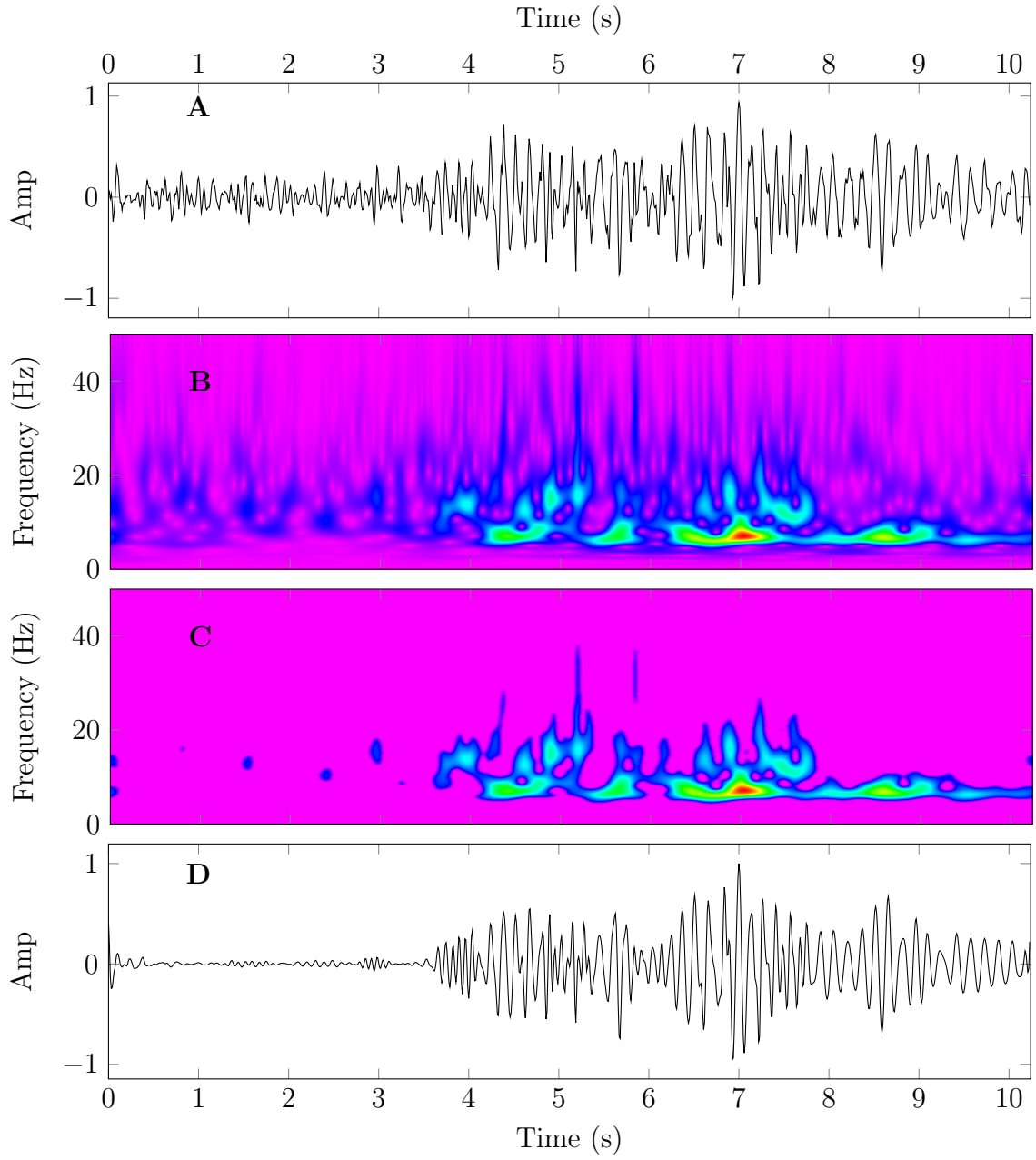

Figure 2.5: Otsu thresholding workflow. The original seismogram (A) was transformed to its S-spectrum (B). The Otsu thresholding was applied to this S spectrum; then the resultant spectrum (C) was transformed back to the time domain to estimate the filtered seismogram (D).

part. In the reconstructed seismogram, most of the noise seen in the original seismogram (Figure 2.5[A]) disappear. This eventually leads to a seismogram with higher SNR. Then, the P-wave onset can finally be clearly observed.

The relationship between raw and denoised S-spectrum after applying triangle filtering can be empirically obtained by plotting both S-spectrum. Figure 2.7 shows the crossplot

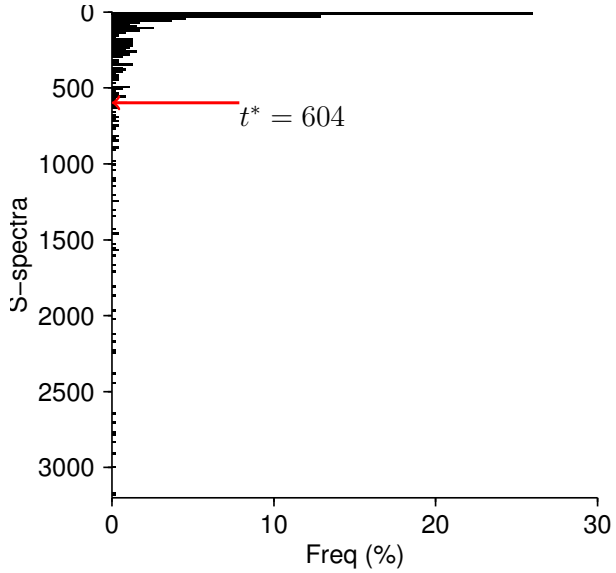

Figure 2.6: Histogram of the magnitude of S-spectra shown in Figure 2.5(B). After applying the Otsu thresholding by using the number of bins at 1024, the optimal threshold obtained was 604.

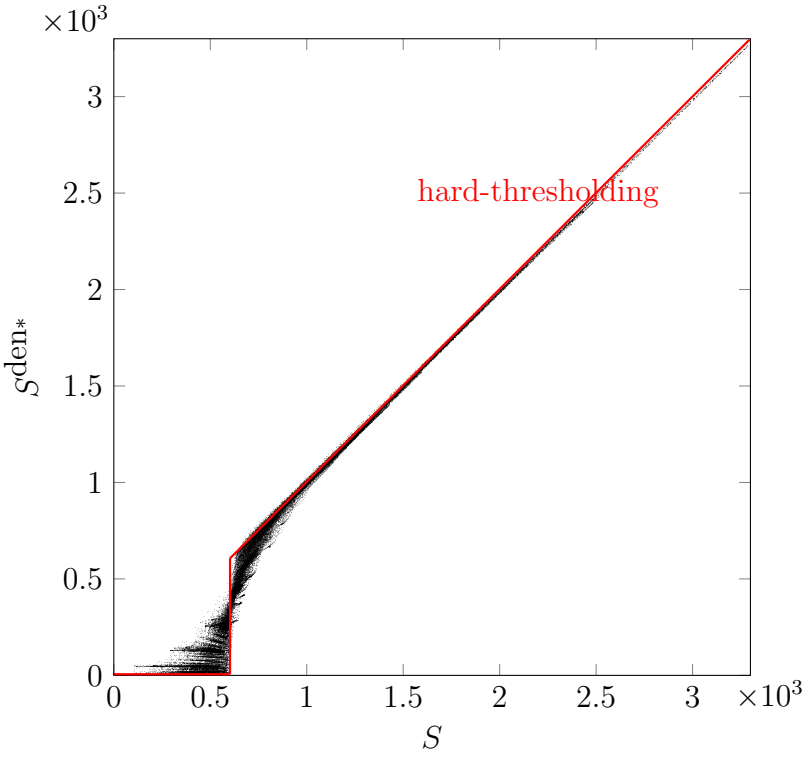

Figure 2.7: Crossplot between raw (S) and denoised S-spectra (S^{den*}). For comparison, the hard-threshold operator is also shown in red.

of S-spectra between the raw and denoised samples. The effect of smoothing can be seen in the surrounding area of the Otsu threshold (604), while S-spectrum far from this

threshold value is unaffected. However, some values below the Otsu threshold increased to a value greater than 0 rather than remaining at zero. By combining hard thresholding and triangle smoothing, one can avoid the downside of applying soft thresholding and hard thresholding simultaneously.

Figure 2.8 compares the raw and filtered seismograms. The waveform similarity is very high after time 4s (around the onset of the P wave). The denoising method only subtracts the amplitudes from the seismogram before 4s. A very high amplitude similarity between raw and denoised seismograms indicates that the level of noise at this range is very low. This amplitude similarity can be achieved since the phase of the seismogram is constant before and after the denoising.

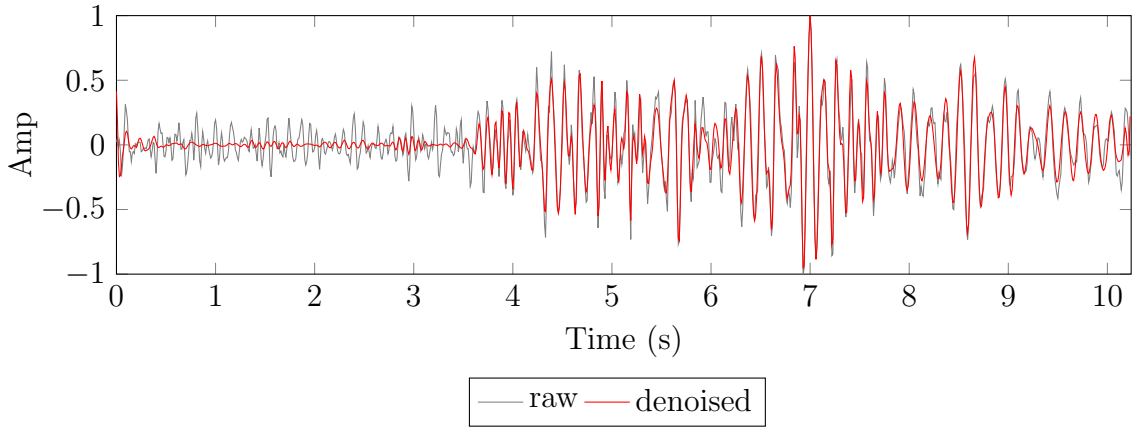

Figure 2.8: Examples of recorded seismograms before (gray) and after applying denoising (red). The figures are similar to 2.5 (A) and (D). The amplitudes are normalized to their maximum rate.

Figure 2.9 shows the amplitude differences between raw and denoised seismograms. The figure indicates that the removed part of the waveforms from the raw seismogram is almost Gaussian (random) with similar maximum amplitude over time.

To examine the effect of Otsu thresholding on the bandwidth of the seismogram, a comparison between the frequency spectra of the raw and denoised seismograms is depicted in Figure 2.10. The thresholding significantly reduces frequencies below 5 Hz and those greater than 35 Hz. However, the frequencies between 5-20 Hz were preserved as those frequencies are associated with important features of the seismogram, particularly the onset of P waves (at around 15 Hz).

The above denoising algorithm was also tested to automatically denoise the raw seis-

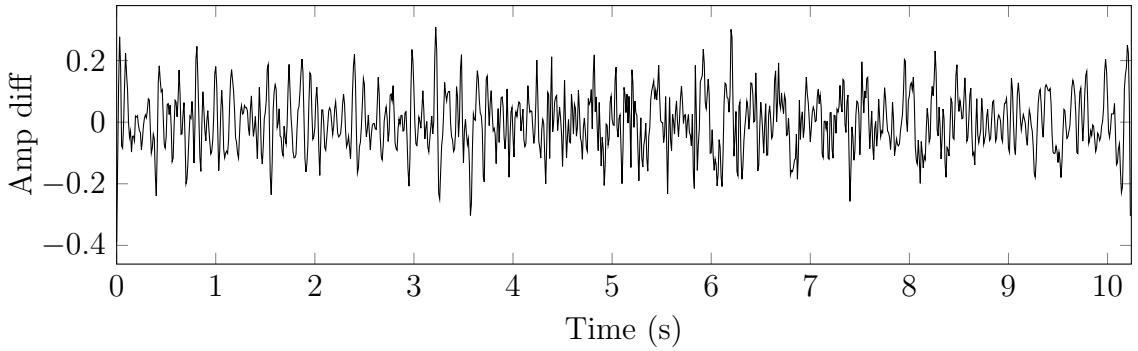

Figure 2.9: Amplitude differences between the original and denoised seismograms.

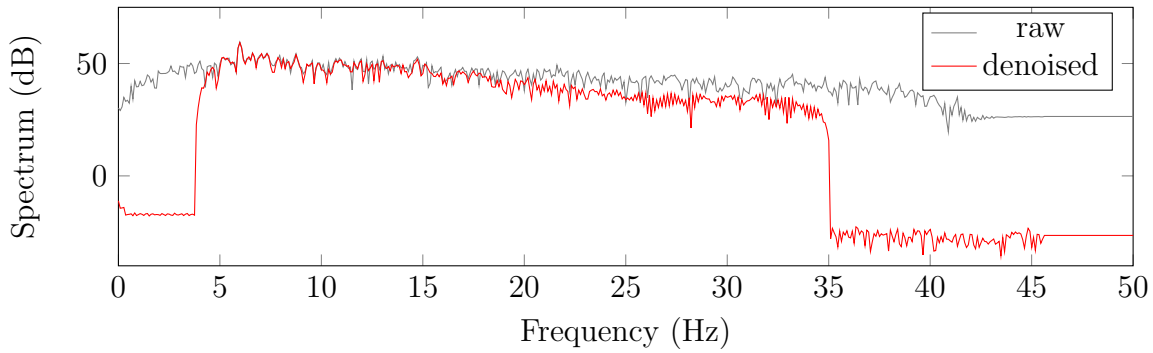

Figure 2.10: A comparison of the spectra of the raw (gray) and denoised (red) seismogram.

mograms recorded by 41 seismometers. The primary goal of applying the denoising is to improve the SNR of the seismogram so that the onset of P and S waves can be more easily recognized. As can be seen from Figure 2.11 (a), the SNRs of the seismograms significantly vary qualitatively between traces. A robust and adaptive thresholding is required to handle these seismograms since each seismogram requires a different denoise parameter (e.g., threshold level). Firstly, the raw seismograms were transformed into time-frequency. Then, the Otsu thresholds were estimated for each time-frequency. After zeroing the S-spectra below the threshold, triangle smoothing was applied. The results are shown in Figure 2.11 (b). In general, it can be seen that the Otsu denoising successfully improved the SNR of most seismograms and the onset of P waves became much easier to identify.

Figure 2.12 presents the Otsu threshold values computed from the raw seismograms (Figure 2.11 [a]) in two different time windows, 20-30s and 0-100s. For most of the traces, the resulting Otsu thresholds for both time windows are different (for example, at traces 2,3,4,6, etc.). These occur since more than one seismic event exists in the broader time window. By using a broader time window, other events are included which then change the threshold value. At each implementation, then, it is critical to choose a proper time

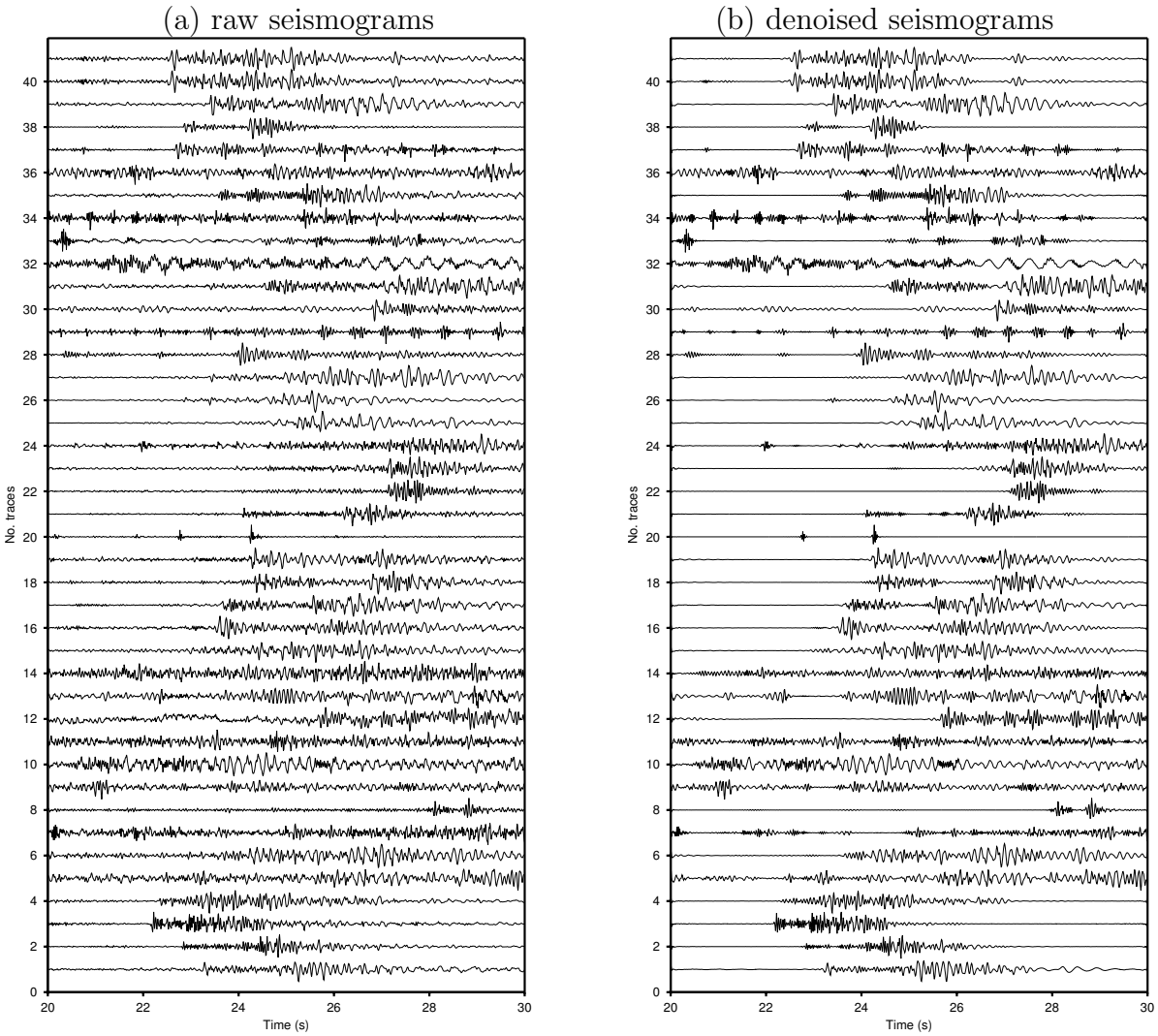

Figure 2.11: Comparison of the original waveform and its filtered results using Otsu thresholding. Amplitudes of each trace are normalized to their maximum value. The trace number 6 is similar to those shown in Figure 2.5.

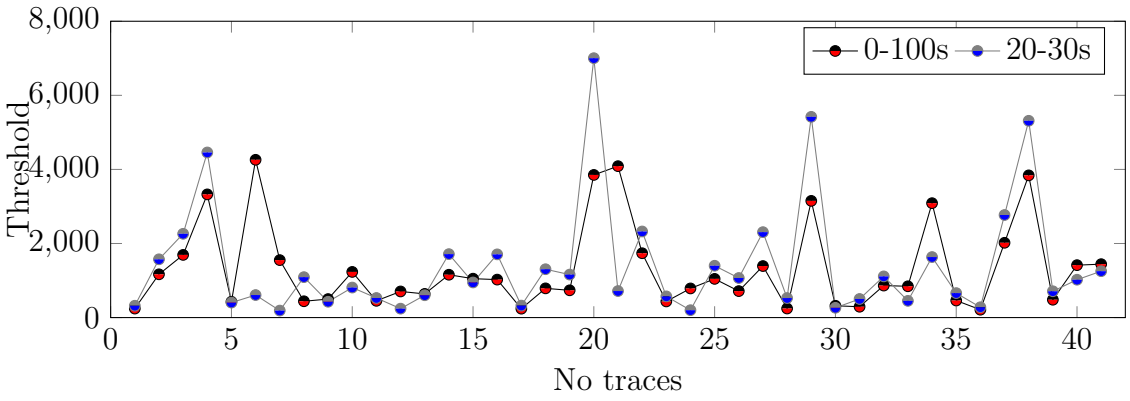

Figure 2.12: Otsu threshold computed from seismograms as shown in Figure 2.11(left).

interval in order to maximize the effectiveness of Otsu thresholding. A priori information regarding the P-wave onset could be beneficial to achieve optimal denoised results. The P-wave onset information could be provided by STA/LTA or AIC.

2.2 Characteristic function

Signals embedded in seismograms can be distinguished from their surrounding background noises by extracting the frequency content, polarization attributes, as well as other attributes from the original time-domain waveform amplitudes (Lomax et al., 2012). These attributes, or characteristic functions (CF), highlight the P and S wave signals and reduce the trailing waves. Hence, the main goal of transforming time-domain seismograms into other CFs is to emphasize the onset of P and S waves. The CF is used as input for a waveform-based localization method instead of the time-domain seismogram. Various CFs have been proposed in waveform-based seismic event localization, such as:

1. Absolute value of seismogram (Kao & Shan, 2004),
2. Envelope of seismogram (Baker et al., 2005; Gharti et al., 2010),
3. Ratio of short-term average and long-term average (STA/LTA) (Drew et al., 2013; Grigoli et al., 2014),
4. Kurtosis derivative (Langet et al., 2014), and
5. Power spectral density (Vaezi & der Baan, 2015).

The Akaike Information Criterion (AIC) function (Akaike, 1973) is considered as a tool to assist the detection of the onset of first arrivals (i.e., Jousset et al., 2011). For a discrete seismogram $w = \{w_1, w_2, ..., w_N\}$ with N samples, the AIC of the seismogram is defined as (Maeda, 1985),

$$\mathrm{AIC}(i)_{1,N} = i \log\left[var(w[1,i])\right] + (N-i-1)\log\left[var(w[i+1,N])\right] \tag{2.28}$$

The subscript in $\mathrm{AIC}(i)_{1,N}$ means that the AIC function is computed from the 1^{st} sample until the N^{th} sample of a seismogram. i runs through the all of the samples of a seismogram. log is a natural logarithm and var is the variance of the seismogram amplitudes.

The onset of first arrivals is indicated by the global minimum of the AIC curve. Figure 2.13 shows an example of the AIC function of a vertical component of a seismogram, which clearly exhibits the onset of P and S seismic waves.

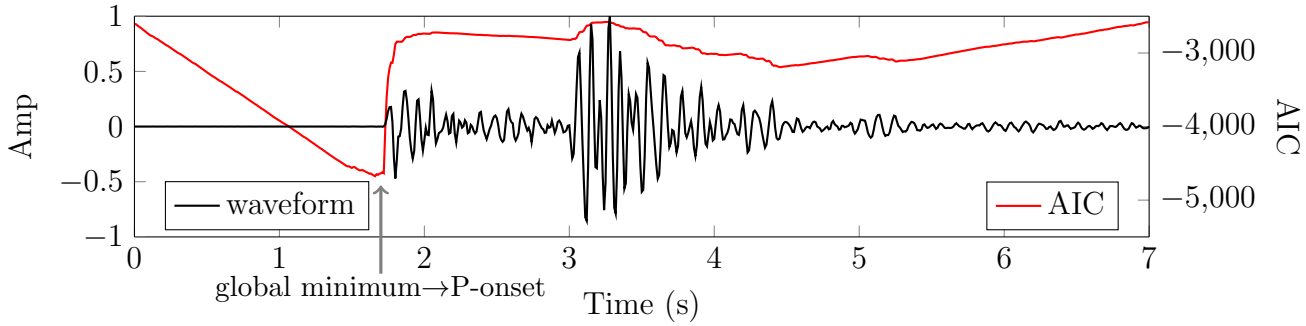

Figure 2.13: Representation of the amplitudes, and the AIC curve of a vertical component of a seismogram. Note that the minimum value of AIC curve corresponds to the P wave onset.

The onset of a P wave coincides with the global minimum of the AIC curve; whereas, the S wave corresponds with the local minimum. However in this example, the AIC curve is only beneficial for highlighting the P-wave onset. The indication of an S wave can be achieved by considering the horizontal component of a seismogram.

Figure 2.14 shows the comparison of the AIC function and STA/LTA of a seismogram. It is obvious that STA/LTA has a higher time resolution compared to an AIC function. If both of these CFs are considered as input for localization, the STA/LTA will produce event locations with better resolution (spatial and temporal). A strategy to increase the time ressolution of an AIC function is proposed in the next section.

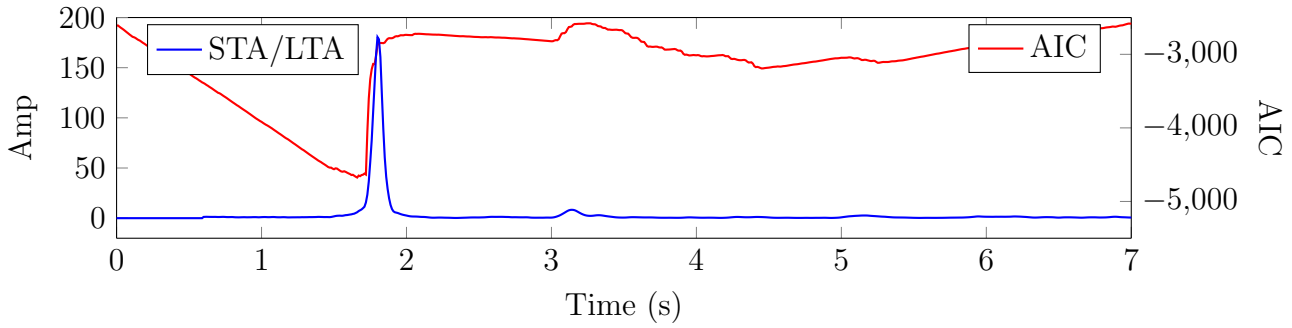

Figure 2.14: Comparison of STA/LTA and AIC function. The short and long window size used to compute STA/LTA are 0.1 and 0.5s respectively.

Another aspect that has to be carefully considered is window size. If the window

size is too large, the onset of the first arrival will not appear as the global maximum; as presented in Figure 2.15. The global minimum does not refer to P-and S-wave onset. In this case, AIC will fail to represent the wave onset.

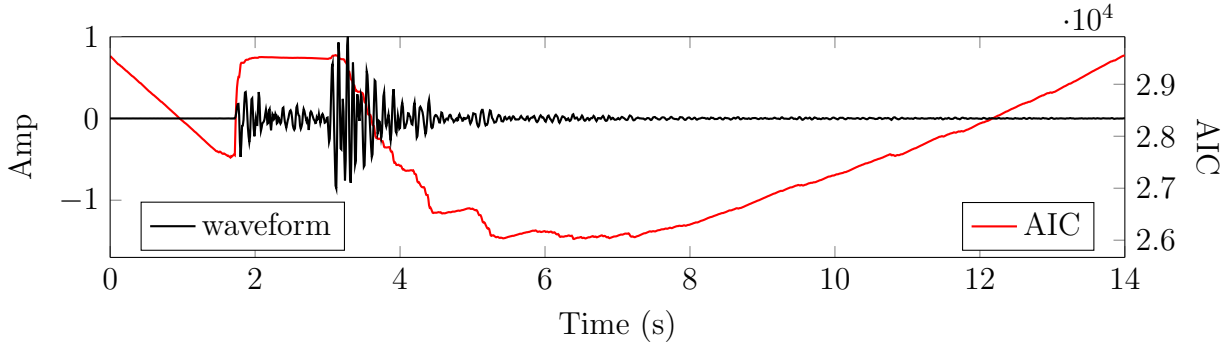

Figure 2.15: The AIC value computed with too large of a window size. The global maximum no longer reflects the onset of a first arrival.

The AIC computation was applied to the denoised seismogram discussed in Sec. 2.1.2 (Figure 2.5). The resulting AIC curve was then compared with that resulting from the raw seismogram. The comparison of the AIC curves is shown in Figure 2.16. Examining both AIC curves, the AIC curve resulting from the denoised seismogram shows better results. The AIC curve resulting from the raw seismogram (blue) shows up as somewhat flat at the wave onset. This might lead to a larger degree of uncertainty in determining the seismic event location using the diffraction stacking method. The AIC curve resulting from the denoised seismogram (black), however, shows a very large trough and makes the global minimum more distinct from its surroundings.

2.2.1 Proposed characteristic function

I propose to modify the classical AIC characteristic function, designated as modified AIC (mAIC), in order to resolve time resolution and to avoid mislocating the global minimum for a long seismogram. The mAIC function computes its value by using a sliding window with a fixed size. The computation of mAIC is schematically described in Figure 2.17. The mAIC value of a specified sample is calculated within the moving window. The window size is set much smaller than the length of the seismogram; i.e., 0.5s. The classical AIC computation (Equation 2.28) is used in each window, and the mAIC value is obtained by measuring the distance from the AIC value to its maximum value at a specified point.

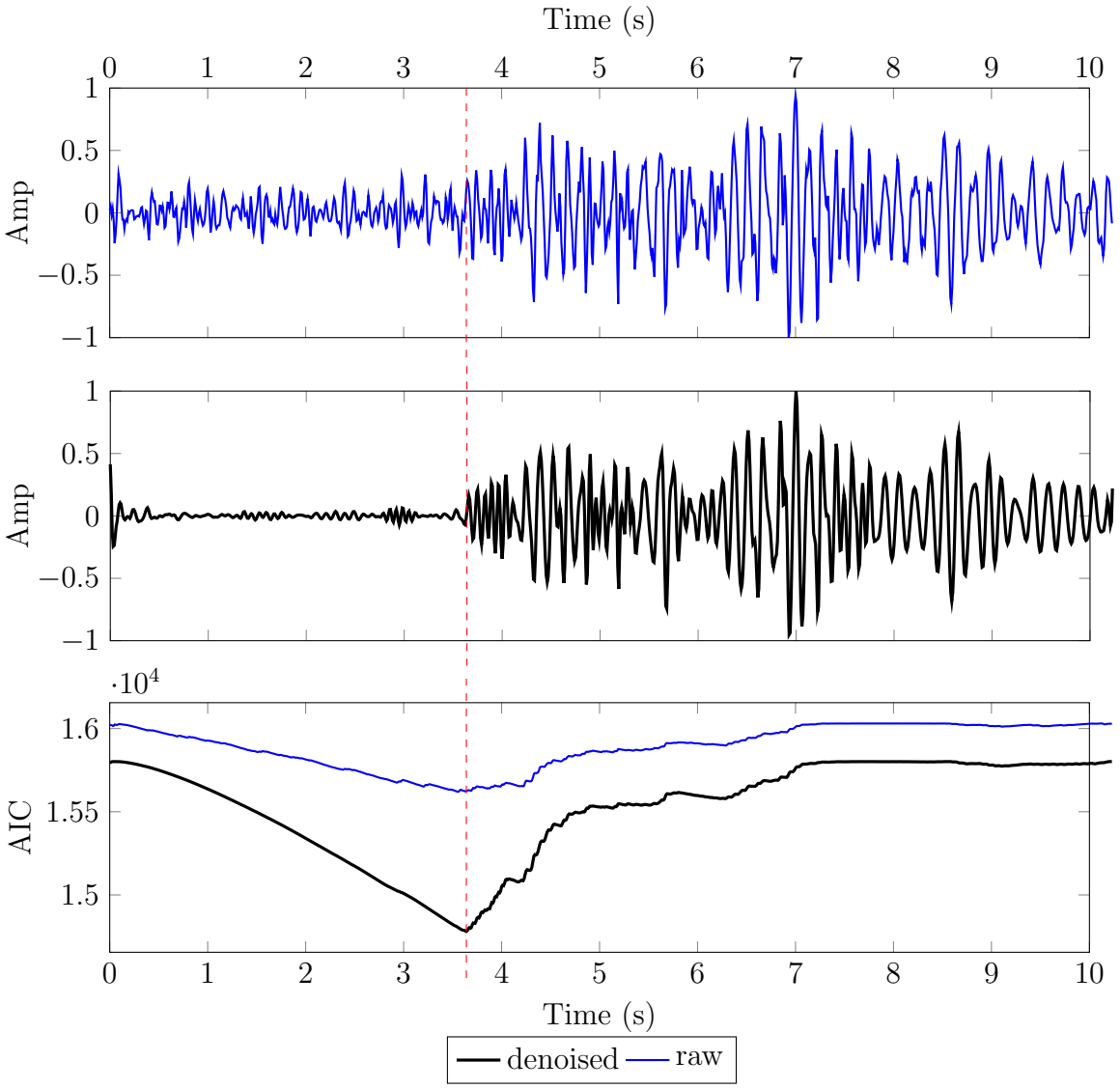

Figure 2.16: The AIC curve for raw (blue) and denoised (black) seismograms. Amplitude representatives of the corresponding seismogram are shown in the two top graphs.

The mAIC is expressed as:

$$mAIC(j) = \max\left\{AIC(i)_{j-T/2,j+T/2}\right\} - AIC(j)_{j-T/2,j+T/2} \tag{2.29}$$

Figure 2.17 illustrates the steps used in computing the characteristic functions using mAIC. The following is the explanation for this figure:

1. Define a window with a size of T samples. If the point being evaluated is at j^{th} index, then the window begins from sample $(j-T/2)^{\text{th}}$ until $(j+T/2)^{\text{th}}$. The AIC function $(AIC(i)_{j-T/2,j+T/2})$ will then be obtained. The AIC function is illustrated in the figure by the black curve.

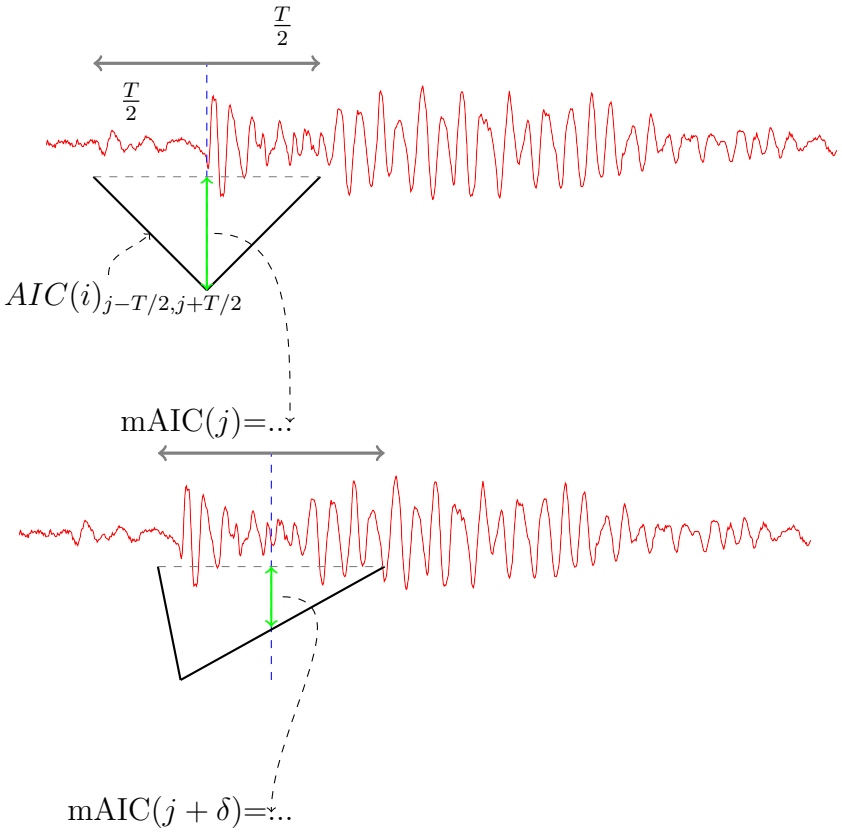

Figure 2.17: Schematic of mAIC function computation. The dashed gray line represents the maximum value of function $AIC(i)_{j-T/2,j+T/2}$.

2. Compute a distance between the value of windowed AIC at the point being evaluated j ,($AIC(j)_{j-T/2,j+T/2}$), and the maximum AIC value within the window (Equation 2.29). The distance is denoted by the green line.

3. Assign the distance (green line) to the mAIC(j).

4. Shift the window to compute the mAIC in the next sample $j+1$.

The proposed mAIC was computed using the previous example (Figure 2.15) using a window size of 1s (Figure 2.18). As can be seen from this figure, the traditional AIC function fails to indicate the onset of P and S waves since the length of the seismogram being evaluated is too long. There is no rule of thumb to determine the window size; however, it is better to not include the S-wave onset if one desires to estimate the P-wave onset. On the other hand, the mAIC function has successfully indicated the onset of P and S waves. Figure 2.18 clearly shows not only the P- but also the S-wave onset. Hence, the proposed mAIC characteristic function can be used to indicate the onset of P and S

waves, regardless of the length of the seismogram.

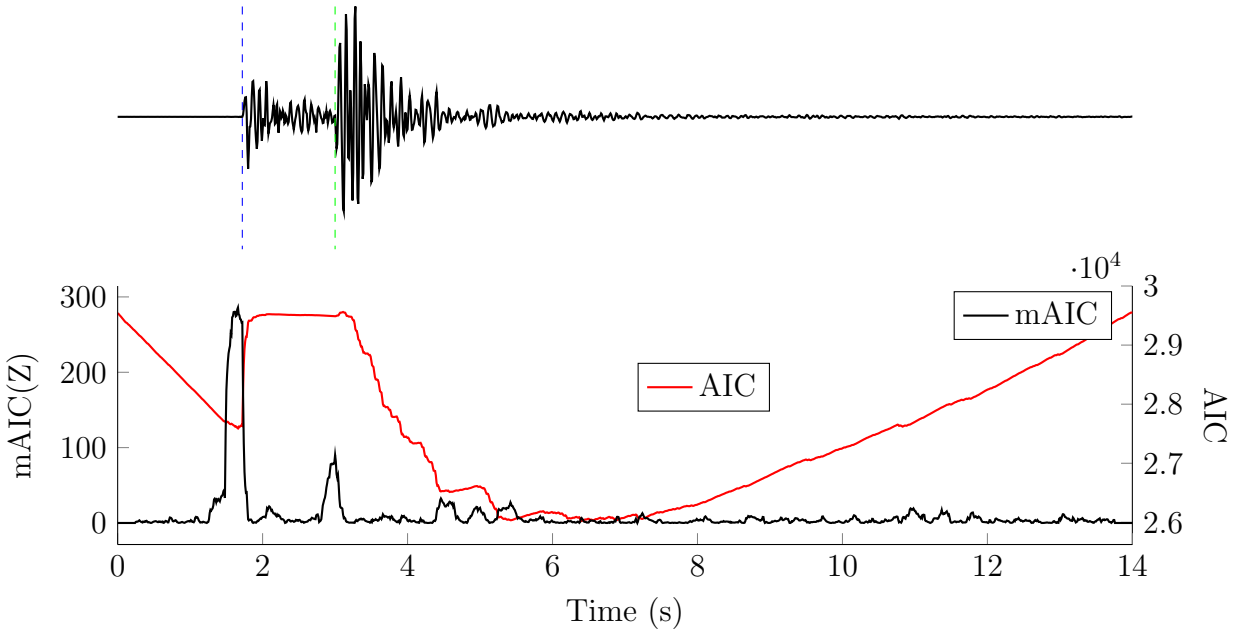

Figure 2.18: AIC and mAIC computed from the vertical component of a raw seismogram (counts) as shown in Figure 2.15. A window size of 0.5s has been used. The blue and green lines are the onset of P and S waves as estimated from the waveform using visual observation. mAIC (black line) indicates the onset of P and S waves by elevated values about time 1.5s (P-wave) and 3s (S-wave).

Various mAIC curves were also computed using different window sizes, T (Figure 2.19). Among the resulting mAIC functions, the mAIC curve computed using a window size of 0.25s showed the optimal result. Using this window size, the onset of P and S waves could easily be identified since the onsets are associated with the two peaks (indicated by blue and green vertical bars in the figure). With the window size of 2 and 3s, the mAIC curve around the P wave shows a broader peak, while the onset of the P wave coincides with the upper limit. These window sizes also cannot well indicate the S wave. This is due to the fact that the P and S wave delay time is less than 2s. It is known from time-frequency (not shown), that the frequency of a P wave is approximately 10 Hz. This value corresponds to a period of 0.1s. It would then be better to choose a window size more than twice that of the P-wave onset period.

A filtering technique which only bypasses either the P- wave or the S- wave from the seismogram needs to be developed. Then the localization of a seismic event could be done separately from the P- and S- waves. The final outcomes result from the image

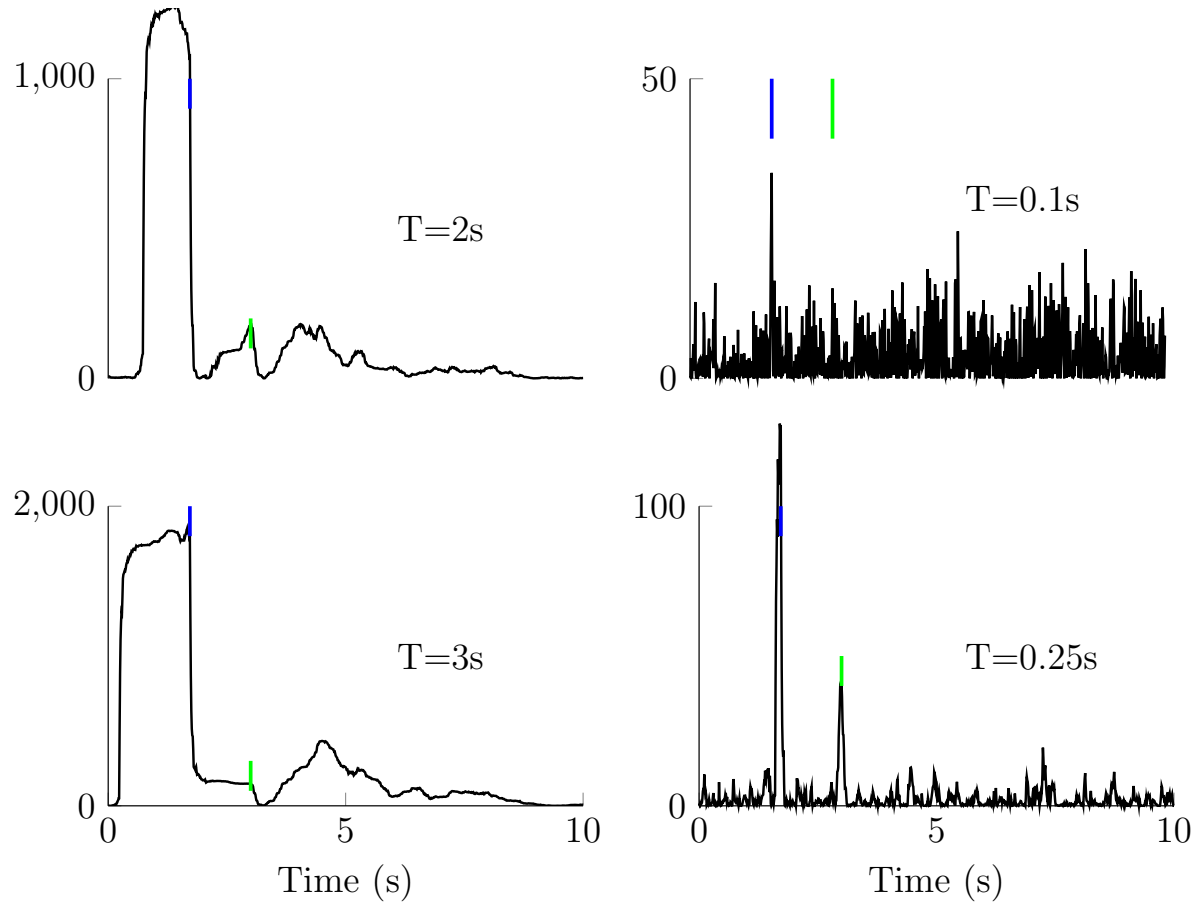

Figure 2.19: The mAIC function computed with various window sizes. The blue and green lines indicate the onset of P and S waves.

functions of the P- and S- waves. In this study, a strategy was developed to generate the characteristic functions of P- and S- waves. I propose to exploit the attribute of polarization as well as the characteristic function, mAIC. Consider one example of a three-component-recorded seismogram that is presented in particle velocity, as indicated by Figure 2.20. From this waveform, some polarization attributes can be derived such as rectilinearity and the vertical incident angle.

Attribute polarizations

The particle movements in 3D space are recorded using three orthogonal axes in the vertical (Z), north-south (N) and west-east (E) directions. The vector of particle propagation can be estimated from this three-component record by applying covariance analysis. The covariance computed between the components of the records composes the covariance

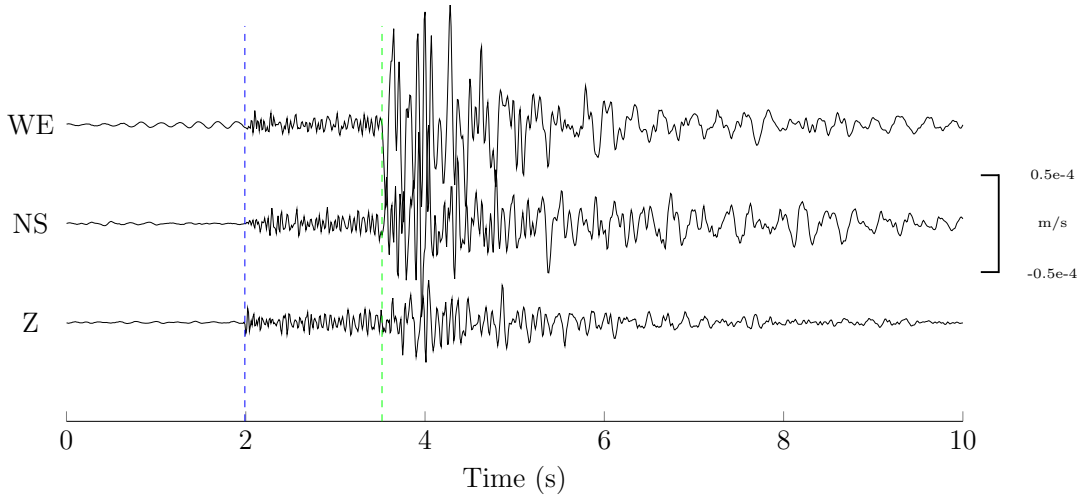

Figure 2.20: A three-component particle velocity record. The onset of P and S waves are indicated by blue and green lines, respectively.

matrix, $C(t)$.

$$\mathbf{C}(t_i) = \begin{bmatrix} var(Z) & cov(Z,N) & cov(Z,E) \\ cov(N,Z) & var(N) & cov(N,E) \\ cov(E,Z) & cov(E,N) & var(E) \end{bmatrix} \tag{2.30}$$

$Z(t)$, $N(t)$, and $E(t)$ denote the particle motion as functions of time. The covariance analysis is conducted in a time window with M samples, and the element of a covariance matrix can be expressed by:

$$cov(A_i, B_i) = \sum_{t=i-M/2}^{t=i+M/2} (A_t - \overline{A})(B_t - \overline{B}) \tag{2.31}$$

$\overline{A}$ and $\overline{B}$ are the mean of particle motions recorded at components A and B within a selected time window having M samples. Three eigenvalues ($\lambda_1 \geq \lambda_2 \geq \lambda_3$) are computed from the covariance matrix (Equation 2.30) using the following:

$$[\mathbf{C} - \lambda_i \mathbf{I}] \begin{Bmatrix} u_i \\ v_i \\ w_i \end{Bmatrix} = 0 \quad i = 1, 2, 3 \tag{2.32}$$

I represents the identity matrix. (u_1, v_1, w_1) is the eigenvector that corresponds to the largest eigenvalue (λ_1). This eigenvector has a physical interpretation as the vector of propagation of particle motion; whereas, the eigenvalues are the radii of the best-fitting ellipsoidal.

The attribute polarizations are derived from the covariance matrix (Jurkevics, 1988):

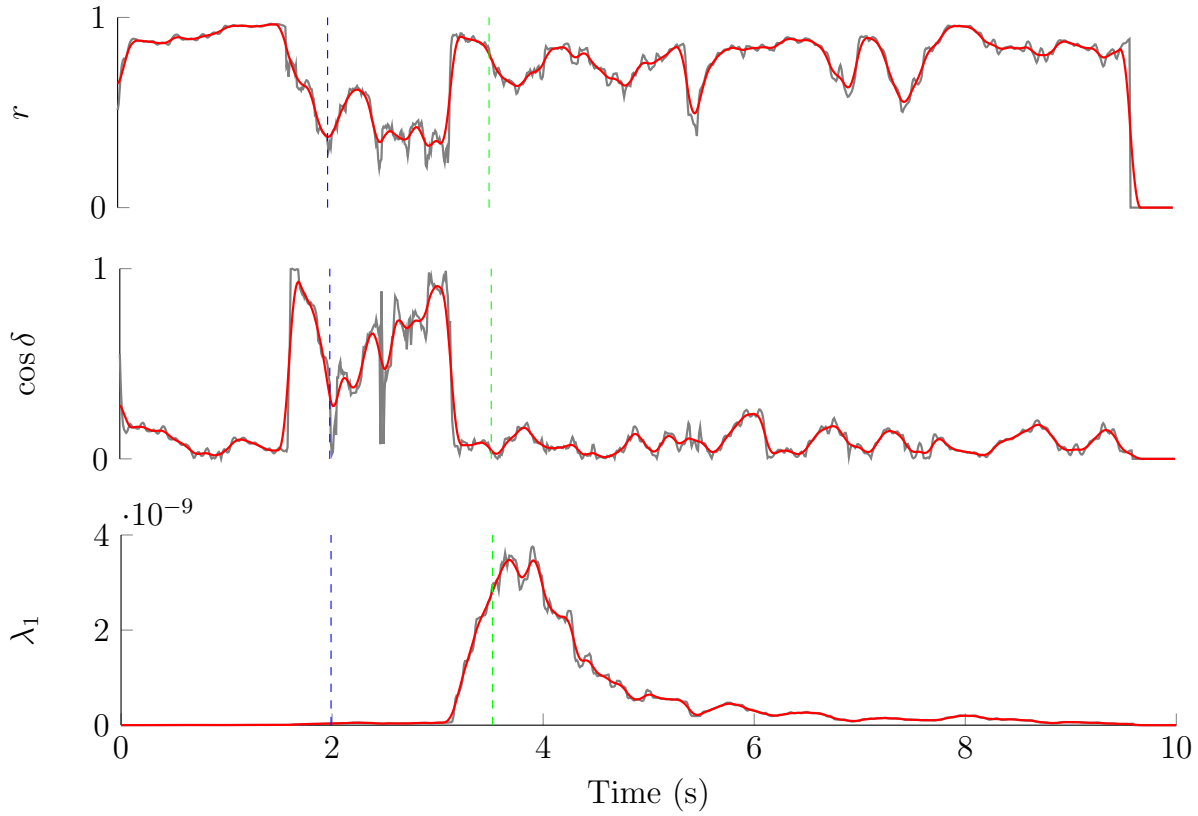

Figure 2.21: Attribute polarizations: (upper) rectilinearity, r, and (middle) vertical angle, $\cos\delta$. (lower) The first eigenvalue, λ_1 is also shown. These attributes are computed from particle velocity shown in Figure 2.20. The polarization analysis is conducted in a moving window having a size of 0.4s. The triangular smoothing (Claerbout & Fomel, 2014) with a window size of 0.1 s has been used. The curves before and after applying smoothing are shown in gray and red, respectively. The onset of P and S waves are indicated by blue and green lines.

- degree of linearity or rectilinearity,r.

$$r = 1 - \left(\frac{\lambda_2 + \lambda_3}{2\lambda_1}\right) \quad \text{with} \quad \lambda_1 \geq \lambda_2 \geq \lambda_3 \tag{2.33}$$

  Linear particle motion is indicated by very high λ_1 compared to other eigenvalues, then the value of rectilinearity is close to 1. Since body waves have linear polarization, their rectilinearity value is close to 1, $r \approx 1$.

- the apparent incidence angle,δ, measured from the vertical axis.

$$\delta = \cos^{-1} u_1 \tag{2.34}$$

For local seismic events, $\cos\delta$ would be close to 1 for P waves; whereas, it would be close to 0 for S waves (Ross & Ben-Zion, 2014). Figure 2.21 (middle) shows an example of the vertical incidence angle computed from the three-component seismogram (Figure 2.20). The P wave is indicated by a value of 1 ($\cos\delta \approx 1$), while the S-wave is close to 0; this attribute can then be utilized to differentiate P and S waves.

P- and S-phase characteristic functions

The P- and S- characteristic function can be utilized to pinpoint the location of seismic events using the diffraction stacking method (e.g., Grigoli et al., 2014). However, they should be handled separately using separately computed travel time (stacking operator) from the P- and S -wave velocity models. It then becomes necessary to separate the characteristic function of the P- and S-waves (CF^P and CF^S) before carrying out diffraction stacking. Grigoli et al. (2014) suggested that the computation of CF^P and CF^S can be conducted as follows:

- the CF^P is derived from the vertical component of a seismogram by computing its energy $CF^P = z^2$. z is the amplitude of a vertical component seismogram, while
- the CF^S is the largest eigenvalue of the covariance matrix between two horizontal components of a seismogram, $CF^S = \lambda_1^2$.

Attribute polarizations have been used in polarization filtering to enhance a particular phase or to separate one particular seismic phase from other seismic phases (Montalbetti & Kanasewich, 1970; Diallo et al., 2005). In this study, then, I utilized attribute polarizations to separate the P- and S-wave characteristic functions which are calculated using mAIC. From Figure 2.21, it can be seen that the P-phase characteristic function can be highlighted by multiplying the mAIC with the $\cos\delta$ function, while the S-phase characteristic function can be extracted by multiplying the $(1 - \cos\delta)$ function with mAIC. Furthermore, the rectilinearity can be used to magnify the strength of the body waves; thus, the P-phase characteristic function is defined as:

$$CF_i^P = mAIC(X_i)(r\cos\delta)^2 \quad \text{with} \quad i = 1, 2, 3 \tag{2.35}$$

X is the time series of a discretized seismogram of any component. Thus, $X_1 = \mathrm{Z}$, $X_2 = \mathrm{NS}$ and $X_3 = \mathrm{WE}$. The P-phase characteristic functions derived from each component

of the seismogram are shown in Figure 2.22. The P-phase characteristic function derived

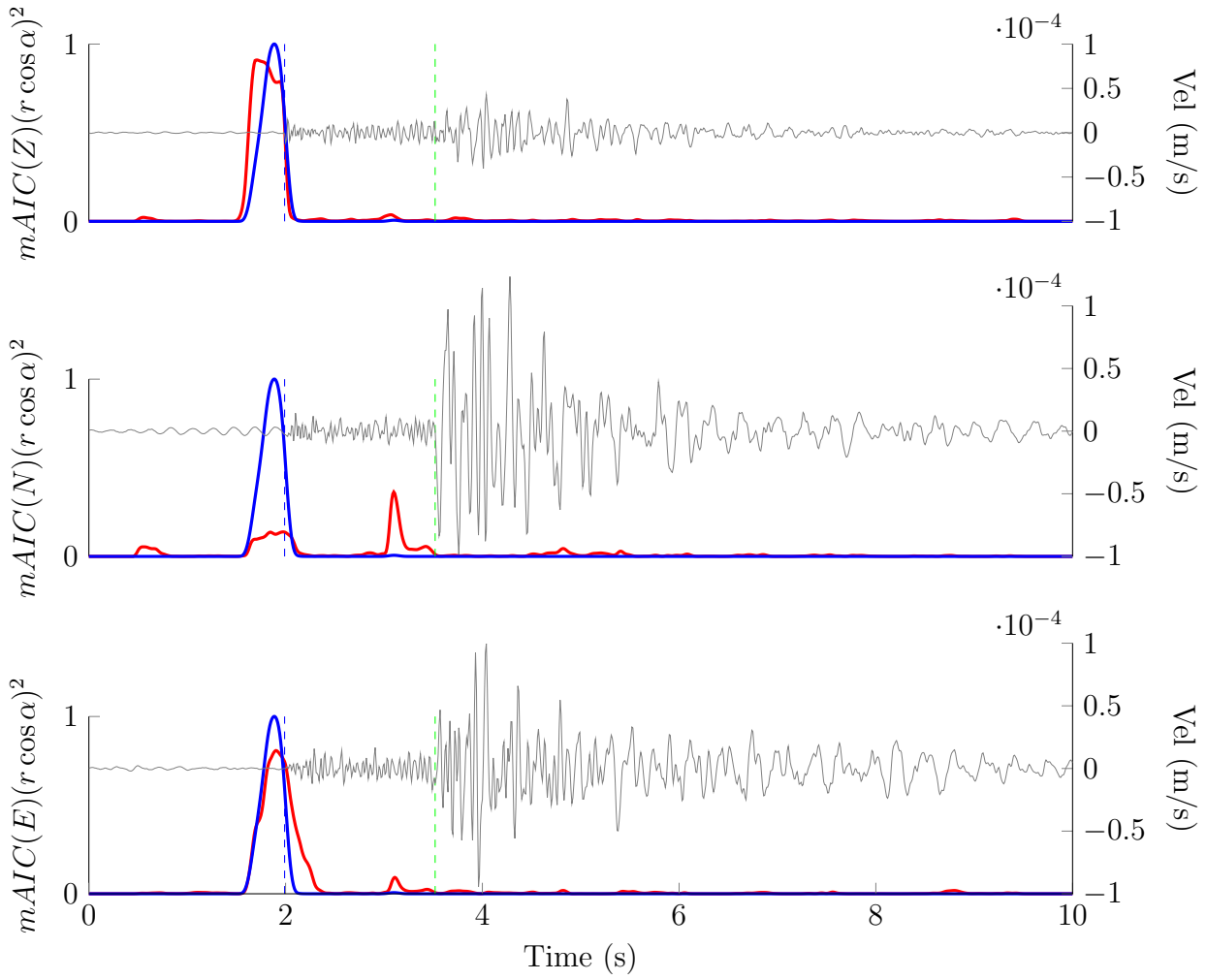

Figure 2.22: The P-phase characteristic function, CF_i^P, (red) computed from each Z, NS and WE component of particle velocity as shown in Figure 2.18. The final P-phase characteristic function is depicted by the blue line. The estimated onset of P- and S-waves is denoted by dashed blue and green lines, respectively. The final P-phase characteristic is normalized to its maximum.

from each component shows a coherent function around the onset time of the P-wave. To reduce noises, a multiplication between characteristic functions estimated from the three-component seismogram is conducted. Thus, the P-phase characteristic function can be expressed by:

$$CF^P = \left[mAIC(Z)(r\cos\delta)^2\right]\left[mAIC(NS)(r\cos\delta)^2\right]\left[mAIC(WE)(r\cos\delta)^2\right] \quad (2.36)$$

The final P-phase characteristic function for the seismic record shown in Figure 2.20 is indicated by the blue line in Figure 2.22. This curve clearly indicates the P waves, while

the S waves have disappeared. The removal of S waves becomes more effective after applying multiplication of the three mAIC functions.

By comparing the peak of the CF^P function with the manually estimated P-wave onset, a gap develops between them. The peaks of the CF^P function arrive earlier than the P-wave onset time. The width of the time gap depends on the size of the moving window used when computing the mAIC function.

The S-phase characteristic function is obtained by multiplying the mAIC function with the angle attribute polarization $(1-\cos\alpha)$ and the largest eigenvalue, λ_1. This would be:

$$CF_i^S = \left[mAIC(X_i)(1-\cos\delta)^2\lambda_1^2\right] \tag{2.37}$$

The final S-phase characteristic function is computed by utilizing the mAIC of the horizontal components NS and WE:

$$CF^S = \left[mAIC(NS)(1-\cos\delta)^2\lambda_1^2\right]\left[mAIC(WE)(1-\cos\delta)^2\lambda_1^2\right] \tag{2.38}$$

Unlike the final P-phase characteristic function, the final S-phase characteristic function is estimated only from the two horizontal components of a seismogram.

In Figure 2.23, the characteristic function no longer shows the P wave. Even if an artifact develops after the S wave, it will not lead to a significantly erroneous result since the measured coherency depends on the stacking operator. Since the peak of the S-wave characteristic function shows a better coincidence with the manually estimated S-wave onset time (the green dashed line), it is expected that utilizing the S-wave would improve seismic event location.

2.3 Diffraction stacking seismic event localization

2.3.1 Basic concept

The original concept of seismic event localization using the diffraction stacking method is derived from the active seismic of hydrocarbon exploration. In the active method, diffraction stacking is often called Kirchhoff Migration. It is an integral solution of the acoustic wave equation (Schneider, 1978). This was commonly used as a tool to collapse diffracted signals that emanate from any discontinuity. When the diffracted energies are recorded at surface sensors, those energies will be recorded along a surface called isochrone

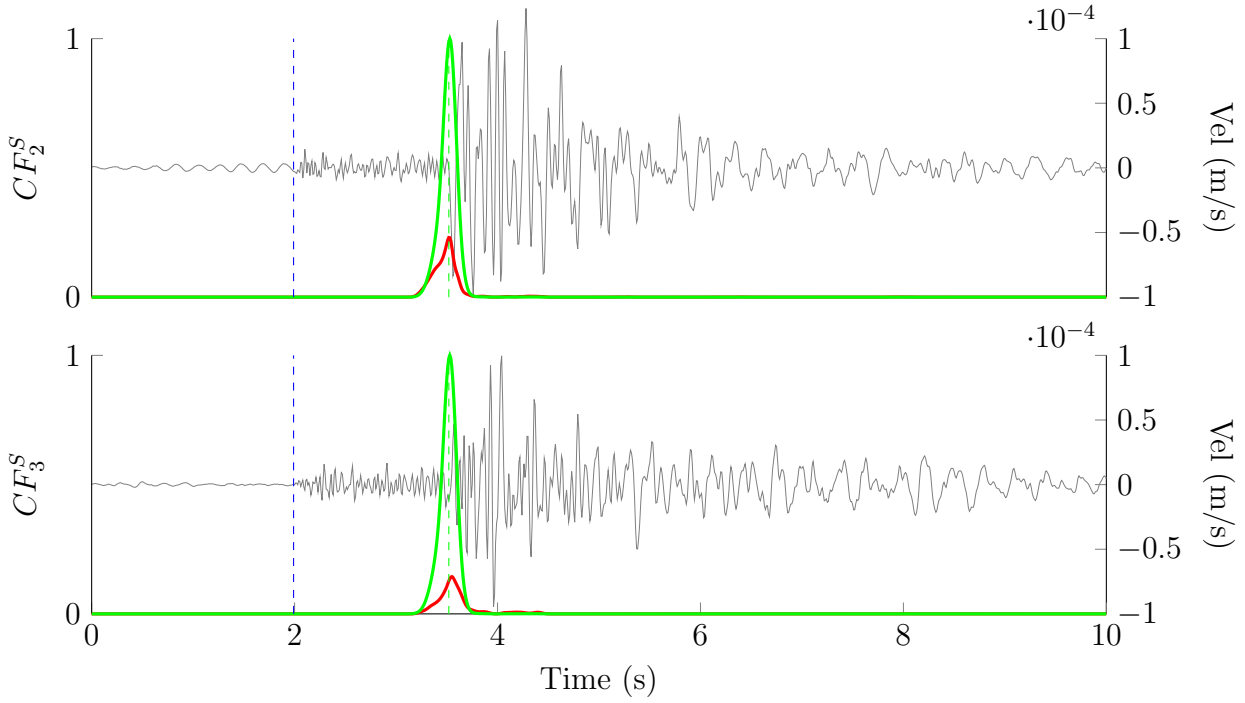

Figure 2.23: The S-phase characteristic function computed from individual components of the multi-component seismogram, CF_i^S (red), multiplication between individual S-phase functions (green), and the estimated P- and S-wave onset times (blue and green dashed line). The final S-phase characteristic function is normalized to its maximum value.

or travel-time surface. Later, this isochrone surface can be used to image or reconstruct the point of diffraction by summing up the diffracted signals along this surface. The isochrone surface is also called the stacking operator.

In a homogeneous velocity model, the isochrone surface (or curve in two-dimensional media) can easily be reconstructed, as illustrated in Figure 2.24. This figure shows the number of rays (black dashed lines) that emanate from a single point (point scatterer) in different directions. These rays travel through the velocity model $v(x_1, x_2)$ and eventually reach receivers installed on the surface. The arrival times of the rays will coincide with the isochrone curve. Hence, once the velocity model is known, the isochrone can be modelled (using an isochrone operator $t(x)^2$), and it can be used to image a point diffractor through the amplitude summation along this isochrone curve. This concept was thus adopted in determining seismic event location.

Assuming that the velocity model is provided, the isochrone curve for each grid (all grids are possible seismic event locations) at a discretized sub-surface model can be modelled. The resulted value from the summation of amplitudes along the isochrone curve is

assigned to the corresponding grid point. Finally, all of the grids are represented by the summation/stacking value.

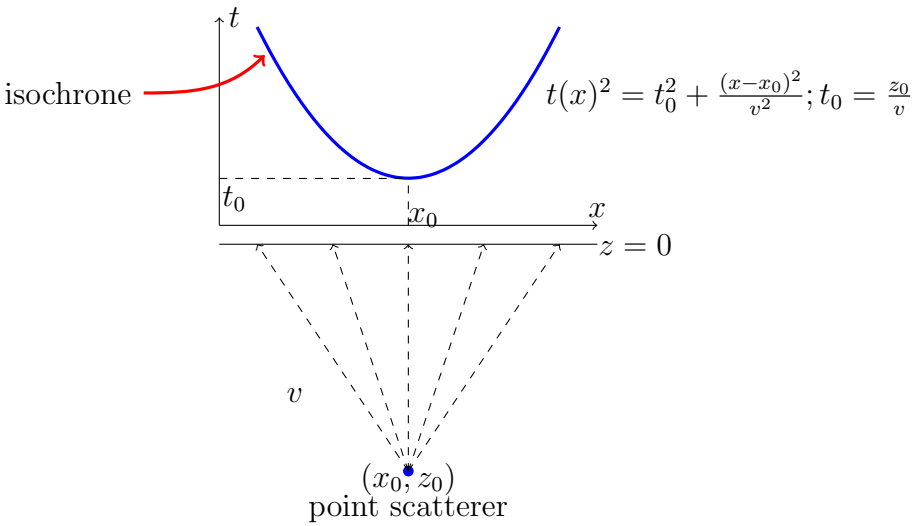

Figure 2.24: The travel time curve (isochrone) corresponds to a point diffractor in the subsurface. This travel time curve is reconstructed using the hyperbolic equation: $t(x)^2$.

Microseismic data is often recorded by sensors distributed over a certain surface area; hence, a three-dimensional model is required. The summation surface in 3D media for a single (homogeneous) velocity, v, can be expressed as follows:

$$t^2(x) = t_0^2 + \frac{(\vec{x} - x_0)^2}{v^2} + \frac{(\vec{y} - y_0)^2}{v^2} \tag{2.39}$$

t_0 is the travel time of an image ray which arrives perpendicular to the surface plane and is approximated by z/v. A graphic representation of Equation 2.39 is shown in Figure 2.25.

In the case of 3D media, the diffracted energy is summed up along the 3D isochrone. Similar to the 2D isochrone, the 3D isochrone represents the arrival time of rays at each receiver traveling from an assumed point diffractor through the assumed velocity model.

The hyperbolic form of this isochrone curve is only valid for a homogeneous velocity model (single value velocity). For a heterogeneous velocity model that resembles complex geological structures, one needs to numerically solve the Eikonal equation in order to develop the 3D isochrone surface. The computation of this summation operator plays a critical step in diffraction stacking since the migration will be carried out along this operator. The more accurate the summation operator, the better the migration results (seismic event location) will be. The Eikonal equation is the high frequency approximation

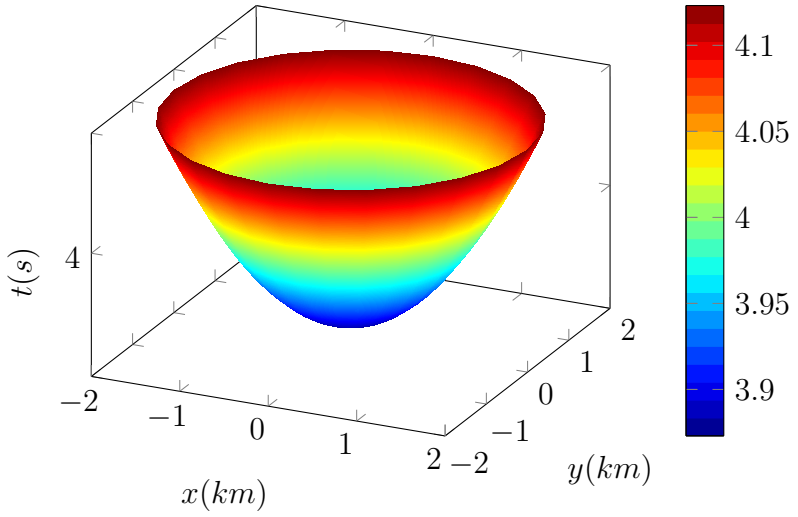

Figure 2.25: The 3D isochrone for homogeneous velocity of $\sqrt{2}$ km/s and the point diffractor is located at a depth of $\sqrt{30}$ km beneath the surface position (0,0).

of a wave equation, which is expressed as follows:

$$|\nabla\tau|^2 = \frac{1}{v(\vec{x})^2} \tag{2.40}$$

where $\tau(\vec{x})$ is the travel time of the energetic wave field (wavefront). Equation 2.40 can be solved numerically using numerous techniques, such as finite difference (Vidale, 1988; van Trier & Symes, 1991; Podvin & Lecomte, 1991; Tryggvason & Bergman, 2006), wavefront construction (Vinje et al., 1993), and fast marching methods (Sethian & Popovici, 1999). The travel time computed by solving the Eikonal equation using one of the aforementioned algorithms is also called Green's function. In this study, I computed Green's function to construct the summation surface by making use of the code developed by Podvin & Lecomte (1991).

The summation process can be formulated as follows (Biondi, 2006):

$$I(\vec{x}) = \int_{\Omega} W(\vec{x}, \vec{x}_0; t)\psi(\vec{x}_0; t_D)d\vec{x}_0 \tag{2.41}$$

$\psi(\vec{x}_0; t_D)$ is the observed wavefields or recorded seismogram, I is the summation/stacking value (represented in the discretized image domain $\vec{x}$) from seismograms recorded at the surface x_0. t_D is the summation operator (isochrone surface). In other words, t_D is the amount of time needed by a particular ray to travel from an image point $\vec{x}$ to receivers located at $\vec{x}_0$. The integral operator computes summation over the aperture size Ω, which is the seismometer network coverage.

The discrete form of equation 2.41 is expressed as:

$$I(\vec{x}) = \sum_{i=1}^{N_{rec}} W(\vec{x}, \vec{x}_{0i}; t)\psi(\vec{x}_{0i}; t'_0 + t_D) \tag{2.42}$$

N_{rec} is the number of actual seismograms that record data. $W(\vec{x}, \vec{x}_0)$ or weighting function is only required if the true-amplitude summation image, $I(\vec{x})$, is expected. The obliquity factor and amplitude correction compose this weighting function. The true-amplitude image is only needed if one is interested in estimating the petrophysical parameter (in terms of active seismicity). In the case of a migrating seismogram, the term "true-amplitude" means that the amplitude conveys a particular physical meaning such as the magnitude of an earthquake. The computation of the weighting function can be found in Cohen & Bleistein (1979) and Schleicher et al. (1993). However, since I only focus on seismic event location, it is not required to preserve the true amplitude as I would then neglect the weighting function. The weighting function in seismic event localization; however, can be connected to a radiation pattern correction or weighting for reduction of acquisition footprints (Canning & Gardner, 1998). Moreover, to avoid complicated radiation patterns, imaging using the Kirchhoff-like method is usually conducted on the absolute value of the seismograms (Reshetnikov, 2013; Kao & Shan, 2004). Hence, for this purpose, the summation process can be expressed as:

$$I(\vec{x}) = \sum_{i} |\psi(\vec{x}_{0i}; t'_0 + t_D)| \tag{2.43}$$

To reduce noise contribution and make the summation more robust, the amplitude summation can be done within a window (i.e., Kao & Shan, 2004). Hence, equation 2.43 now becomes:

$$I(\vec{x}) = \sum_{ti=t'_0-T/2}^{t'_0+T/2} \sum_{i=1}^{N_{rec}} |\psi(\vec{x}_{0i}; ti + t_D)| \tag{2.44}$$

T is the window length that depends on the dominant frequency of the seismic amplitude data.

2.3.2 Seismic event localization using the diffraction stack method

The diffraction stacking method used in this study differs from travel-time-based localization methods in many aspects. In the travel-time-based methods, the seismic event location is computed iteratively by applying model perturbation to the initial model based

on the type of objective function used. The final model (the seismic event location and its origin time) is obtained when the lowest misfit between calculated and observed travel times is achieved. In contrast to travel-time-based localization methods, the diffraction stacking method is a forward modeling problem. A number of guest models are considered as candidates for the final model, and the objective function (can also be referred to as the coherency function) is evaluated for each model. The highest coherence is sought, since it is associated with the final model. The models can be provided by discretizing the subsurface model regularly in a fixed grid size. A priori information can be introduced to constrain model space. The coherency at each grid, in a model space, is measured along the coherency (previously called summation, stacking, or isochrone surface) operator. Several coherency measures have been used in the diffraction stacking method, such as:

- Stacking (Gajewski et al., 2007; Grigoli et al., 2014). The coherency is measured by summing up the amplitude of the seismogram along the coherency operator.

- Semblance (Staněk et al., 2015). The coherency is computed using the following equation:

$$I(\xi, t_0) = \frac{(\sum_{k=1}^{N_{rec}} \psi_k(\xi; t_R + t_0))^2}{N_{rec} \sum_{k=1}^{N_{rec}} \psi_k^2(\xi; t_R + t_0)} \tag{2.45}$$

  ψ is the amplitude of a recorded seismogram, t_R is the traveltime from a position ξ to a receiver k, t_0 is an assumed origin time and N_{rec} is the number of the seismogram.

- Median (Hansen & Schmandt, 2015). The median is considered as a more robust coherency measure than stacking (mean value), as the median is not affected by spurious high amplitudes (outliers).

General seismic event determination using diffraction stacking is conducted in several steps, as described in the following (see Figure 2.26):

1. Discretize the subsurface model represented by model velocity into grids of the so-called image point. This image point is then considered as a possible location of seismic events.

2. Choose one grid (ξ_j) then compute the travel time (t_{jk}) from the chosen grid to a particular receiver (x_j).

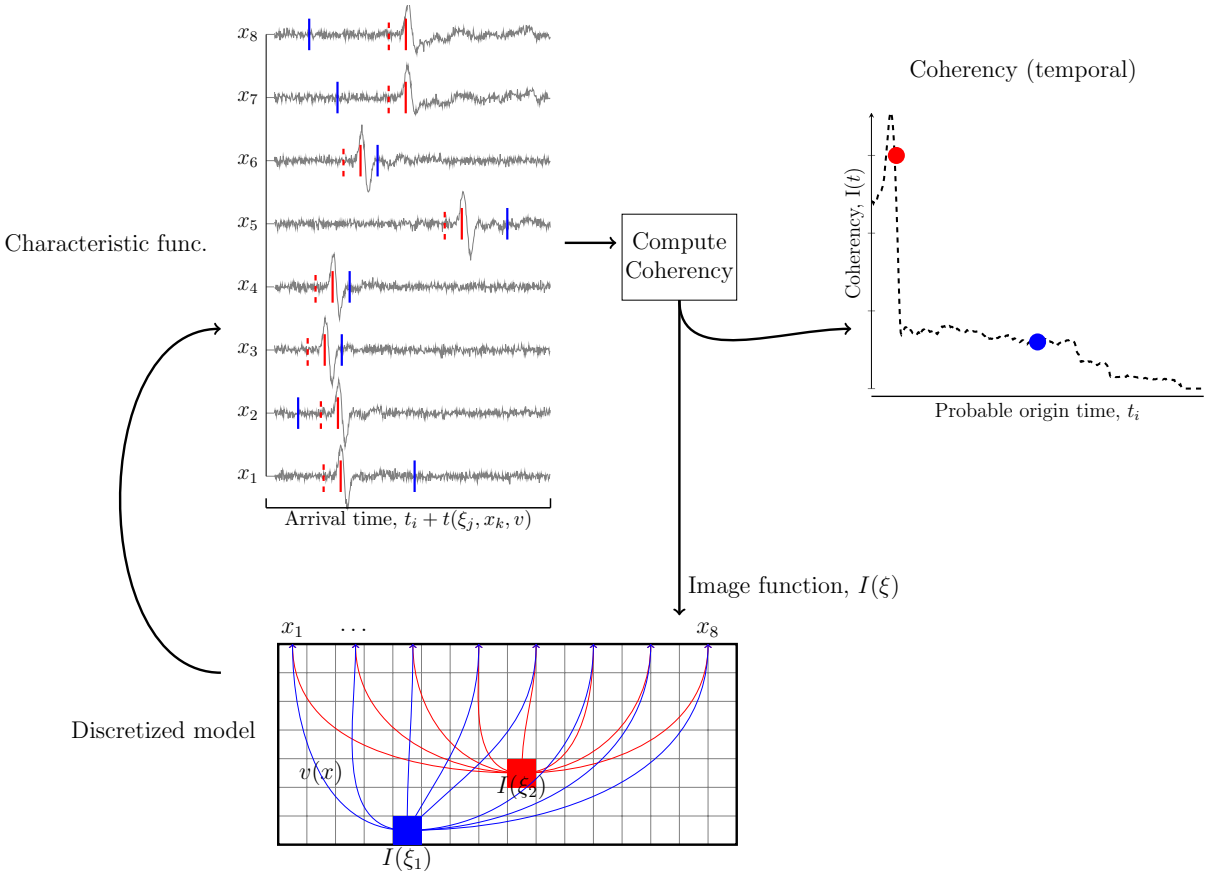

Figure 2.26: The concept of determining seismic event location and the corresponding origin time using the diffraction stacking method. A subsurface that is represented by the velocity model is discretized. All nodes are considered as candidates for seismic event location. By then choosing one node, ξ_j, the time (t_{jk}) required by rays to travel from ξ_j to a certain receiver, x_k, can be computed. The amplitudes of recorded seismograms along the t_{jk} are stacked (as a measure of coherency). The stacked value is assigned to temporal and spatial domains.

3. Choose the time position, t_i, as a guest for origin time. By combining this value with the travel time t_{jk}, the coherency operator (t_{ijk}) can be built. The coherency operator is expressed by:

$$t_{ijk} = t_i + t_{jk} \tag{2.46}$$

In this study, stacking has been chosen as the method to measure coherency. I prefer to use mean (stacking) rather than median, as only a limited number of seismometers (42) are available in data sets used this study.

4. Stack the amplitudes along the stacking operator,

$$I(t_i, \xi_j) = \sum_{t_w=-T/2}^{+T/2} \sum_{k=1}^{N_{rec}} \psi(\xi_j; t_{ijk} + t_w) \tag{2.47}$$

ψ is the amplitude of a recorded seismogram. In this study, I used the mAIC characteristic function instead of the original amplitudes. The first summation running from $-T/2$ to $T/2$ indicates that the stacking is conducted within a time window with a size of T. The weighting function can be applied within this window. The choice of weighting window depends on the noise level of the seismogram and the accuracy of the velocity model. Kao & Shan (2004) suggested that, for noisy data and inaccurate velocity models, equal weighting is more appropriate. While for high quality data and accurate models, the Gaussian weighting function should be considered (Kao & Shan, 2004). The use of a weighting function in the Kirchhoff-like migration is for obtaining a true-amplitude image (see equation 2.41). However, in diffraction stacking, its usage is to accommodate the uncertainties of the velocity model and coherency operator.

Stacking the amplitudes of a particular grid location is carried out several times over a time axis, which is a candidate for the origin time. The solid and dashed red lines in the recorded seismogram (see Figure 2.26) illustrate the two stacking operators corresponding to the nodal point ξ_2 but with different origin times. From the figure, it is obvious that the stacking amplitude value resulted from the summation along the solid red line is higher than that of the dashed line.

5. Find the maximum stacked amplitude:

$$I(\xi_j) = \max_{t_i}\{I(\xi_j, t_i)\} \tag{2.48}$$

In this step, simply collapse the time axis of the function $I(\xi_j, t_i)$. The maximum stacked amplitude, $I(\xi_j)$, is regarded as the coherency of the corresponding grid, $I(\xi_j)$. Then, assign the stacked amplitude to the nodal point ξ_j. Collapsing the time axis does not mean ignoring the origin time. The origin time information can be retrieved from the next step.

6. Repeat the above procedure to all image points (nodal point) to construct spatial,

$I(\xi)$, and temporal, $I(t)$ coherency.

$$I(t_i) = \max_{\xi_j}\{I(\xi_j, t_i)\} \tag{2.49}$$

7. Find the seismic event location, ξ_0, and its origin time, t_0, by finding the maximum stacked amplitude at the coherency function $I(\xi)$ and $I(t)$,

$$\begin{aligned} \xi_0 &= \max_{\xi}\{I(\xi)\} \\ t_0 &= \max_{t}\{I(t)\} \end{aligned} \tag{2.50}$$

2.3.3 Combining P- and S- image function

After diffraction stacking is applied to the characteristic functions CF^P and CF^S, two image functions (I^p and I^s) will be obtained. These images carry information about the location of seismic events which can be retrieved by searching the maximum coherency from each of the three-dimensional image functions. There is a possibility that the seismic event locations retrieved from the P- and S- image functions will be different. This is mainly caused by different capabilities (effectiveness) of the P- and S-phase characteristic functions in detecting the onset of P- and S- waves. These two image functions are then reconciled to estimate the final seismic event location that is constrained by P- and S-wave information.

One approach for reconciling the P- and S- image functions is employing normalized multiplication between I^p and I^s (Grigoli et al., 2014),

$$I^{ps} = \frac{\sqrt{I^p I^s}}{N_s} \tag{2.51}$$

N_s is the number of the station.

In this work, I proposed to reconcile the P- and S- image functions by employing the covariance analysis approach. The covariance matrix was computed at each spatial location by involving n points surrounding the location being investigated. If the P- and S- image function is represented by $I^p(i,j,k)$ and $I^s(i,j,k)$, then the covariance between P- and S- image functions (I^{ps}) at the location being evaluated of (i^{th}, j^{th}, k^{th}) can be expressed by:

$$cov(I^p, I^s) = \begin{pmatrix} I^{pp} & I^{ps} \\ I^{ps} & I^{ss} \end{pmatrix} \tag{2.52}$$

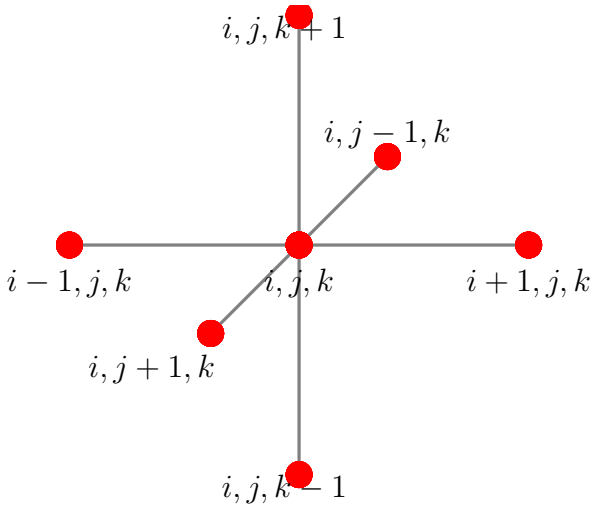

Figure 2.27: The samples included in the computation of the covariance matrix of point being evaluated (i, j, k). $n = 1$ has been assumed.

with,

$$I^{ps}(i,j,k) = \sum_{a=-n}^{n} I^{p}(i+a,j,k)I^{s}(i+a,j,k) + \sum_{b=-n}^{n} I^{p}(i,j+b,k)I^{s}(i,j+b,k) + \sum_{c=-n}^{n} I^{p}(i,j,k+c)I^{s}(i,j,k+c) \quad \text{with} \quad b,c \neq 0 \tag{2.53}$$

In case of $n = 1$, the covariance at the point (i, j, k) is calculated by including all the samples as described in Figure 2.27. Two eigenvalues (λ_1 and λ_2) are then determined from the covariance matrix. The largest eigenvalue (λ_1) is considered as the image representing P- and S-image functions. Figure 2.28 shows the comparison between P-, S-, and PS-image functions resulting from covariance analysis.

Table 2.1: The location of maximum coherency of image functions shown in Figure 2.28. PS(cov) is the location of the maximum coherency of the image function computed by covariance analysis. Whereas in PS(mul), the location of maximum coherency is calculated from the image resulting by the multiplication of P- and S- images.

	P	S	PS(cov)	PS(mul)
WE	21.5	24	24	23.5
NS	37.5	39.25	39.25	39.25

By examining the maximum coherency at each image function (Table 2.1), it can be seen that the final location of a seismic event could be close to the maximum S- (as

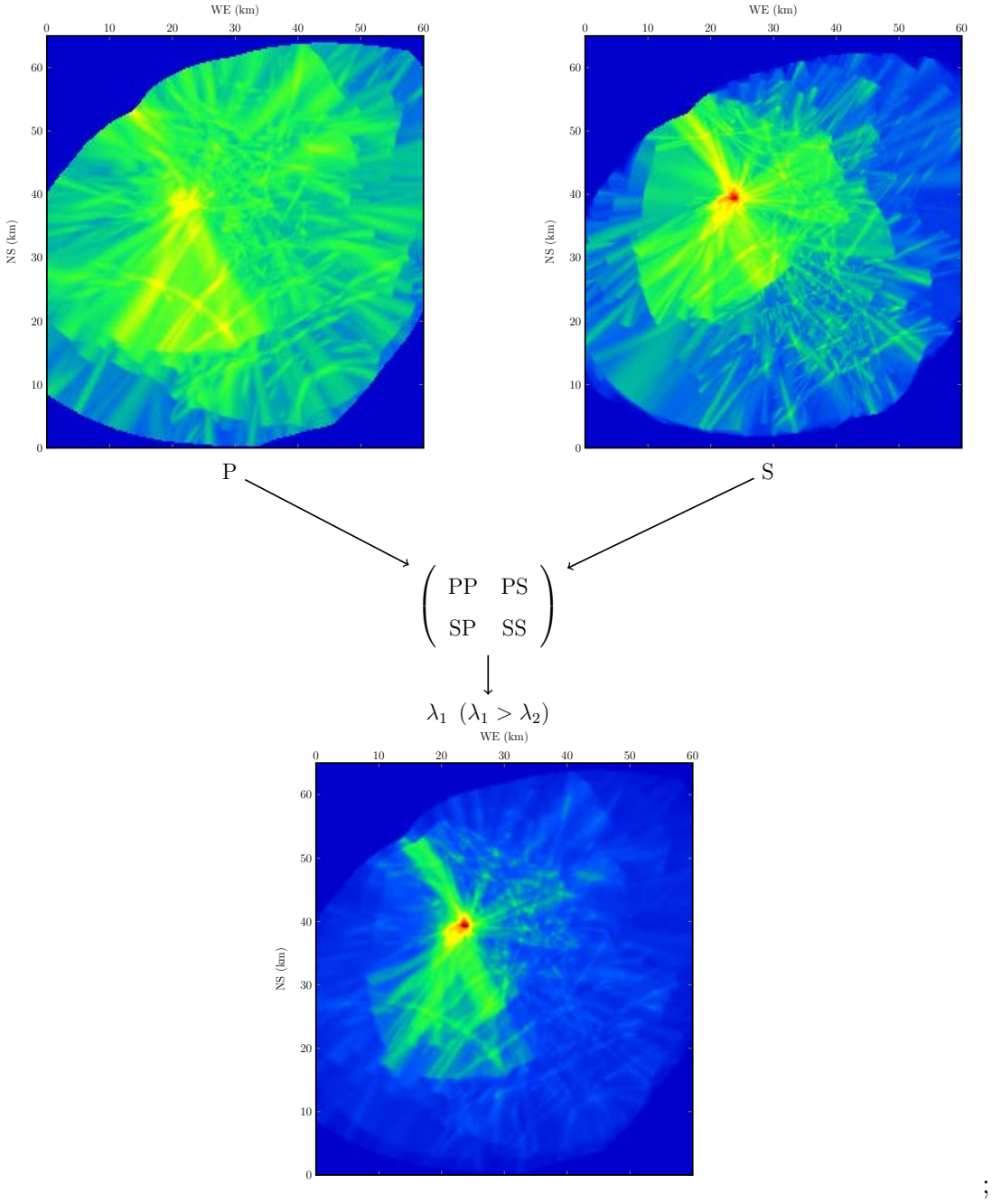

Figure 2.28: Joining the P- and S- image functions by computing the covariance matrix between P- and S- coherency image functions. The covariance is performed by involving one sample surrounding the point being evaluated. The maximum coherency can be seen in Table 2.1. The grid size is 0.25 km.

well as P-) image, or even unrelated to both maximum P- and S- images, depending on the number of samples surrounding the point being evaluated that are included in the calculation. Before computing the PS image, it might be better not to apply normalization to the P- and S- images. The original value of the coherencies are preserved as these

resulted from the diffraction stacking. The coherence in image function represents the number of coherent events along the stacking operator. The above table also reveals that the location of the event is closer to the location estimated from the S-image rather than the P-image. This means that the S-image shown in this figure represents a more coherent event when compared to the P-image.

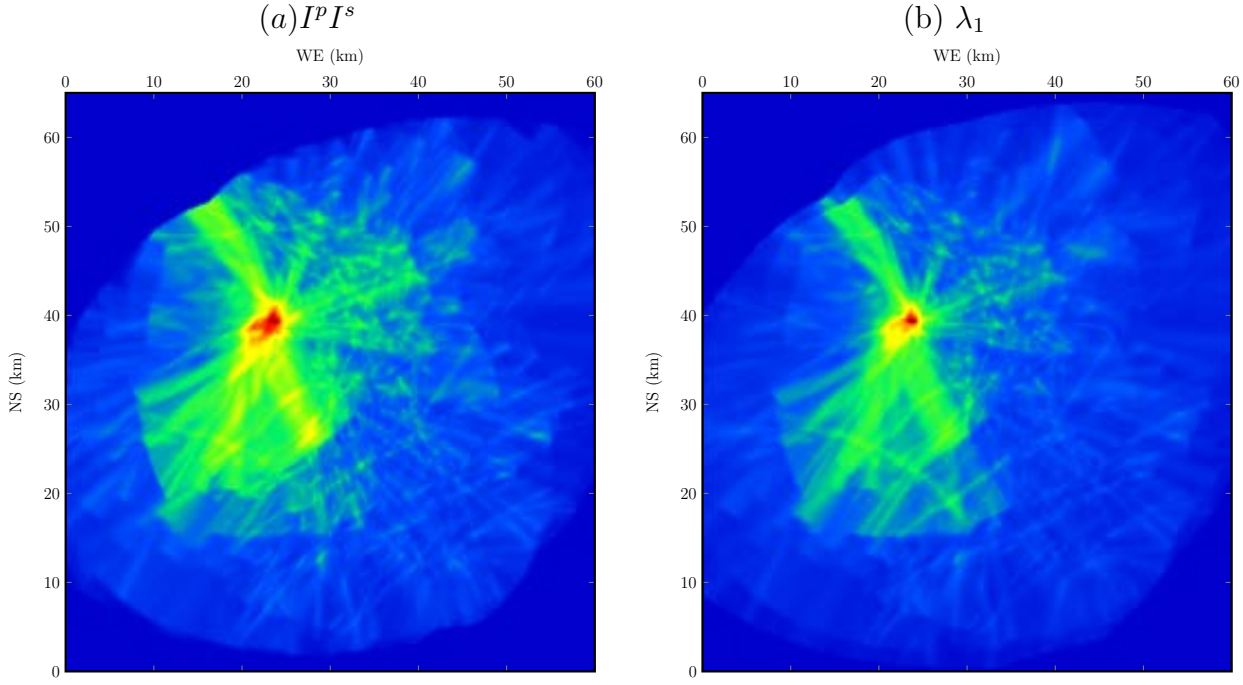

Figure 2.29: Comparison of the PS image function resulted by calculating (a) multiplication and (b) the largest eigenvalue of the covariance matrix. The images are normalized to their maximum value. The comparison of location of maximum value is shown in Table 2.1.

Figure 2.29 provides some insight into the difference between covariance analysis and multiplication. At a glance, they look similar. By combining Equation 2.32 and 2.52 , it can be easily proven that for $n = 0$ the image of covariance analysis has the value,

$$I^{ps}_{cov}(i,j,k) = (I^p(i,j,k))^2 + (I^s(i,j,k))^2 \tag{2.54}$$

while for the multiplication:

$$I^{ps}_{mul}(i,j,k) = \sqrt{I^p(i,j,k)I^s(i,j,k)} \tag{2.55}$$

Note that the normalization by number of stations (N_s) has been neglected by Equation 2.55. The covariance results for $n = 0$ as shown in Equation 2.54 are consistent with

the objective function used by Gharti et al. (2010) to find the seismic location using the diffraction stacking approach,

$$I^{ps} = I_L^2 + I_Q^2 + I_T^2 \tag{2.56}$$

L, Q and T are the rotated seismograms in the local ray coordinate system.

2.3.4 The maximum and statistical location of a seismic event

Unlike traditional seismic event localization which results in dot-like seismic events, the output of the diffraction stacking method is in the form of an image function. The final seismic event can be presented in amplitudes (image), point of maximum image function (i.e., Gajewski et al., 2007; Chambers et al., 2013; Grigoli et al., 2014), and points computed using a statistical approach (Anikiev et al., 2014) or the density of the seismic event (Hansen & Schmandt, 2015). The image representation is well-suited for imaging tremor-like events (Steiner et al., 2008) in which it is not possible to recognize the onset of first arrivals. When the seismic event can be identified from the recorded seismogram, it is possible to represent the seismic event location by a point, which is common in traditional approaches.

Maximum image function

The seismic event location, $\mathbf{x}_0$, is defined as,

$$I(\mathbf{x}_0) = \max\{I(\mathbf{x})\} \tag{2.57}$$

$I(\mathbf{x})$ is an image function whose values represent the stacking amplitude over the diffraction/stacking operator.

Statistical approach

After the four-dimensional image function is available, the location of a seismic event can be estimated by simply locating the maximum stacking amplitude value. However, by using this approach, the located seismic event is limited by the voxel size. To obtain more accurate results, the grid size can be reduced; nevertheless, processing time increases eight-fold for halving the voxel size. Another downside of this approach is that the located seismic event might lead to the wrong location due to noise contamination (outliers). To overcome these drawbacks, Anikiev et al. (2014) suggest transforming the image function

into a probability density function (pdf). By using this method, the location of a seismic event is not limited to the nodal points. Moreover, it makes it possible to estimate the uncertainty of the locations. The following steps outline the procedure for event location determination from image functions:

1. Convert the image function, $C(\vec{x})$ into a probability density function (i.e., Tarantola, 2005) by using the following equation:

$$P(\vec{x}) = c.exp\left[-\frac{(C(\vec{x}) - max(C(\vec{x})))^2}{2\sigma^2}\right] \tag{2.58}$$

   c is a constant to satisfy that $\int P(\vec{x}) = 1$.

2. Compute the seismic event location, $\vec{x}_0(x_0, y_0, z_0)$:

$$x_0 = \sum_x \left(x \sum_{y,z} P(\vec{x}) \right) \tag{2.59a}$$

$$y_0 = \sum_y \left(y \sum_{x,z} P(\vec{x}) \right) \tag{2.59b}$$

$$z_0 = \sum_z \left(z \sum_{x,y} P(\vec{x}) \right) \tag{2.59c}$$

3. Estimate the corresponding uncertainties:

$$\sigma_x = \pm\sqrt{\sum_x \left((x - x_0)^2 \sum_{y,z} P(\vec{x}) \right)} \tag{2.60a}$$

$$\sigma_y = \pm\sqrt{\sum_y \left((y - y_0)^2 \sum_{x,z} P(\vec{x}) \right)} \tag{2.60b}$$

$$\sigma_z = \pm\sqrt{\sum_z \left((z - z_0)^2 \sum_{x,y} P(\vec{x}) \right)} \tag{2.60c}$$

Chapter 3

Synthetic Tests

The concept of seismic event localization using diffraction stacking methods was introduced in the previous chapter. Based on this concept, a localization method aiming to pinpoint the location and origin time of a seismic event has been formulated in a general, three-dimensional case. The performance of the proposed localization method will be demonstrated and evaluated using synthetic test examples in this chapter. The objective of the synthetic exercises is validating the developed code and to evaluate the accuracy of the located seismic events. In order to realize this purpose, the same velocity model was used for both generating the synthetic seismogram and localizing the seismic events.

The X, Y, and Z components of a synthetic seismogram were generated using the predefined three-dimensional velocity model. The characteristic function was computed from a seismogram which was represented in these various particle motions: acceleration, velocity and displacement. The particle motion that yields the most accurate results is considered the appropriate particle motion for processing field data.

The ability of the characteristic function generator to indicate the onset of P and S waves is a critical aspect in seismic event localization. The characteristic function generator was tested against synthetic seismograms resulting from four different source models: (1) isotropic (ISO), (2) double couple (DC), (3) compensated linear vector dipole (CLVD), and (4) a combination of the ISO, DC and CLVD models. In order to evaluate accuracy, the seismic event locations resulting from the different particle motions and the source models were compared. A comparison of seismic locations between those computed from the original seismogram and the characteristic function was also conducted.

Different noise levels were introduced to the synthetic seismograms. The Signal-to-

Noise Ratio (SNR), which is defined as the ratio between Root-Mean-Square (RMS) amplitudes of signal and noise, is used to quantitatively measure the amount of contaminated noise on the original synthetic seismogram. By using synthetic seismograms with different noise levels, the robustness of the characteristic function generator can be evaluated.

The seismic event locations produced by the diffraction stack differed from those computed by the classic travel-time-based method. The event locations resulting from the classic event localization methods are represented by a dot-like form, while the diffraction stacking methods initially represent the results in an image; i.e., the so-called image function volume. However, it is beneficial to transform the image function volume to a dot-like form so that the misfit between the original and the estimated source location can be quantified (in case of synthetic data). The location of a seismic event can be computed from the image function volume by determining the maximum value of the image function (Gajewski et al., 2007; Chambers et al., 2013) or by transforming the image function into the probability density function (Anikiev et al., 2014).

3.1 Velocity model, seismic source model and synthetic seismogram

The synthetic experiment was conducted using acquisition parameters resembling the actual passive seismic survey. This implies that parameters such as:

- velocity model,
- seismometer distribution, and
- hypothetical source locations

were chosen as they were used in the Tarutung passive seismic experiment in Sumatra (Muksin et al., 2013).

This simulation used the velocity model of P and S waves derived from the recorded seismogram using the travel time tomography method (Muksin et al., 2013). The velocity model portrays the complexity of the Tarutung and Sarulla pull-apart Basins developed by the dextral strike-slip Sumatran Fault. This velocity model can be divided vertically into three parts (Muksin et al., 2013): (1) the uppermost layer, going down to a depth

of 4 km from the surface (in this simulation, the surface is defined at $z = 0$) ; (2) the middle part; and (3) the deeper part. The upper layer is dominated by low velocity values that span between 3-4 km/s (P-wave), and these structures represent the sediment filling the pull-apart basin. The middle part is characterized by P-wave velocities ranging from 4 to 5 km/s, and the deeper part is occupied by higher P-wave velocities between 5-6 km/s. A significant lateral velocity variation occurs at the uppermost layer, since the Tarutung and Sarulla Basins exist at these depths. Furthermore, the shear wave speeds range between 1.6 and 4 km/s. The model has a dimension of 60 by 65 km in West-East and North-South directions, respectively, with a depth of 18 km. The average density of the continental crust (granitic rock) of 2670 kg/m^3 (Hinze, 2003) was used to represent the homogeneous density model. For synthetic modeling, a flat surface ($z = 0$) was assumed instead of rugged topography. The seismometer distribution (red triangles) as well as 100 hypothetical event locations (black dots) are shown in Figure 3.1.

The simulation was conducted using SPECFEM3D Cartesian (i.e., Tromp et al., 2008), an open-source software suite for synthetic seismogram simulations based on the spectral element method. In the first step, a regular mesh with 12 and 13 spectral elements along the X and Y directions respectively, was used. Additional spectral elements along the depth axis were combined; a total of 5616 elements were then implemented. The simulation was conducted for 2500 time steps with a sampling frequency of 125 Hz (or time sampling of 8 ms), and 20s long-seismograms were produced. An absorbing condition scheme was implemented on all sides, including the top surface. The free surface was not implemented to avoid the interference of surface-related reflections from later arrivals.

The source-time function is selected by defining the half-duration of the rupture process. A practical application was chosen in this simulation by specifying the source-time function as zero half-duration or moment-rate with delta function. To produce a synthetic seismogram, after a simulation is conducted, the seismogram (impulse response) is convolved with the desired time function (Komatitsch & Tromp, 2002). In this synthetic experiment, the resulting impulse response was convolved with a triangular source-time function with a half-duration of 0.25s to produce the synthetic seismograms.

Most earthquake source mechanisms can be well-approximated by using the double-couple (DC) model representing equivalent forces due to shear failure on a simple planar plane (i.e., Vavryčuk, 2015). DC source models can be associated with strike-slip, dip-slip,

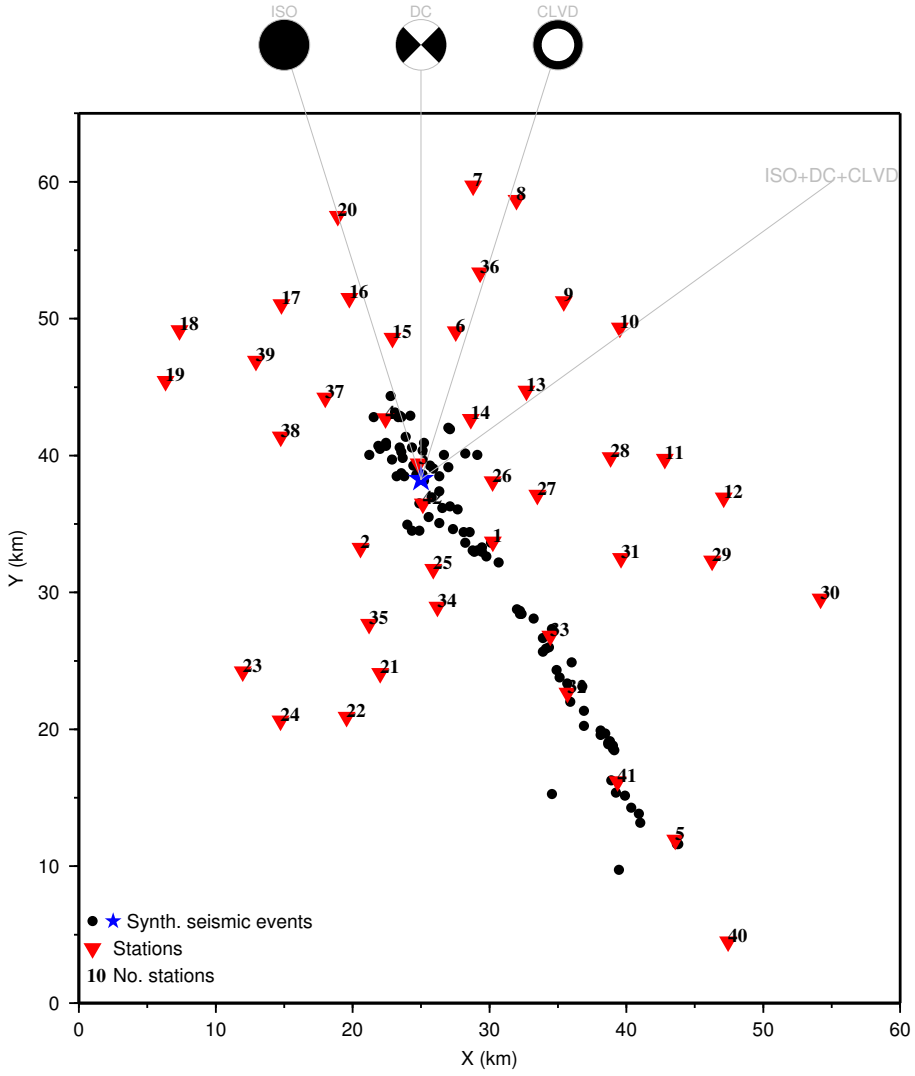

Figure 3.1: Distribution of the 42 seismometers (red) and 100 seismic events (black) used in this synthetic simulation. Four kinds of source mechanisms were used to simulate a synthetic seismogram at the same location (blue star): explosion (isotropic), strike-slip (double couple, DC), compensated linear vector dipole (CLVD), and a combination of isotropic DC and CLVD.

and reverse slip faults on a planar fault plane. However, a significant number of non-DC components are observed, particularly in volcanic and geothermal areas (Julian, 1983; Julian et al., 1998).

A non-DC component moment tensor consists of an explosion or implosion (isotropic component) and a compensated linear vector dipole (CLVD). Julian (1983) showed that a non-DC source model in a volcanic area could be explained using a CLVD model. The non-DC component was also observed in the aftershock of the 1999 Izmit Earthquake (Stierle

et al., 2014). Explosion and implosion components were reported to have taken place in the Geysers geothermal field (Ross et al., 1999) and the Hengill-Grensdalur geothermal area (Julian et al., 1997). This could be related to the collapse of a cavity or an opening which occured during fluid extraction or injection. The CLVD model can represent an equivalent force introduced by an opening crack caused by tensile failure under high fluid pressure (Julian, 1983), and a rupture along the curve plane (Kubas & Sipkin, 1987). Tensile failures occur, for example, when fluid injection in a geothermal field takes place(Foulger, 1988), or due to dike intrusion (Julian, 1983). Hence, the seismic event associated with fluid injection or extraction in a geothermal area would exhibit the CLVD source model.

In general, any source mechanism can be modeled by considering the contribution from DC and non-DC components. Hence, decomposing a moment tensor into three elementary parts (DC, explosion/implosion, and CLVD) was used to performed before interpreting the source model of an earthquake (Vavryčuk, 2015).

As a first step, I determined a seismic event located at a specific point (X=24.994; Y=38.273; and Z=7.88 km) (see Figure 3.1). At this location, four seismic events with different moment tensors were simulated:

1. An explosion source model was chosen to represent the isotropic component of a source mechanism. This isotropic component was expressed by the following moment tensor:

$$\begin{pmatrix} 1 & 0 & 0 \\ 0 & 1 & 0 \\ 0 & 0 & 1 \end{pmatrix} \tag{3.1}$$

2. A strike-slip motion was considered as a DC component, and it is denoted by the following moment tensor:

$$\begin{pmatrix} -1 & 0 & 0 \\ 0 & 1 & 0 \\ 0 & 0 & 0 \end{pmatrix} \tag{3.2}$$

3. A non-DC component was represented by CLVD which is expressed by the following moment tensor:

$$\begin{pmatrix} 0.5 & 0 & 0 \\ 0 & 0.5 & 0 \\ 0 & 0 & -1 \end{pmatrix} \tag{3.3}$$

4. Finally, a combination of explosion, strike-slip, and CLVD moment tensors were used to represent a complex source mechanism:

$$\begin{pmatrix} 1 & 0 & 0 \\ 0 & 1 & 0 \\ 0 & 0 & 1 \end{pmatrix} + \begin{pmatrix} -1 & 0 & 0 \\ 0 & 1 & 0 \\ 0 & 0 & 0 \end{pmatrix} + \begin{pmatrix} 0.5 & 0 & 0 \\ 0 & 0.5 & 0 \\ 0 & 0 & -1 \end{pmatrix} = \begin{pmatrix} 0.5 & 0 & 0 \\ 0 & 2.5 & 0 \\ 0 & 0 & 0 \end{pmatrix} \quad (3.4)$$

These four kinds of focal mechanisms were simulated at the same location in order to study the sensitivity of the characteristic function generator with respect to different source models. The synthetic seismograms that resulted from the simulation using four kinds of source mechanisms are shown in Figure 3.2. From the frequency spectra represented in Figure 3.3, their significant frequencies were observed between 0.3 - 4 Hz.

3.2 P- and S- characteristic functions

As mentioned in the previous chapter (see Section 2.2), diffraction stacking was applied to the characteristic function rather than the recorded seismogram. Transforming the recorded seismogram into P- and S characteristic functions was conducted by making use of the three-component seismogram.

Polarization attributes, such as rectilinearity, apparent vertical angle, and eigenvalues, were estimated from the three-component seismogram. Since rectilinearity is equal to 1 for pure body waves (Jurkevics, 1988), this could be useful to distinguish between seismic events or noise signals. It could be used to enhance signals and reduce noise as well. Furthermore, the apparent vertical angle, δ, could be used to separate the P and S wavefields of a local earthquake since $\cos\delta \approx 1$ for P waves; while for S waves, it is $\cos\delta \approx 0$ (i.e., Ross & Ben-Zion, 2014). Figure 3.4 indicates the number of polarization attributes derived from one example of the three-component waveform resulted from ISO+DC+CLVD source mechanism, as shown in Figure 3.2(d). The curves clarify that the polarization attributes are capable of: (1) extracting the P- and S-onset from the synthetic example as it is indicated by λ_1^2 and $(r\cos\delta)^2$ functions, and (2) enhancing the body waves as implied from the rectilinearity (r) curve.

When performing the polarization analysis, only one parameter is required; i.e., the window size. A window size of 640 ms was used in this analysis. Estimation of the window size can take into consideration the dominant frequency of the waveform. In this

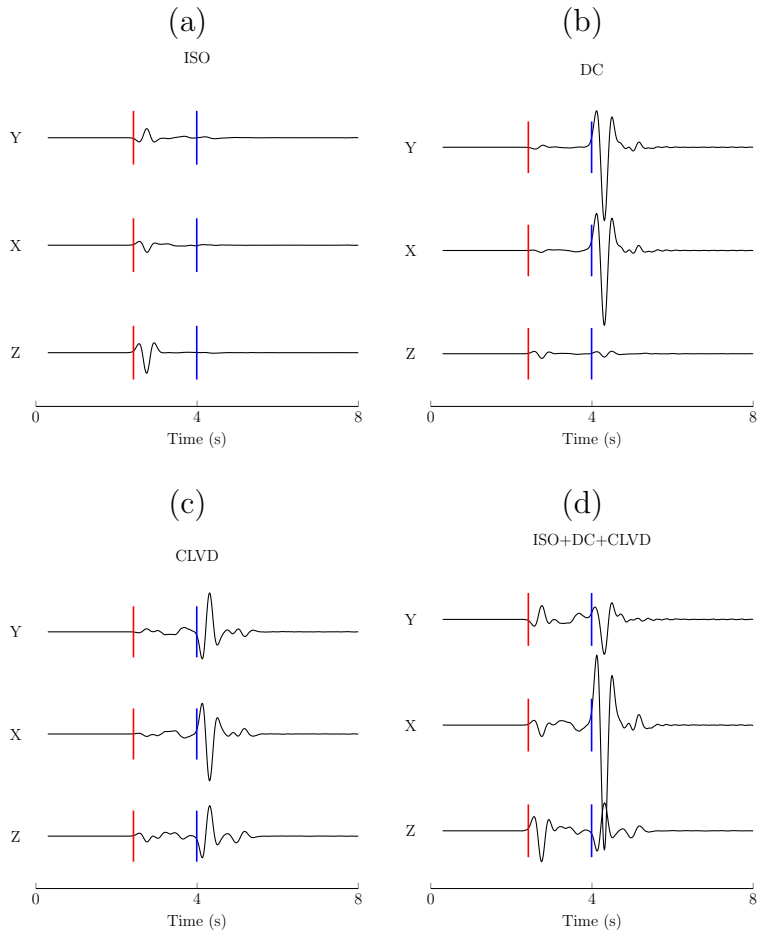

Figure 3.2: The X, Y, and Z components of the synthetic particle acceleration for different focal mechanisms. The onsets of P and S waves were computed using the Eikonal Equation solver as shown by the red and blue lines, respectively. These waveforms are recorded at Station 1.

example, the dominant frequency of the waveform is 2 Hz (See Figure 3.3). The period of the signal can then be roughly estimated to be 500 ms. The triangular smoothing procedure (Claerbout & Fomel, 2014) has also been applied to the polarization attributes with a window size of 10 samples (80ms).

The other attributes that need to be computed from the recorded seismogram are the mAIC function (Equation 2.29) for each component of the seismogram. The calculated mAIC function from the synthetic seismogram shown in 3.2(d) is presented in Figure 3.5. The computation of mAIC functions was conducted using a window size of 2.5s. This value does not need to reflect the dominant period of the signal, but it is confined by the delay time between the P- and S-onset. Since the value of mAIC is assigned to the

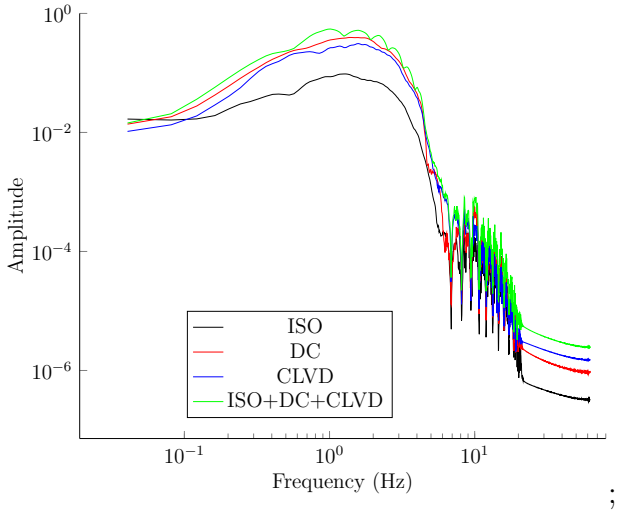

;

Figure 3.3: Frequency spectra of particle velocity of simulated seismograms using four different source models: isotropic, double-couple, CLVD, and a combination of these.

middle of the window, the 2.5s window size is still capable of detecting the S wave, which is separated by 1.25s from the onset of the P wave.

Characteristic functions such as STA/LTA (Grigoli et al., 2014) and kurtosis (Langet et al., 2014) are frequently used as input data in seismic event localization. However, they do not indicate either the P or S wave. This also applies to the mAIC function. The mAIC function might indicate the onset of body waves, but it cannot determine the type of body waves (P or S). Depending on the angle of azimuth, an mAIC function derived from a particular component of a seismogram could indicate only a P wave, an S wave, or even both P and S waves. For example, Figure 3.5 shows that mAIC(Z) and mAIC(Y) retrieve only the P wave; while mAIC(X) retrieves only the S wave. Thus, the interpretation of the wave type is carried out by making use of the polarization attributes (Figure 3.4).

The proposed equations 2.36 and 2.38 were used to determine the P- and S- characteristic functions from the mAIC functions and polarization attributes. The resulting functions, which were used as input functions for diffraction stacking, are shown in Figure 3.6. The P-wave characteristic function, CF^p, comprises the representative of the P wave since a characteristic function is located around the P-onset; whereas the S-wave characteristic function, CF^s, only includes the representative of the S wave. Both P and S characteristic functions no longer represent the real P and S waveforms, but rather their kinematic aspects (their onset times) (see Figure 3.2(d)).

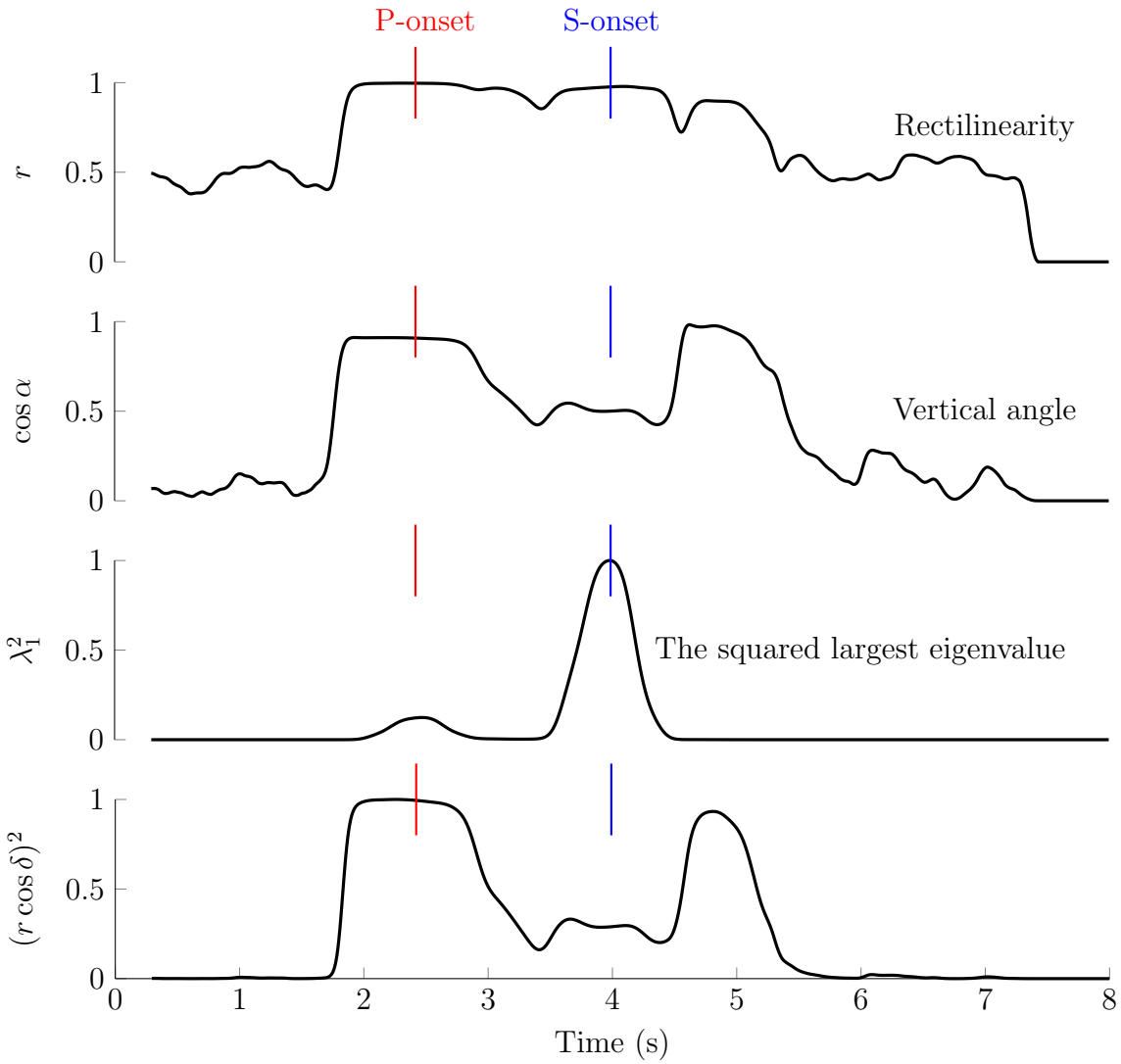

Figure 3.4: Some attributes derived from the original waveform correspond to a mixed-focal mechanism (ISO+DC+CLVD) (Figure 3.2[d]). These include: rectilinearity, apparent vertical angle, largest eigenvalue, the square of the product of rectilinearity and the apparent vertical angle. Red and blue lines correspond to the onset of P- and S-first arrivals. The λ_1^2 and $(r\cos\delta)^2$ curves could be used to extract the S and P waves, respectively.

3.3 Diffraction stacking localization

The Green Function Table (GFT) was prepared by computing the travel times of the P and S waves from all image points to receivers in the network. In this study, the travel time between a source-receiver pair was computed using the Eikonal Solver Code written by Podvin & Lecomte (1991). A voxel size of $250 \times 250 \times 250$ m^3 was used. Thus, the

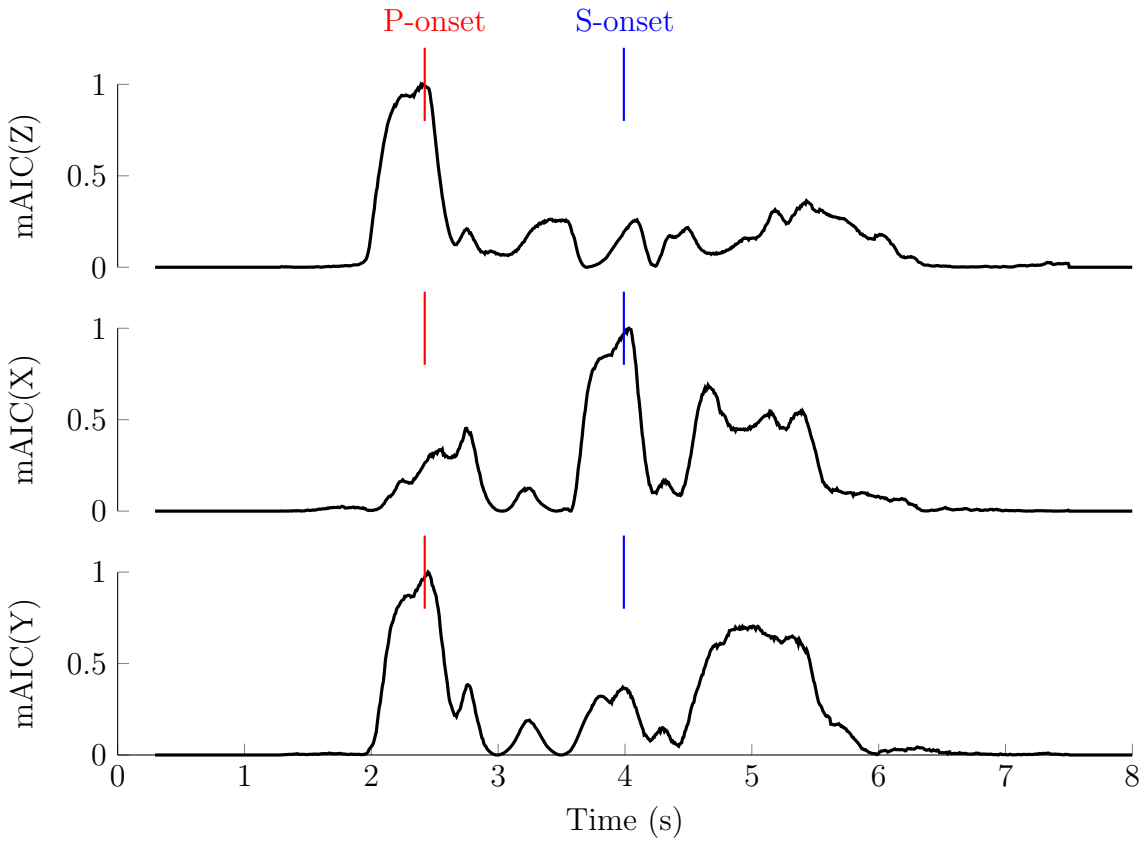

Figure 3.5: The normalized mAIC characteristic functions computed from the Z, X, and Y components of the synthetic seismograms (Figure 3.2(d)). The arrival of P and S direct waves is denoted by the red and blue lines. The onset of the P and S waves coincides with the peaks of several mAIC functions.

Eikonal Equation has to be computed numerically in a model consisting of $241 \times 261 \times 73$ (approximately 4.6×10^6) voxels. Each voxel could be the location of a seismic event, the travel time of the rays travelling from all voxels (possible location of seismic events) to receivers must be calculated. Calculation of Eikonal solver as many as 4.6×10^6 times and each simulation involved approximately 4.6×10^6 voxels will take a great deal of time. In order to circumvent the computation time, I employed the reciprocity principle. All voxels were considered as receivers and the true receivers installed on the surface act as hypothetical sources. As a result, the number of calculation of travel time was reduced from 4.6×10^6 to 42 (number of surface receivers). Moreover, the simulations were distributed to numerous cores by using a high performance Message Passing Library (Open-MPI). This was possible because each simulation is independent from any other. By using 42 cores, for instance, the GFT could be constructed by computing the Eikonal

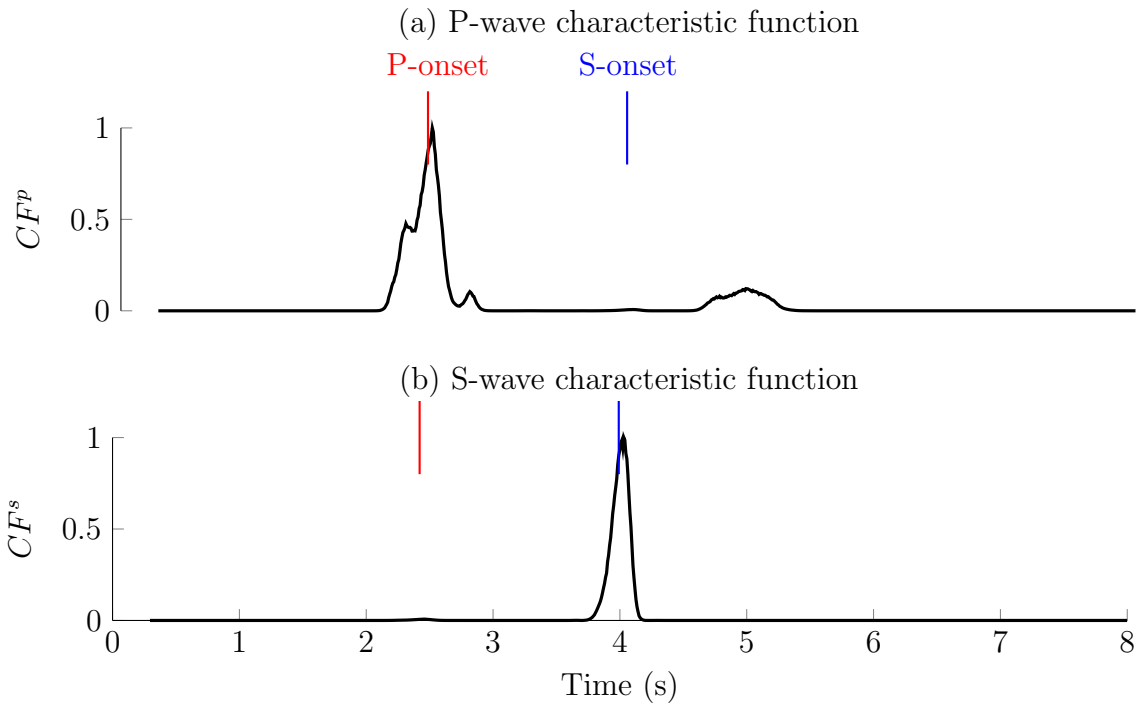

Figure 3.6: The P- and S-wave characteristic functions. The onset of the P- and S-waves is denoted by the red and blue lines.

Solver only one time. In this study, 42 computer cores were used to compute the GFT, significantly reduce the computation time. The computed GFT acts as a reference table which can be used to locate any seismic event. The GFT was computed using the same velocity model as that used for simulating the synthetic seismograms.

The proposed localization approach makes use of the P- and S-wave characteristic functions as its input function rather than the original seismogram. However, in this synthetic experiment, the localization using the original waveform (seismogram) was also conducted in order to compare the results with those obtained using the characteristic function.

3.3.1 Input function: the synthetic seismogram

Since the three ground motions of synthetic seismograms resulted from four focal mechanisms and were recorded by a three-component sensor, there were a total of 36 image functions. The analysis was divided into three categories based on the sensor components (X, Y and Z), due to the fact that the P wave was recorded by the Z component; whereas, the S wave was recorded by the X and Y components.

The GFT, which was computed using the P-wave speed, was used to locate seismic events from the Z component of the synthetic seismogram. The resulting 12 image functions are shown in Figure 3.7. The image function showing the stacking amplitude. These stacking amplitudes are associated with coherency of a seismic event. Thus, the seismic event location could be determined from the maximum coherency value. Consistency between the original location (red circle) and the maximum coherency was seen in most of the image functions except those resulting from the DC focal mechanism (Figure 3.7[d,e,f]). Thus, the location of a seismic event cannot be reconstructed if the focal mechanism is purely DC (strike-slip in this case). The location of a seismic event is surrounded by four lobes, rather than being represented by the maximum stacking amplitude.

It is interesting to note that the Z component of the seismograms pertained to the CLVD source (Figure 3.2[c]) produced an interpretable image function (Figure 3.7[g,h,i]) from which the reliable seismic event location could be estimated. These results emphasize that eventhough the S-wave signals present with higher amplitude that the P-wave, they do not contribute to the stacking amplitude. The use of an accurate velocity model could prevent a cross-talk between P- and S-wave signals.

The image functions resulting from the acceleration seismogram present more focused images (smaller uncertainty) compared to those resulting from the velocity and displacement seismograms. This was due to the fact that in the time domain, the frequency content of the acceleration waveform is higher than those of velocity and displacement. The better the time resolution of the input seismograms, the better the spatial resolution of the resulting image functions.

In conclusion, the vertical component of a seismogram can be used as input to reconstruct a seismic event location using the P-wave velocity model, except in the case of seismograms associated with the purely DC source model. In addition, the highest spatial resolution of event locations was achieved by acceleration seismograms. However, this benefit does not affect the final results since the location of a seismic event is derived from the maximum stacking amplitude (or image function).

The computed GFT using the S-wave velocity model was also used to locate a seismic event from the X and Y components. The resulting image functions are shown in Figure 3.8 and 3.9. The seismic event did not appear at image functions resulting from the explosion source model since there are no significant S-wave signals in both the X and Y

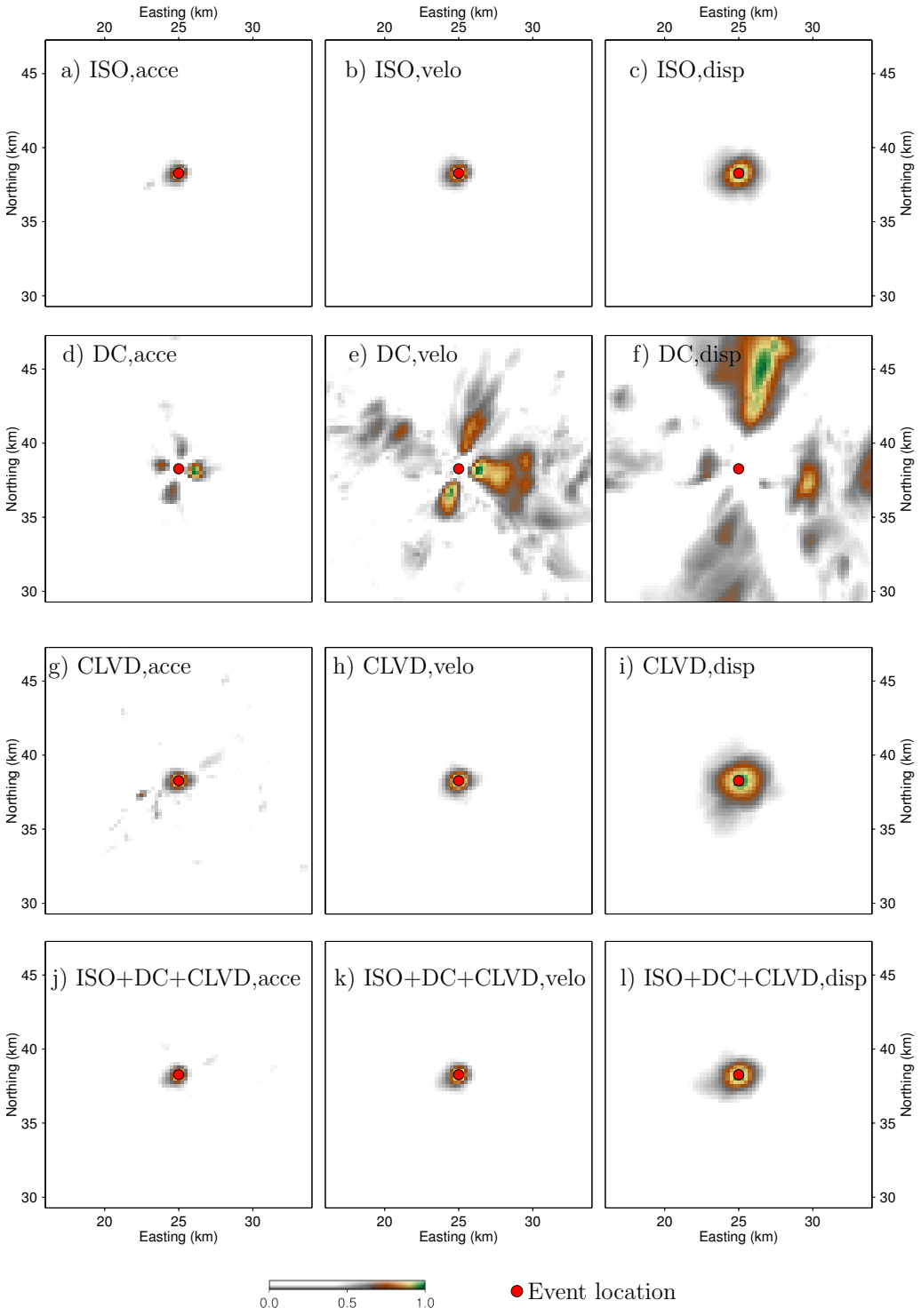

Figure 3.7: Twelve image functions were computed from the Z component seismograms. The seismograms were resulted from a combination of four focal mechanisms: (ISO, explosion, DC, CLVD and ISO+DC+CLVD) and were recorded in three ground motion forms: (acceleration, velocity and displacement). The amplitudes of image functions were normalized to 1. The red circles indicate the location of the original seismic event.

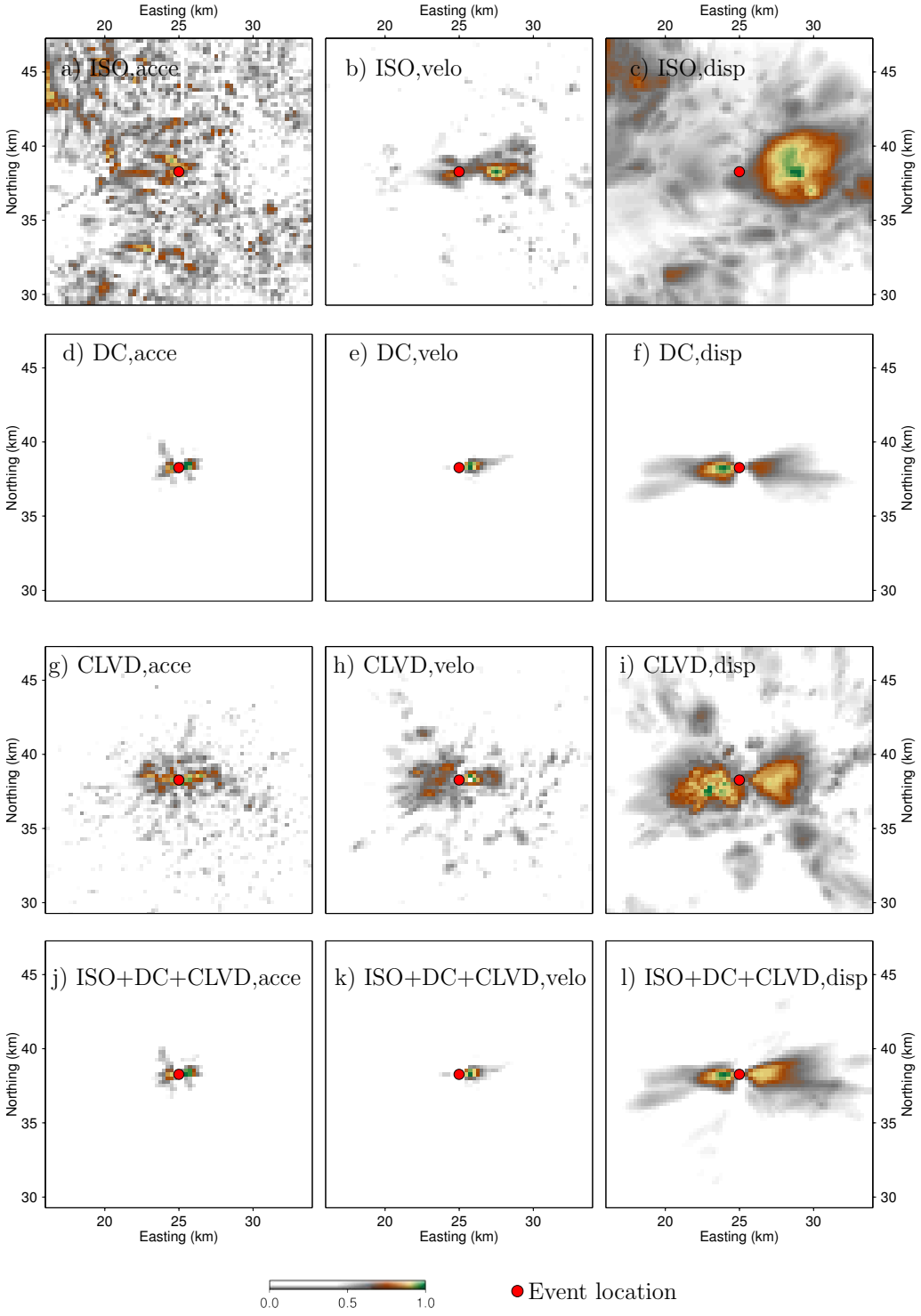

Figure 3.8: Twelve image functions were computed from the X component seismograms. The seismograms were resulted from a combination of four focal mechanisms: (ISO, explosion, DC, CLVD and ISO+DC+CLVD) and were recorded in three ground motion forms: (acceleration, velocity and displacement). The amplitudes of image functions were normalized to 1. The red circles indicate the location of the original seismic event.

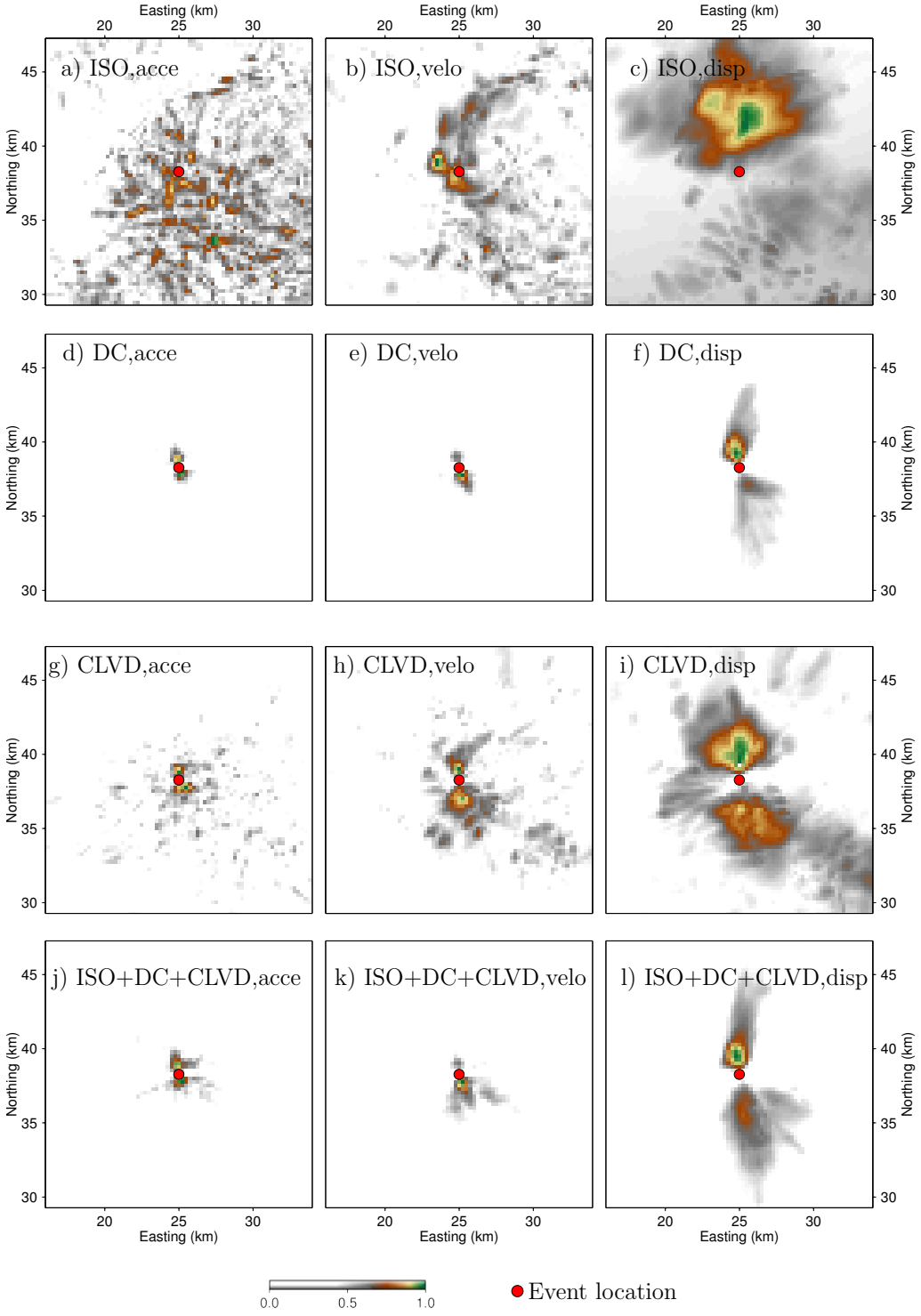

Figure 3.9: Twelve image functions were computed from the Y component seismograms. The seismograms were resulted from a combination of four focal mechanisms: (ISO, explosion, DC, CLVD and ISO+DC+CLVD) and were recorded in three ground motion forms: (acceleration, velocity and displacement). The amplitudes of image functions were normalized to 1. The red circles indicate the location of the original seismic event.

seismogram components. The examination of 24-presented image functions in both figures leads to a conclusion that the horizontal component of seismogram failed to reconstruct the seismic event location. This led to conclusive results that the horizontal components of a seismogram cannot be used by diffraction stacking to locate a seismic event.

3.3.2 Input seismogram: characteristic function

As previously shown (see 3.3.1), applying diffraction stacking directly to a seismogram is successful only for its vertical component. On the other hand, the horizontal component registers S waves; in which case, the utilization of this wave would improve the accuracy of a seismic event location. Hence, it would be advantageous if diffraction stacking is performed by considering the horizontal component as well. Unfortunately, this cannot be done if the polarity of a seismogram is not corrected. Several methods for correcting the polarity of a seismogram exist, including using the envelope of the rotated seismogram (Gharti et al., 2010) and a pair-wise cross-correlation method (Zhebel, 2013). In this study, a three-component seismogram was transformed into the P- and S-characteristic functions.

The characteristic function computation was applied to seismograms which are presented by acceleration, velocity, and the displacement of ground motion. The steps involved and the parameters used in calculating those functions were mentioned in Sec. 3.2. Figures 3.10 and 3.11 show the computed characteristic functions of the synthetic seismograms resulting from the ISO+DC+CLVD source model. In order to determine which ground motions produce the best characteristic function, an evaluation was conducted. This evaluation was performed by considering two aspects:

- The consistency between the theoretical arrival times and the peak of the characteristic function, and
- the temporal resolution of the characteristic function.

Based on these two aspects, the evaluation of the resulting characteristic functions showed that the best P-characteristic function resulted from the displacement ground motion; whereas, the best S-characteristic function resulted from the acceleration ground motion.

The results of applying diffraction stacking to the above P- and S- characteristic functions are shown in Figure 3.12. The image functions were computed from each char-

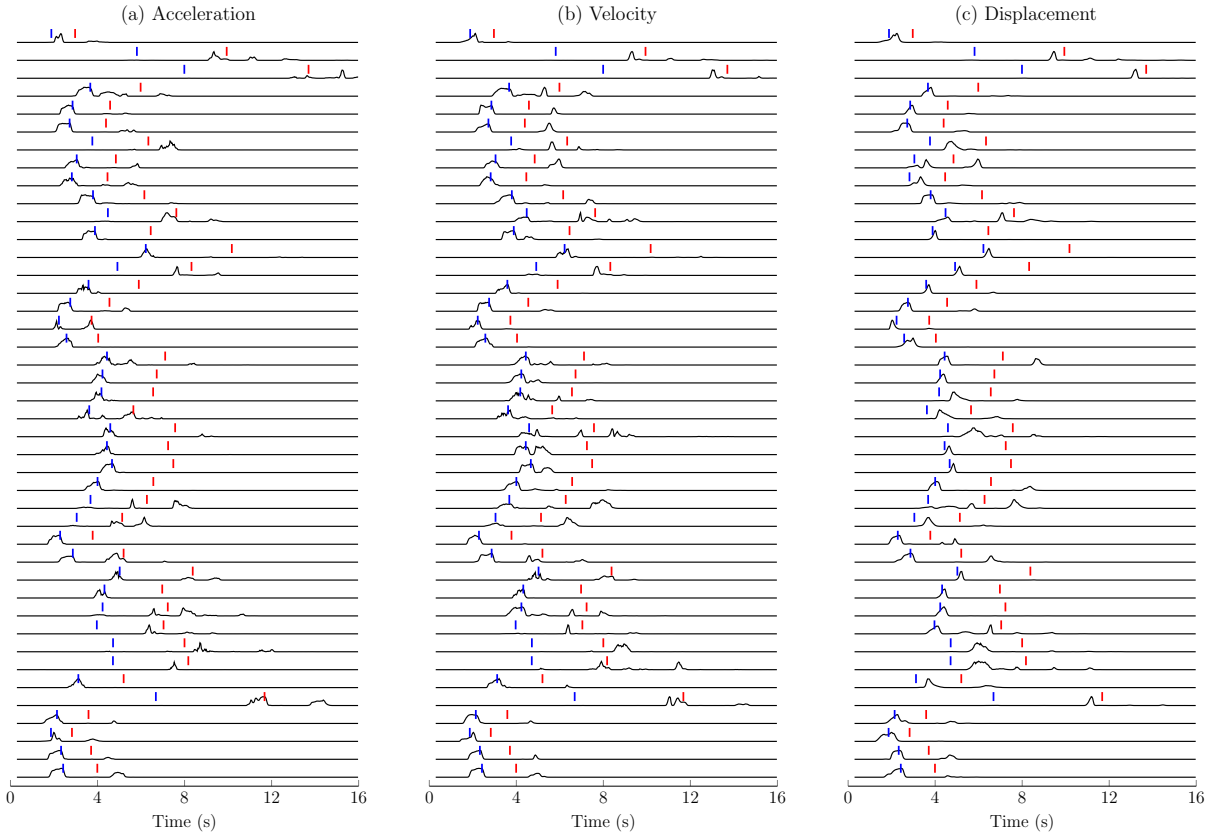

Figure 3.10: The P-characteristic function of the (a) acceleration, (b) velocity, and (c) displacement seismograms for the ISO+DC+CLVD source model. The blue and red lines denote the theoretical arrival times of P and S waves, computed by using the Eikonal Equation.

acteristic function by using the P or S travel-time function (GFT). The image functions resulting from the S-characteristic functions show more focussed images, compared to those resulting from the P-characteristic functions. This was caused by a poor resolution of the P-characteristic functions. In addition, the P characteristic functions did not show up at some stations; for example, at stations 5, 7, 8, 9, 10, etc., as shown in Figure 3.10(a). To obtain the final image functions, covariance analysis (see 2.3.3) was conducted using the P- and S- characteristic functions using a window of five samples in the X, Y, and Z directions. The computed highest eigenvalue, λ_1, is shown in Figure 3.12(g,h,i).

The results of applying the localization of 100 synthetic seismic events, as shown in Figure 3.1, are discussed. Figure 3.13 presents the located seismic events estimated from the velocity seismogram. The distance from the located event to the true location (or spatial error) is represented by gray lines. Larger errors are found in the southern

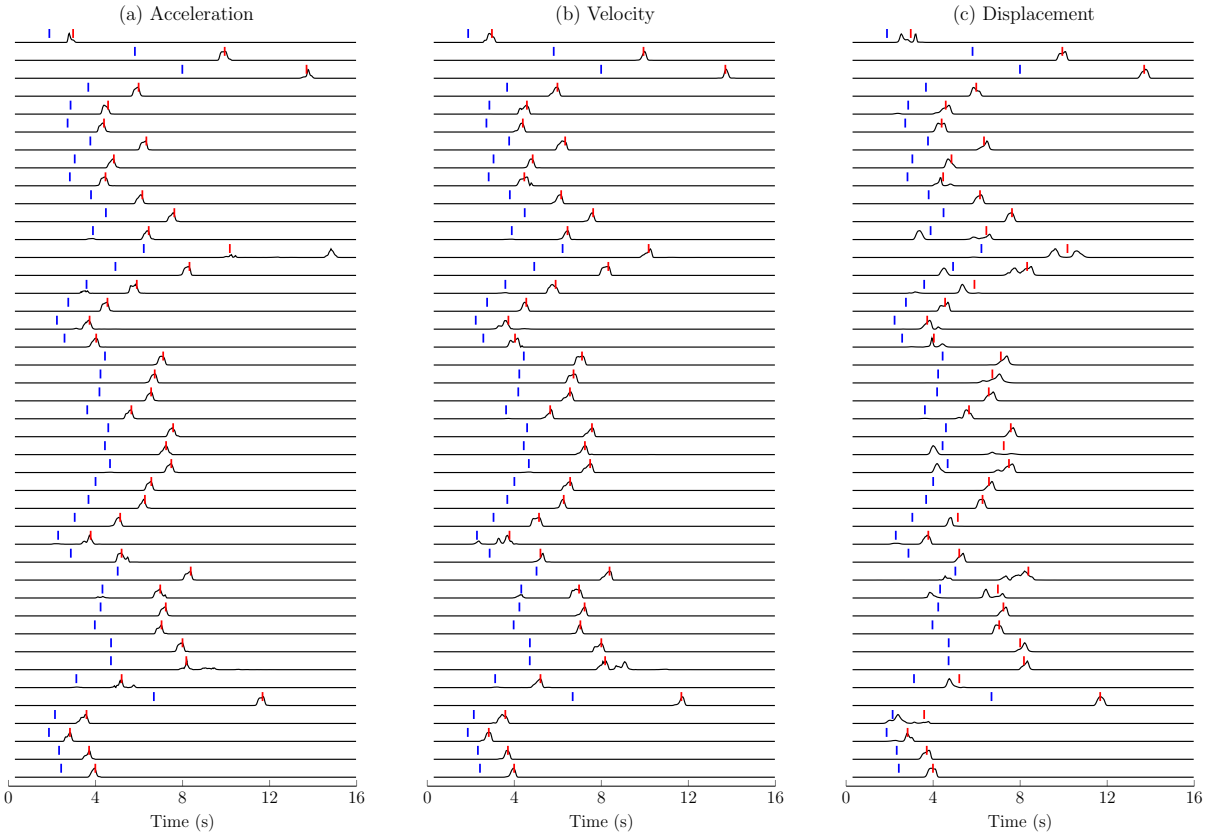

Figure 3.11: The S-characteristic function of the (a) acceleration, (b) velocity, and (c) displacement seismograms for the ISO+DC+CLVD source model. The blue and red lines denote the theoretical arrival times of P and S waves computed by using the Eikonal Equation.

part of the area; i.e., at $Y < 15$ km. This is due to poor coverage of the seismometer network. The located event in the southern part also shows larger uncertainties (black lines). In addition, the vertical (depth) uncertainty is higher than the horizontal one. The uncertainty of an event location is mostly defined by the seismic network (Bondár et al., 2004); particularly by either the primary or secondary azimuthal gap.

A location error, defined as the distance between the original event locations with those computed from diffraction stacking was chosen to quantify the accuracy of the resulting seismic event locations. Table 3.1 shows the statistics of the location error for three different input seismograms: displacement, velocity and acceleration. The seismic event location resulting from the acceleration seismogram computed using either the statistical or the maximum image function approaches appears to be more accurate compared to those resultant from the velocity and displacement seismograms. Their means of location

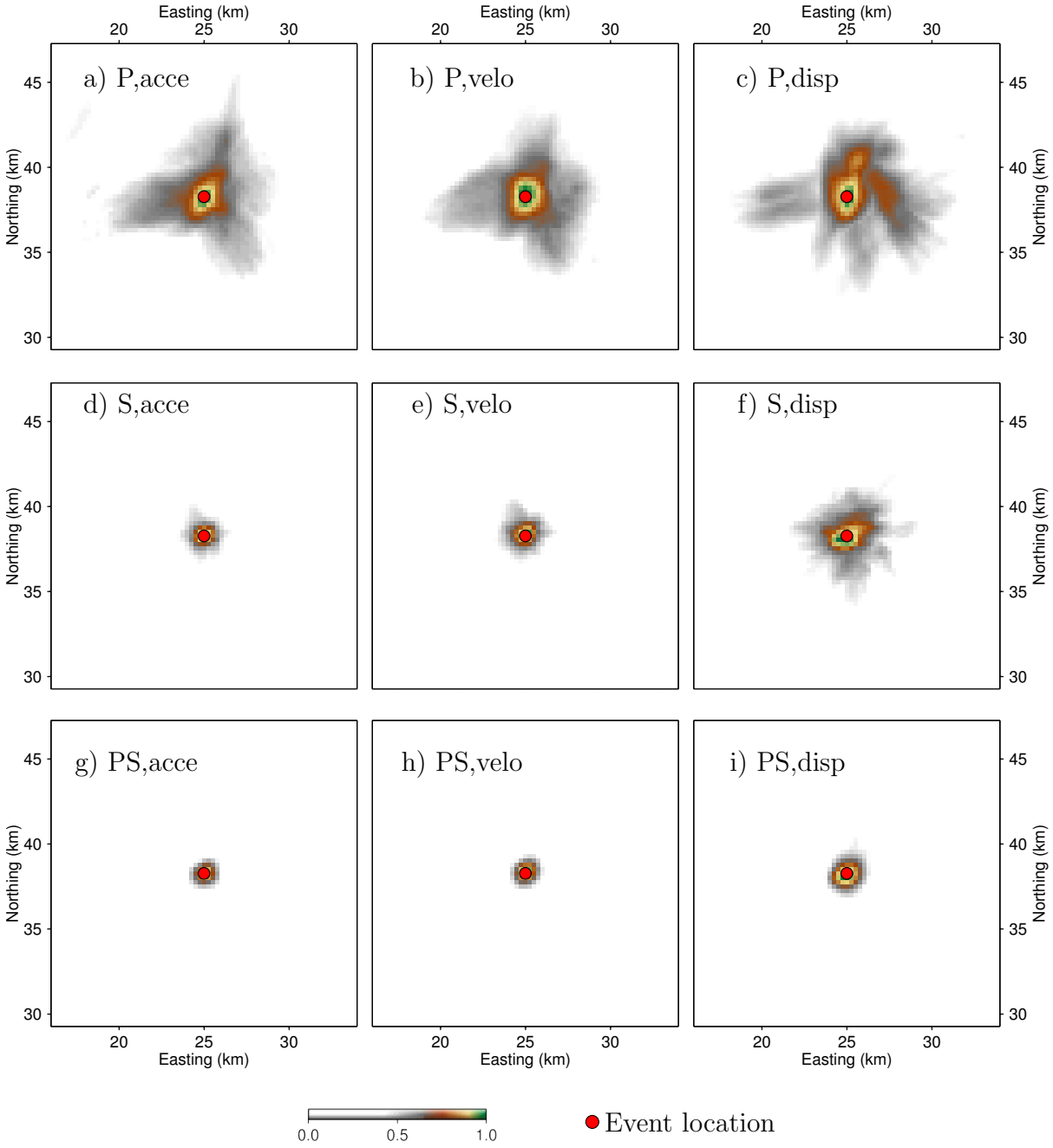

Figure 3.12: The image functions resulting from P- (a,b,c) and S- characteristic functions (d,e,f) for the ISO+DC+CLVD source model. The characteristic functions were computed using acceleration, velocity and displacement seismograms. The final images resulting from the covariance analysis of P- and S- image functions are also shown (g,h,i).

errors are smaller than the grid node spacing of 250 m.

By applying the steps explained in 2.3.2, the origin time of the seismic event (Figure 3.12) can also be extracted by the diffraction stacking methods. Figure 3.14 shows a comparison of the coherency (stacking amplitudes) curves $I(t)$ of those calculated from

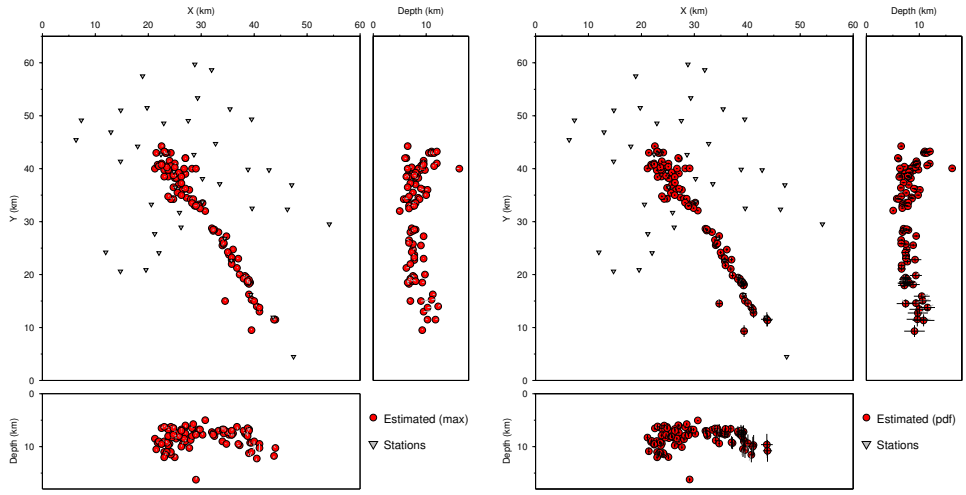

(a) Maximum (b) Statistical approach (pdf)

Figure 3.13: 100 located seismic events determined by (a) finding the maximum value and (b) applying the statistical approach (pdf) to the PS- image function. Gray lines delineate the true location.

Table 3.1: Statistical summaries of absolute location error computed from the **statistical** and **maximum** derived event locations from synthetic waveforms. Units are expressed in km.

	statistical (pdf)				maximum (max)			
	min	max	mean	std	min	max	mean	std
displacement	0.0518	2.1111	0.5012	0.4884	0.0594	2.1446	0.4185	0.3507
velocity	0.0800	1.1231	0.2926	0.1903	0.0761	0.7685	0.2891	0.1446
acceleration	0.0252	0.6068	0.1806	0.1137	0.0275	0.5050	0.2064	0.0918

the acceleration, velocity, and displacement seismograms. The best estimated origin time ($|\delta t_0| = 0.s$) was provided by the coherency curve resulting from the S-characteristic function of the velocity seismogram; whereas, the worst ($|\delta t_0| = 0.096s$) was estimated from the P-characteristic function of the velocity seismogram. The maximum misfit of $0.096s$ is equal to 12 time samples since the sampling rate of the seismograms was 8ms.

Figure 3.15 shows the performance of the diffraction stacking method in determining the origin time of a seismic event. The estimated origin times of 100 seismic events were compared to their exact value (same for all as of 0.496s), and their errors ($0.496 -$

(a) P-characteristic func.

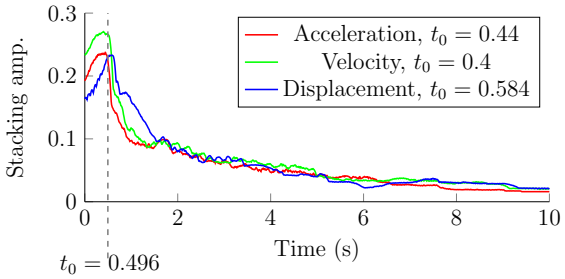

(b) S-characteristic func.

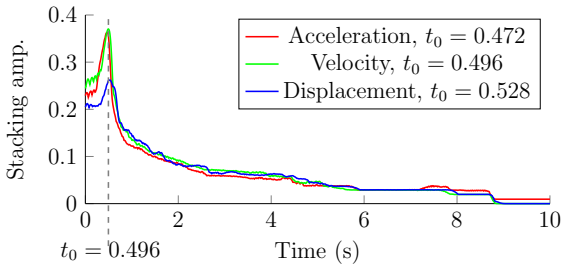

Figure 3.14: The estimated time of origin computed by the diffraction time. The exact value for the origin time is 0.496s. The sampling rate of seismograms was 8ms.

t_0') were computed. It is interesting to note that the mean and standard deviations of this error resulting from the P- and S- characteristic functions are different. The origin times resulting from the S-characteristic function show better results as indicated by a lower mean value. The value of 0.016s is equal to two discrete time samples as the sampling rate of the seismogram was 8ms. However, the error of the estimated time deriving from the P characteristic function is quite large. This error should be carefully considered since this may lead to an inaccurate depth of the located seismic event. The accuracy of the estimated origin time depends primarily on the accuracy of the characteristic function; accurate origin time can be achieved if the peak (the maximum amplitude) of a characteristic function coincides with the arrival time of P or S waves.

3.3.3 Random noise sensitivity

The signal-to-noise ratio would generally be low in seismograms recorded at the surface, particularly regarding local seismicity when the seismic events are not related to the interplate boundaries (megathrust). The advantage of using diffraction stacking methods is that this method is capable of dealing with noisy data (e.g., Gajewski & Tessmer, 2005). Hence, the synthetic seismograms were intentionally contaminated with random noise in order to determine the capability of diffraction methods in dealing with noisy data. The strength of the added noise was adapted to produce synthetic seismograms with a certain signal-to-noise ratio (SNR).

The addition of random noise to the synthetic seismogram was conducted using the Seismic Unix command `suaddnoise`. This command applies the following algorithm:

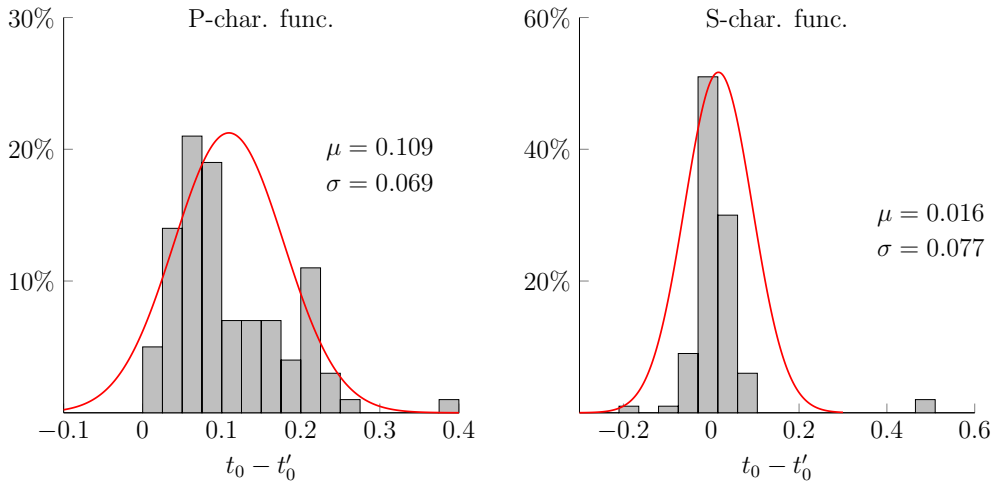

(a) (b)

Figure 3.15: Temporal errors of the estimated origin times resulting from (a) P and (b) S characteristic functions. The Gaussian curve was computed using the mean (μ) and standard deviation (σ) of the misfit. Note that the sampling rate is 0.008s.

1. Find the maximum absolute of seismogram amplitudes $[\psi(t)]$, $|\psi|_{max}$= max$\{|\psi(t)|\}$.

2. Generate a random number series (as many as the number of seismogram samples) with a mean and standard deviation of 0 and 1, respectively, $N(0, 1)$. The random numbers were generated using a code based on Marsaglia & Tsang (1984).

3. Compute noise power, $\overline{P}$, as denoted by the following equation:

$$P = \frac{\sum_{i=1}^{m} N^2(i)}{N}. \tag{3.5}$$

4. Calculate a scale, γ:

$$\gamma = \frac{|\psi|_{max}}{\text{SNR}\sqrt{2P}}, \tag{3.6}$$

   SNR is the required signal-to-noise ratio of noisy data.

5. Estimate the noisy seismogram:

$$\psi'(t) = \psi(t) + \gamma N(t) \tag{3.7}$$

SNR values of 1 was chosen to evaluate the robustness of the proposed method for computing the characteristic function. Synthetic seismograms (see Figure 3.2d) after contamination with additive noise to reach SNR values of 1 is shown in Figure 3.16.

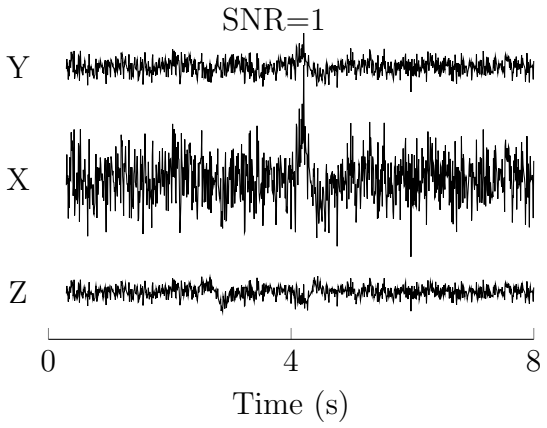

Figure 3.16: The contaminated synthetic seismograms with SNR values of 1. The waveform without noise is shown in Figure 3.2d. The window length is 0.8s.

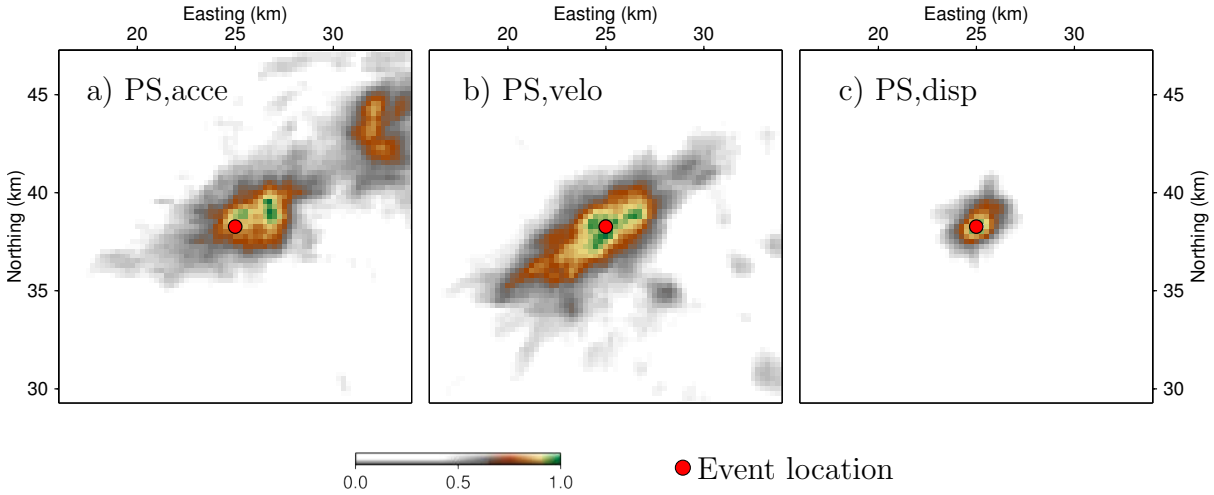

Figure 3.17: The comparison of image functions resulting from acceleration, velocity, and displacement seismograms with SNR equal to 1.

Figure 3.17 shows the image functions resulting from the synthetic seismogram with SNR equal to 1. Only the displacement seismogram could locate the seismic event (Figure 3.17[c]). These results show that the proposed characteristic function was able to act as a pre-processing approach which provides a reliable input function for diffraction stacking. However, when SNR=1, precautions need to be considered since only the displacement seismogram produced a reliable seismic event location. In addition, the resulting vertical location has a large measure of uncertainty.

Figure 3.18 shows the located seismic event where its input function was the characteristic function computed from displacement seismograms with severe noise contamination (SNR=1). The results suggest that diffraction stacking can be used to process data with

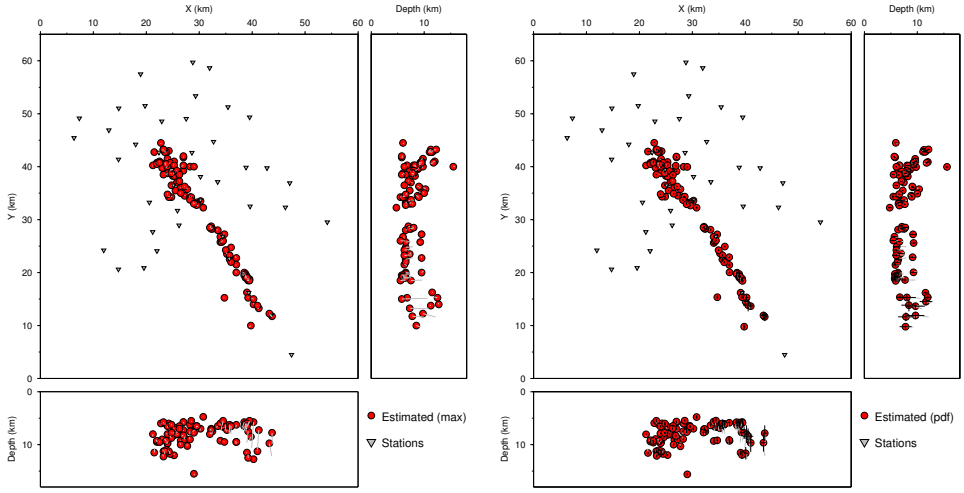

(a) Maximum (b) Statistical approach (pdf)

Figure 3.18: The located seismic events resulting from the characteristic function of displacement seismograms with SNR = 1. The point locations were estimated using (a) maximum value and (b) probability density function of the PS image function. Gray lines delineate the original locations. Hence, the longer this line, the larger the spatial error.

very weak signals. Another interesting outcome was found by comparing Figure 3.18 with 3.19: Seismic events derived from velocity seismograms show a larger amount of errors compared to those resulting from displacement seismograms.

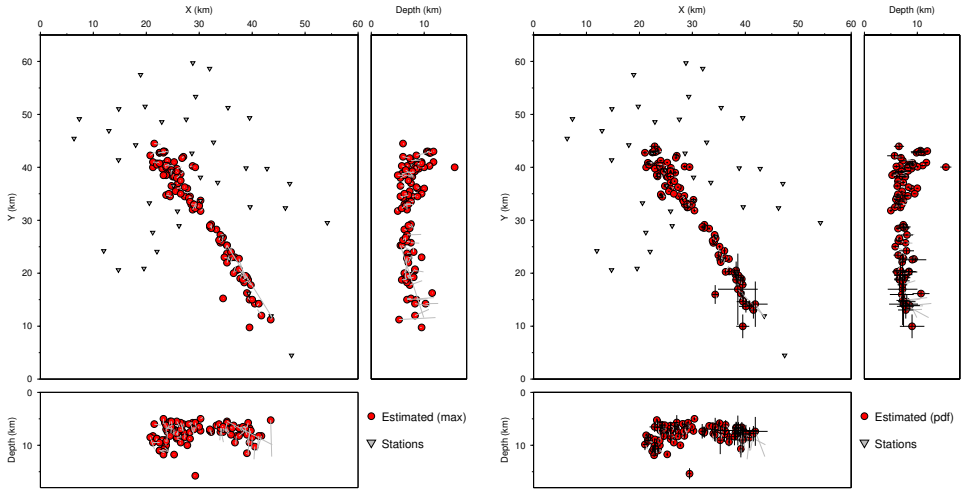

(a) Maximum (b) Statistical approach (pdf)

Figure 3.19: The located seismic events derived from velocity seismograms with SNR = 1. The point locations were estimated using (a) maximum value and (b) probability density function of the PS image function.

Table 3.2: Statistical summaries of absolute location error computed from the **statistical** and **maximum** derived event locations from the synthetic waveform with SNR=1. Units are expressed in km.

	statistical (pdf)				maximum (max)			
	min	max	mean	std	min	max	mean	std
displacement	0.0742	2.6125	0.5608	0.5571	0.0930	4.8751	0.5580	0.6904
velocity	0.0551	7.9302	1.0139	1.1437	0.1009	16.6752	1.1695	1.8708
acceleration	0.0372	27.9267	1.0708	2.7836	0.1208	28.3117	1.0513	2.8420

Table 3.2 shows a comparison of the histograms of location errors as derived from the analysis of displacement, velocity and acceleration seismograms. The synthetic exercises have shown that for very low data quality (e.g. SNR=1), the analysis of displacement seismograms delivered event locations with the smallest uncertainty. In addition, velocity seismograms led to better results compared to those resultant from the acceleration seismograms.

The statistical parameters presented in the Table 3.1 and 3.2 show that the statistical summaries for the analysis of displacement seismograms are almost similar for seismograms with low and high quality data. This indicates that the new method, if applied to displacement seismograms, provides stable results independent from the noise level. Meanwhile, the location error depends strongly on the noise level, if acceleration seismograms are analyzed.

Figure 3.20 shows the location errors for each seismic event. This presentation reveals that the largest location errors are associated with the unfavorable distribution of stations (a sparse seismic network) in the southern part of the seismic network. It is interesting to note that for less noisy seismograms, the deviation of the estimated seismic event location from the original location (black cirle) is in-line with the trend of the seismometer distribution. Figure 3.20 (a) indicates that in the northern area the largest errors are related with the limiting accuracy of the sparse grid (250 m node spacing in this exercise). The uncertainty caused by the velocity model is ruled out in this exercise since the diffraction stacking was based on the same velocity model as the forward modeling to create the synthetic seismograms.

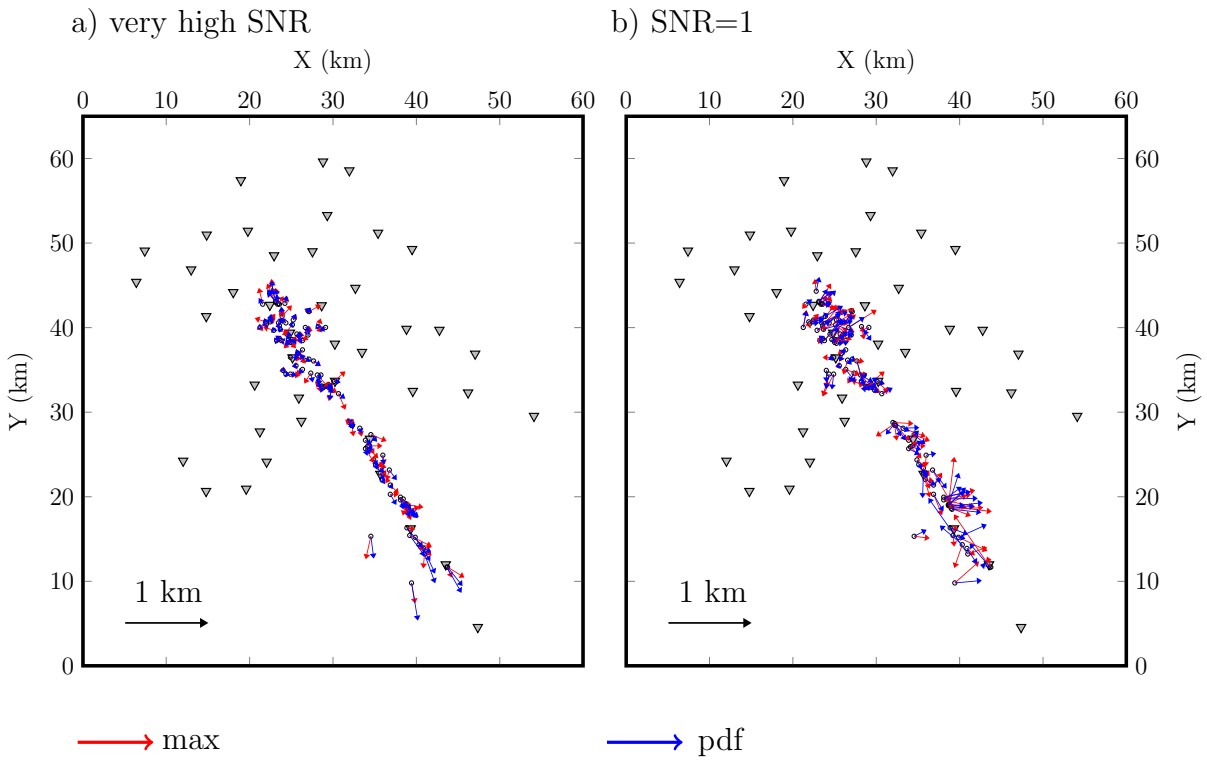

Figure 3.20: Map of location error associated with the maximum (max) and statistical (pdf) results computed from synthetic seismograms with (a) high quality and (b) very low quality of signals. The length of the arrows indicates the magnitude of error between those derived from diffraction stack and those from the original locations. The black circles represent the original locations of the seismic events.

Chapter 4

Application to local earthquake data from Sumatra, Indonesia

This chapter presents an application of the proposed localization workflow to seismic data records a number of seismic activities recorded in the Tarutung Region, North Sumatra, Indonesia (Figure 4.1). A series of pre-processing steps includes instrumental response removal, seismogram denoising and computing the characteristic function (CF) will be discussed. In a computation of the CF, different input seismograms which are represented in acceleration, velocity and displacement of ground motions will be considered. The analysis of a comparison of seismic events resulting from the unfilter and the filtered seismograms is also presented.

4.1 Tectonic and geological setting of the study area

The island of Sumatra is situated at the convergence boundary between the Indo-Australian and Sunda Sub-plates. The Indo-Australian Plate is moving northward against the Sunda Subplate at a rate between 59 mm/year at the southeastern tip of Sumatra (around latitude $-5°$) and 53 mm/year at latitude $5°$ (Prawirodirdjo & Bock, 2004; Briggs et al., 2006). The oceanic part of the Indo-Australian Plate is subducting beneath the Sunda Plate, but the subduction is oblique, unlike the frontal subduction occurring at the convergence at the south of Java Island (along the Java Trench). As a result of this oblique convergence, the resulting strains introduce two kinds of mechanisms: a dip-slip displacement that occurs along the so-called Sunda megathrust where the two plates meet,

and a strike-slip movement at the overriding plate. These mechanisms are also called slip-partitioning (Fitch, 1972). These two kinds of slip-partitions have been verified by numerous earthquakes that occurred at both the Sunda megathrust (for-arch) and along the dextral strike-slip of the Sumatran Fault (SF) (Figure 4.1). At the for-arch region, the earthquakes mainly showed thrust fault focal mechanisms. These earthquakes rupture plates along the Sunda megathrust with strikes parallel to the plate boundary. Meanwhile, strike-slip fault mechanisms occurred along the magmatic arc were striking in a NW direction. One example of a seismic event at the megathrust is the great Sumatra-Andaman earthquake of December 26, 2004 that ruptured the 1600 km-long plate boundary and 15 m fault slip near Banda Aceh (Lay et al., 2005). A large earthquake with a magnitude of 7.7 also occurred at the SF in 1892 (Reid, 1913).

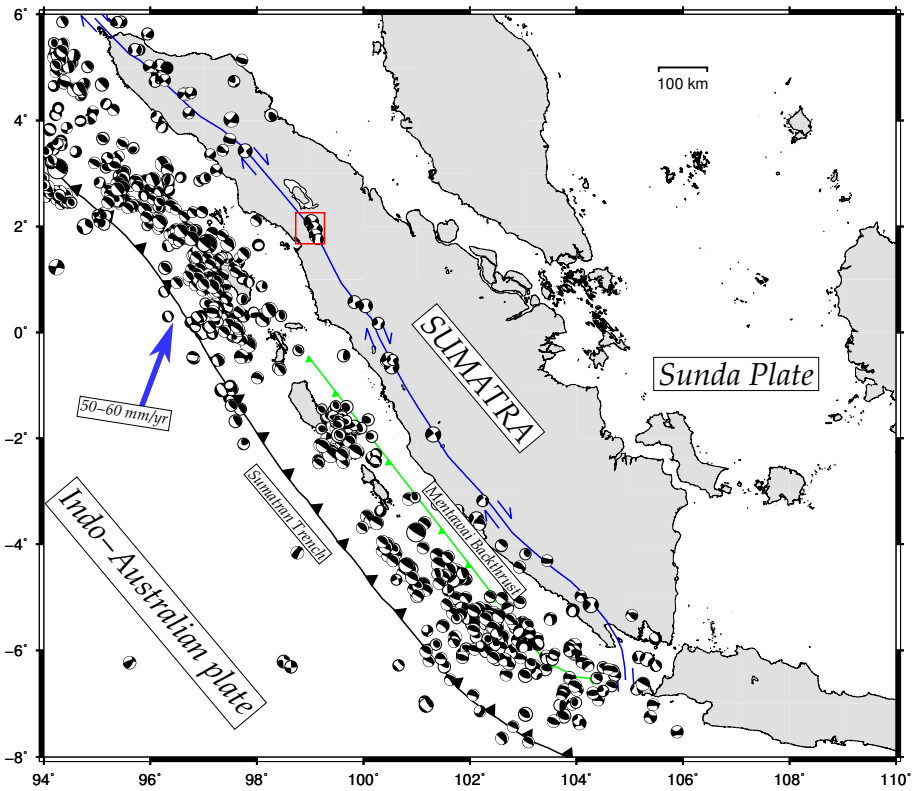

Figure 4.1: Regional tectonic map of the area surrounding the Tarutung and Sarulla Regions (red box). The focal mechanisms around the Sumatran Plate boundary with depths of less than 40 km are also presented (Global CMT catalogue between 1976-2016). The blue line indicates the Sumatran Fault (SF) and the green line denotes the Mentawai Fault. The blue arrow showing a horizontal velocity vector of the Indo-Australian plate movement.

The Indo-Australian Plate converges with the Sunda Sub-plate in different directions and at different rates, causing the SF to be segmented into 19 major segments (Sieh & Natawidjaja, 2000). Particularly in the northern part of Sumatra, the segmentation of the SF introduced offsets (step-overs) between segments and caused en-echelon faults, forming pull-apart basins in the late Neogene Period (Hickman et al., 2004). In central Sumatra, the SF is splitting into two trace faults in which the two parts are separated by a 35 km long divide (Weller et al., 2012). The Tarutung Basin and the Sarulla Graben are two of thirteen identified basins (Muraoka et al., 2010) in the area. The Tarutung and Sarulla Basins are being bounded by the Hutajulu Fault at the western side and the Tor Sibohi Fault at the eastern side (Bellier & Sébrier, 1994; Hickman et al., 2004). The latter continues to the south and becomes the eastern boundary of the Sarulla Graben (Hickman et al., 2004). These two faults meet at Silangkitan Village north of Sarulla Graben (Hickman et al., 2004).

Since the strike-slip SF trace can be derived from the Satellite image (Bellier & Sébrier, 1994), it has been found that a number of volcanic centers reside nearby the fault. Two volcanic centers are located at both ends of the Sarulla Basin: the Imun Volcano in the north and the andesitic Martimbang Volcano in the southwest. These volcanic features and geothermal manifestations seem to be related to the releasing stepover fault zones of the segmented SF. Although the volcanoes are not active at present (Nukman & Moeck, 2013; Ryberg et al., 2016), geothermal manifestations can be found in the area, such as large travertines localized along the eastern boundary of the Tarutung Basin 4.2, and hot springs whose temperatures increase from west to east (Nukman & Moeck, 2013).

Travertines and hot springs with high flux are located only along the southeastern boundary of the Tarutung Basin, at such locations as Sitompul (STP), Pansur Napitu (PN), Hutabarat (HT) and also in the southern part of Pianor nor (see Figure 4.2). These geothermal manifestations present at local extension due to clockwise block rotation (Nukman & Moeck, 2013). Travertines at locations HT, PN and Pianor nor are characterized by N-S striking extensional fractures; whereas at locations Ria and STP their fractures striking NW-SE parallel with the strike of SF. A speculated caldera-like formation was observed from the surface (Nukman & Moeck, 2013) and was interpreted as an ancient caldera as supported by low surface seismic velocity (Ryberg et al., 2016).

Nukman & Moeck (2013) reported several faults indicating local compression and

extension present at the Tarutung Basin. The reverse fault striking WNW-ESE was observed close to the springs Air Soda (AS). The normal fault striking NW-SE (AK) develops at releasing bend at the southern part. At Panabungan (PNB), the WNW-ESE normal faulting fault was found in which hot springs with a temperature of 49° C was found (see Figure 4.2).

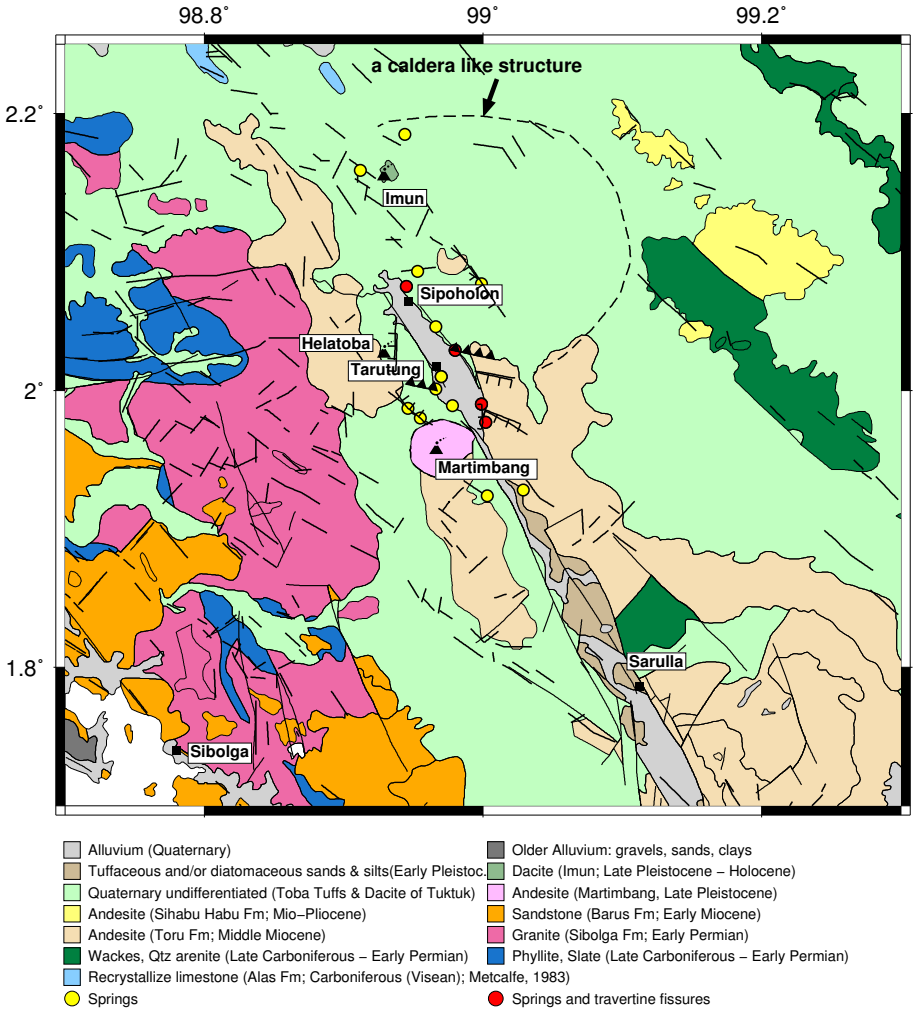

Figure 4.2: Geological map of the Tarutung and Sarulla Regions (after Apsden et al. (1982); Clarke et al. (1982); Aldiss et al. (1983); Nukman & Moeck (2013); Ryberg et al. (2016).

The Quaternary Toba Tuff Formation resulting from the explosion of the Toba Caldera 73 ka is widespread across the study area, while the Tarutung and Sarulla Basins are filled with quaternary alluvium. The andesitic lava of the Toru Formation (Middle Miocene) was exposed northwest of the Tarutung Basin and between Tarutung and Sarulla Basins in the southern part. There is a lack of uniformity between the Andesitic lava of the Toru Formation with andesite where the Martimbang Volcano is located. The age of the

Martimbang Volcano is late Pleistocene. Granites from the early Permian Age were found at the western boundary as part of the Sibolga Formation complex.

4.2 Data acquisition

Passive seismic monitoring at the Tarutung and Sarulla Regions (Muksin et al., 2013) were conducted between May 2011 and February 2012. The purpose of this experiment was to study the influence of fault structures on the geothermal setting inside the region. Forty-two temporal surface seismic stations were installed; forty of these stations were equipped with short-period Mark sensors (1 Hz), and the two remains were equipped with 3C PE-6/B4.5 Hertz sensors. Digital seismograms were registered using 40 PR6-24 Earth Data Logger (EDL) and two DSS Cube Data Loggers (Omnirecs) using temporal samplings of 100 Hz (equals to 10 milliseconds). Most of the seismometers were installed in the surroundings of the Tarutung depression (Figure 4.3), covering an area of 50 $\times$ 55 km^2, and were separated from each other by a distance of 5 km. Only five seismometers were installed along the SF traversing the Sarulla Basin.

The previous processing steps were conducted to map the seismic event distribution, and the following are summarized from Muksin et al. (2013, 2014):

- 1D velocity model derived from IASP91 was used to compute seismic event locations from P and S picks travel time. This resulted in 2,586 seismic events occurring around the Tarutung and Sarulla Basins.

- The number of seismic events were reduced to 809 after imposing restriction criteria. Only seismic events that occurred at depths of less than 40 km and those having an azimuthal gap of less than 180° were considered.

- These events were then refined by simultaneously deriving velocity models and seismic event locations using the SIMUL2000 Program (Thurber, 1983).

- The refined event locations were then relocated using the double-difference method (Waldhauser & Ellsworth, 2000) and finally resulted in 735 events (Muksin et al., 2014). One of the located seismic events is shown in Figure 4.3.

The diffraction stacking method was applied to an organized data set of Tarutung local seismicity. The application of diffraction stacking to a continuous seismogram data

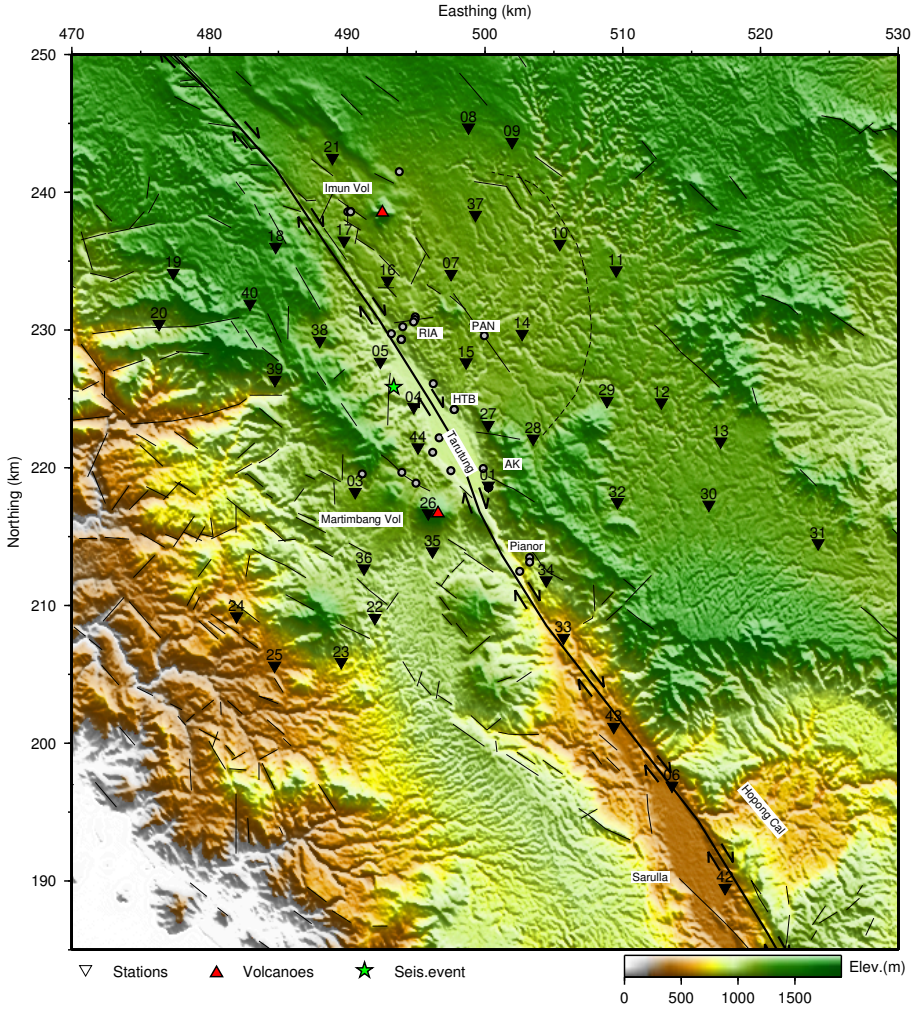

Figure 4.3: The distribution of 42 seismometers installed between May 2011 and February 2012 around the Tarutung and Sarulla Basins. The green star shows one example of a seismic event which occurred on May 19, 2011 at 12:35:44.39, in which the corresponding seismograms are shown in Figure 4.4. The lineaments were taken from (Nukman & Moeck, 2013).

stream is possible, but processing 10 months of recorded seismograms would require a large amount of time. Since the catalog particularly origin times of seismic events of this recorded seismograms has been obtained by the previous study (Muksin et al., 2013), diffraction stacking can be conducted on recorded seismograms that have been cut several seconds prior to the origin time of a particular seismic event, based on the information provided by the catalog. Therefore, diffraction stacking was applied to windowed seismograms with a length of 20s starting several seconds before the origin time of the seismic events. If the catalog has not yet been prepared, then the triggering event triggering, such as STA/LTA, can also be used to window the seismogram. By considering data

availability, 472 of 735 seismic events were chosen to demonstrate the performance of the proposed localization method. An example of cut seismograms recording an earthquake that occurred at a depth of 7 km is shown in Figure 4.4. Since at most locations the seismograms have high SNR qualities, in general a manual P-onset picking can be conducted on this example data.

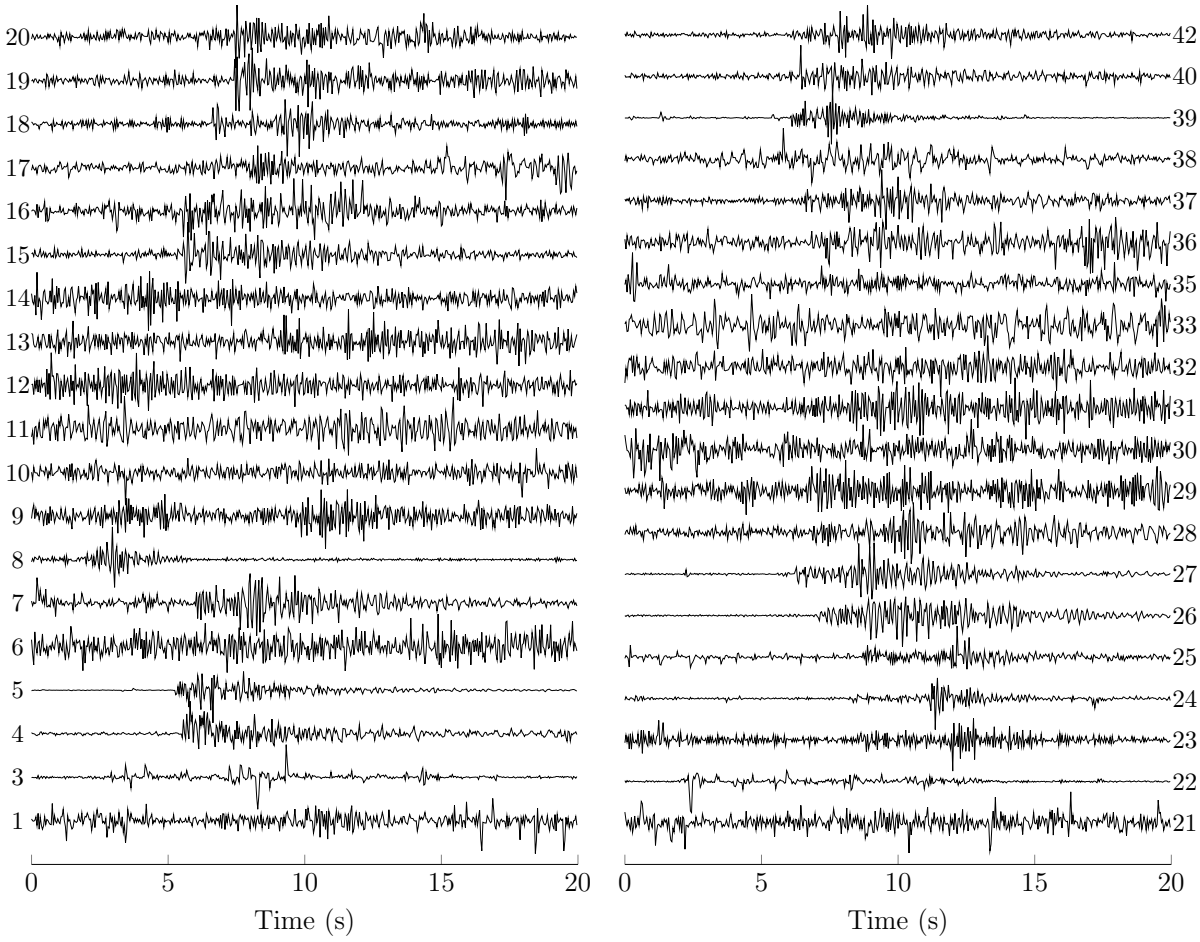

Figure 4.4: A local earthquake recorded on August 2, 2011 at 04:44:54.92 UTC. Time t=0 in these graphs corresponds to 04:44:51.42. The location of the epicenter is depicted by a green star in Fig. 4.3. Only the vertical components of the seismometers are shown and the amplitudes (in counts) were normalized according to the maximum value of each station. A zero-mean amplitude correction was applied. Each trace represents ground motions recorded at a particular seismometer.

Both P and S wave velocity models estimated by Muksin et al. (2013) derived from the simultaneous inversion were used as the velocity models for localizing events using the diffraction stacking method. The P and S velocity models were used to build the Green Function Table (GFT) associated with the P and S waves.

4.3 Diffraction stacking localization

Diffraction stacking localization was applied to the characteristic function (CF) of the seismograms rather than the actual recorded seismograms. However, some pre-processing steps were applied prior to transforming the raw seismograms into their respective CFs. These pre-processing steps consist of removing the instrument response and lowering random noises using Otsu thresholding. The filtered seismograms were then transformed into the characteristic function. Finally, a three-dimensional P and S image functions were constructed by stacking the amplitudes of the CFs along a diffraction curve (stacking operator) pertaining to the specific grid location. The last step was estimating an event location from the final image function which could be achieved through finding the maximum amplitude and computing the probability density function of the image function. The final image was resulted from the covariance analysis between the P and S image functions.

4.3.1 Instrument response removal

The amplitudes of the recorded seismograms represent the ground motions in digital counts, rather than in real physical units such as meters, m/s, or m/s^2. Therefore, restitution must be performed to retrieve the ground motions in the suitable units by correcting the instrumental responses of the observed seismograms. An example of an observed seismogram and its ground motion represented in displacement, velocity, and acceleration for a particular seismic event can be seen in Figure 4.5. The seismometers used in this study were velocity instrument seismographs, which explains the fact that the waveform of the ground velocity (Figure 4.5[b]) is similar to the recorded (raw) seismogram (Figure 4.5[a]). There were no significant changes after restitution, except that the units were converted from counts to m/s, and only minor changes occurred at some frequencies. By examining the maximum amplitude of the recorded waveform and its corresponding particle velocity, it can be concluded that one count is equivalent to approximately one nanometer per second.

Once the velocity of the ground motions was determined, the displacement and acceleration could also be computed. According to the synthetic experiments, it is obvious that the accuracy of the located events computed from velocity and displacement seismograms

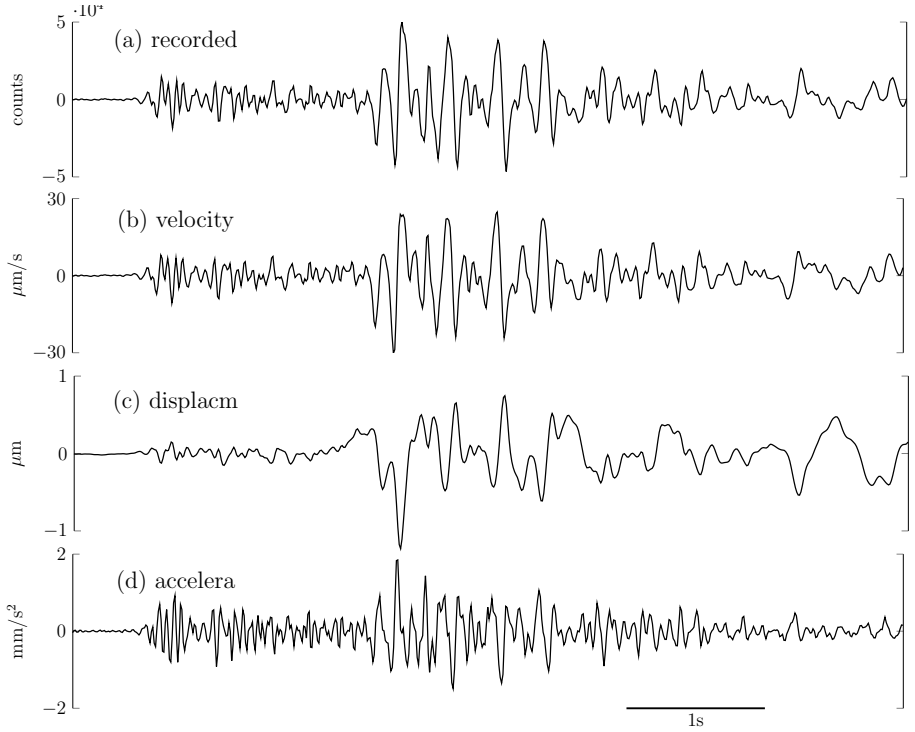

Figure 4.5: (a) The instrumental response (recorded seismogram) of an event, and its derived ground motion represented in (b) velocity, (c) displacement, and (d) acceleration.

were different (Figure 3.18 and 3.19). Therefore, it is of interest to compare the located seismic events at the study area derived from different seismogram representations, such as acceleration, velocity, and displacement.

4.3.2 Seismogram denoising

The seismometers used during the Tarutung passive seismic experiment were installed at the surface, which likely exposed them to abundant environmental noise originating from ambient natural noises (friction of wind over rugged topography, trees, flowing water/rivers) or anthropogenic vibration (traffic, daily activities). Since most of the seismometers used were installed near various public spots such as schools and offices (Muksin, 2014), anthropogenic vibration (or cultural noises) were more likely to have contaminated the seismogram recordings compared to ambient natural noise. Also, the amount of seismic noise could be greater during the daytime than nighttime, as shown by Figure 4.6.

Figure 4.6 shows a comparison of the average spectra of the seismogram recorded at daytime and nighttime. The lowest frequency is around 0.5 Hz as this value was

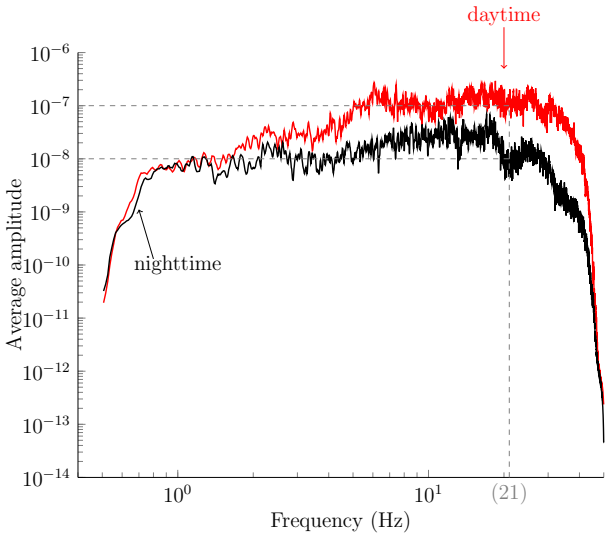

Figure 4.6: Average spectra of the waveforms recorded during daytime (6 am to 18 pm local time) and nighttime (18 pm to 6 am local time).

chosen as the lower cut-off filtering value during instrument response correction. It can be observed that the amplitude of the daytime spectrum is higher than that of the nighttime spectrum. The highest difference in amplitude between day and night was at a frequency of 5 Hz, which is about 40 dB ($20 \log (10^{-7}/10^{-9})$). This discrepancy seems persistent and continuous between 1-3 Hz as well as between 10-30 Hz.

An examination of the noise of the recorded seismograms was also conducted in a receiver gather-like. Seismograms registered at the same seismometer were collected into a group, and the noise levels recorded by the group were analyzed. The results provided insights on the noise levels of a given site where a particular seismometer was installed. By examining each receiver gather, one can compare the quality of waveforms based on the location of their installation. Figure 4.7 shows two seismograms differing in quality as they were installed at different sites. The location where station 39 was installed recorded higher SNR seismograms compared to those recorded at station 13, as the alignment of the P-waves is clearer at station gather 39. This is consistent with the fact that station 39 was placed in a relatively remote and quiet area while station 13 was located near a large village with a big population. In response to these results, seismogram denoising might be performed for seismograms recorded from stations with a high probability of noise, such as receiver gather 13, and might not be performed for seismograms from less noise-prone locations such as receiver gather 39.

The average spectra of the seismograms recorded at a location with less noise such as

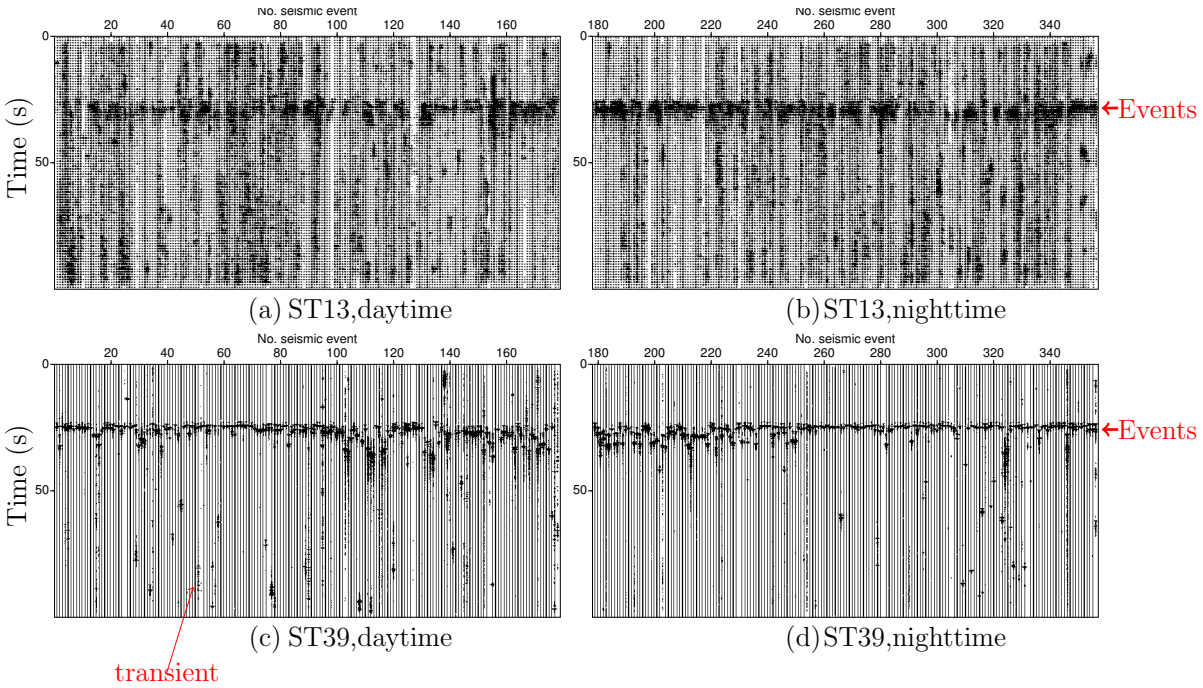

Figure 4.7: Seismograms recorded from receiver gather 13 (first row) and 39 (second row) at daytime (first column) and nighttime (second column). Only the vertical component seismograms are shown. Each seismic trace is a 100 second-long seismogram containing one seismic event. All the seismograms were aligned according to their origin time computed by the classical event localization (Muksin et al., 2013).

station 39 were similar during the daytime and nighttime (see Figure 4.8) at all frequencies except between 16-40 Hz. The magnitude spectra for frequencies between 16-40 Hz were higher in daytime than at nighttime, although the differences are quite low. Additional high frequency component noise recorded in daytime at station 39 was due to transient high frequency noises. Different results can be seen at station 13 which was installed near a large village. The average amplitude of the seismograms recorded at this station was higher in daytime compared to nighttime for all frequencies. This is a strong indication that anthropogenic random noise exists in seismograms recorded at some stations, including station 13. The anthropogenic noise at nighttime was, as expected, lower than in daytime. Therefore, denoising might be performed only on seismograms recorded in daytime.

For large magnitude earthquakes, background noises could be negligible. However, since we are interested in local earthquakes which usually occur with low magnitude, our seismograms suffer from environmental seismic noises. Hence, removing the background

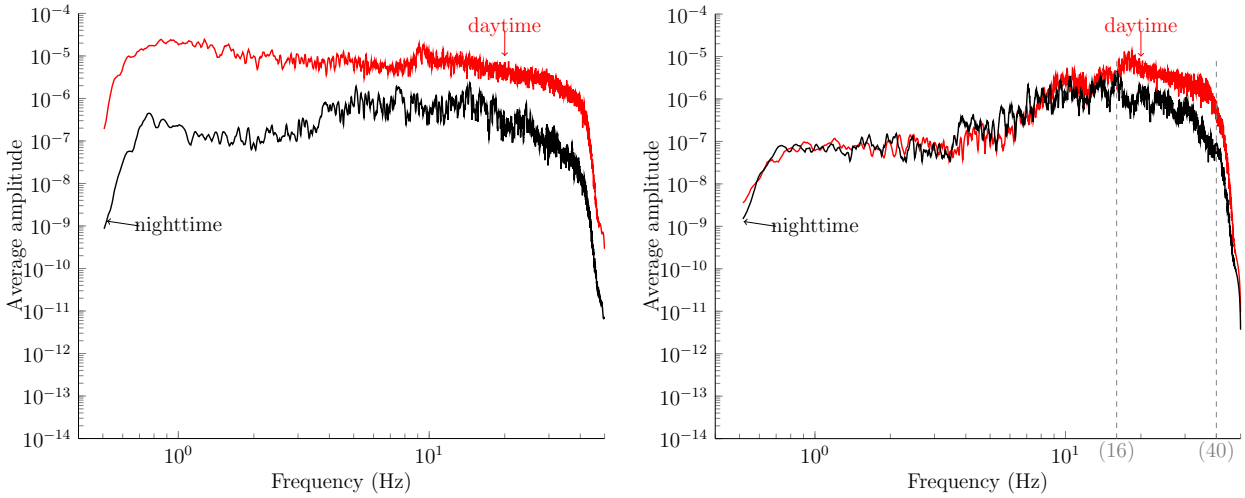

(a) Station gather 13

(b) Station gather 39

Figure 4.8: The average spectra of the seismograms recorded during daytime and nighttime for station gather (a) 13 and (b) 39.

noise before any further processing is desirable. Otsu thresholding method was used to decrease the amplitude of seismic noises.

Figure 4.9 compares the results of the seismogram denoising (filtering) using the bandpass and Otsu thresholding method shown as a time domain waveform and a time-frequency representation. The bandpass filtering method was very effective in removing very low frequency noises that could not be filtered using Otsu thresholding (Figure 4.9 [b,c] and Figure 4.10). However, bandpass filtering could not reduce noises in the frequency range between 5-25 Hz since these frequencies overlap with important signals (i.e., P and S body waves). A combination of bandpass filtering and Otsu thresholding establishes an effective protocol to increase the SNR of the recorded seismogram shown in Figure 4.9 (a). The resulting seismogram shows a relatively flat frequency spectrum between 5-20 Hz (Figure 4.10).

4.3.3 Computing the characteristic function

The characteristic function (mAIC) of the recorded seismograms was computed from the Tarutung field data using a window length of 200 ms. The resulting characteristic function was then smoothed by applying triangular smoothing using a window size of 100 ms, resulting in the P- and S-wave characteristic functions, which were then used as input to construct image functions.

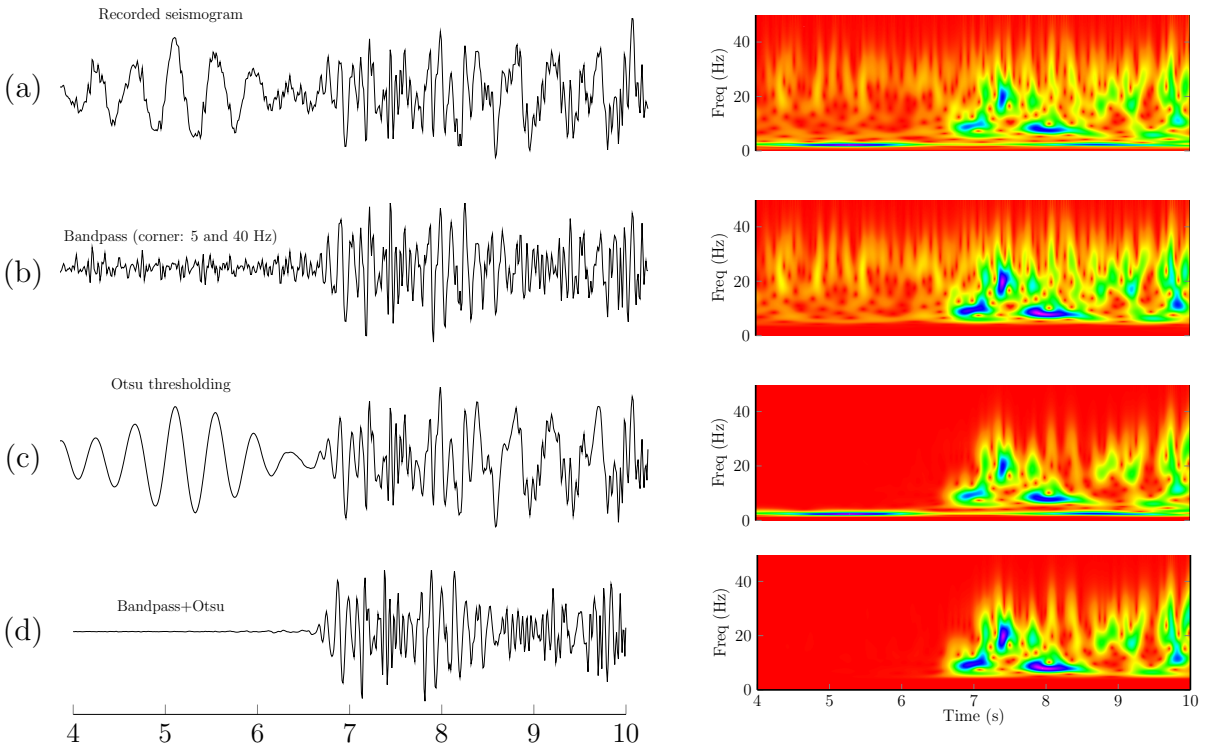

Figure 4.9: (a) Vertical component of a raw seismogram, (b) the seismogram filtered using a Butterworth bandpass filtering method with four poles and corner frequencies of 5 and 40 Hz, (c) the seismogram filtered using Otsu's thresholding method and (d) the filtered seismogram after a combination of bandpass filtering and Otsu thresholding.

4.3.4 Diffraction stacking

Firstly, event localization using the diffraction stacking method was conducted by discretizing the subsurface model. The study area has dimensions of 60×65×18 km in easting, northing, and depth direction, respectively. A grid size of 250 meters was used; and thus, the discretized model has dimensions of 241×261×73 grid points, or more than 4.6 million grids in total.

The following steps were used as a workflow to determine a seismic event location:

1. Prepare the GFT. This consists of travel time taken for a particular ray to travel through the assumed velocity model from each image point (grid point) to the seismometers. The method to compute the GFT was discussed in 3.3 since the synthetic example was created using the real velocity model of the Tarutung Region estimated by travel-time tomography (Muksin et al., 2013). The resulting GFT was then used to create a new catalog (particularly event locations) derived by the

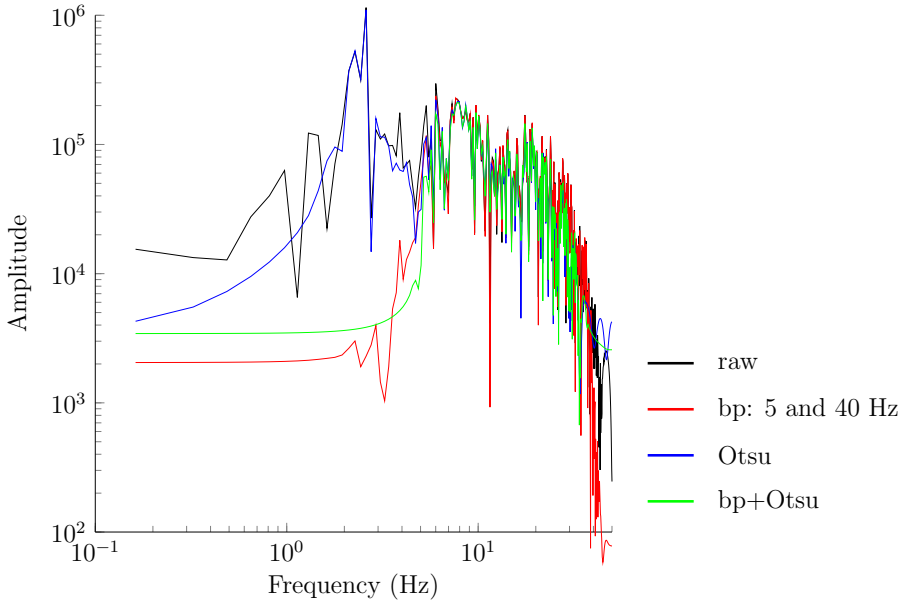

Figure 4.10: The frequency spectra of the raw seismogram: filtered using bandpass filtering, processed by Otsu's thresholding, and processed by two consecutive filterings: bandpass and Otsu thresholding filtering.

diffraction stacking method for local seismicities recorded during the 9-month-period of passive seismic measurements at the Tarutung Region.

2. Compose the P- and S-image functions by computing the stacking amplitude along a stacking operator constructed, based on the computed GFTs. The imaging condition used are explained in 2.3.2.

3. Combine the P- and S- image function by mean of covariance analysis.

4. Estimate the event location from the resulted image function using either the statistical or maximum image function approach.

As for an example to describe the resulting image function of a particular seismic event (as shown in Figure 4.4), Figure 4.11 shows a comparison of the resulting P-image function, S-image function, and PS-image function. The P- and S-image functions resulted from the P- and S-phase characteristic functions; whereas, the PS-image function was the result of covariance between the two. The covariance analysis was conducted by involving the two grid points surrounding the grid being evaluated. It can be seen that the image values surrounding the seismic event was located using a travel-time-based method (red point) are generally high. The S-image function showed better focusing than

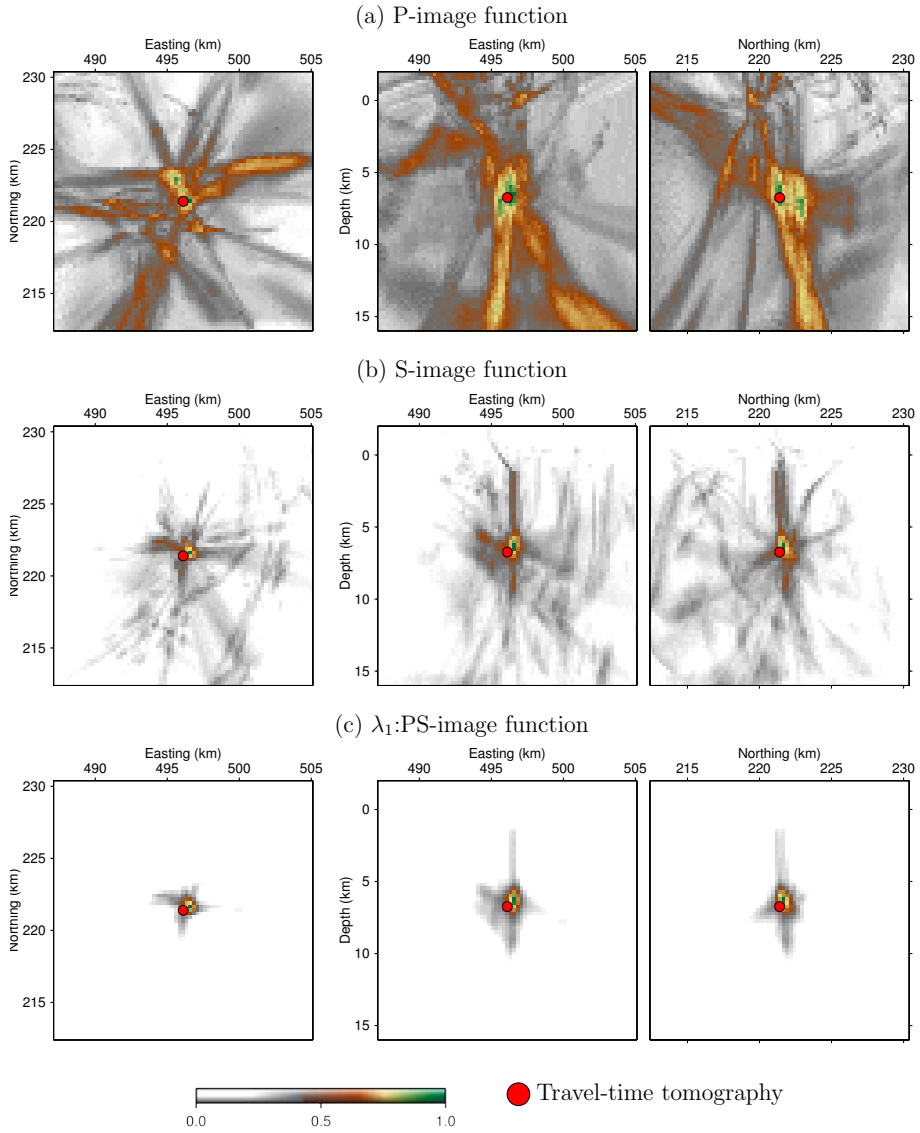

Figure 4.11: The image functions resulted from (a) the P- and (b) S- phase characteristic functions, as well as from (c) the covariance analysis between both P and S-phase of a particular seismic event. The three-dimensional image function was stacked (by choosing the maximum value instead of taking the average) along the $i-$axis to see a $jk-$ plan/section, where $i, j, k = x, y, z$. The images focused on a smaller area than the overall study area in order to easily examine these in greater detail.

the P- image function since the high image-values are localized into a smaller area. By applying covariance analysis between the P- and S- image functions, the focusing area was improved. The same processing steps were applied to data set consists of 472 seismic events.

Transforming an mAIC characteristic function into a high quality image function

through the diffraction stacking method is not enough. "Collapsing" the multidimensional image function into a point which represents the seismic event location is the next critical step after conducting diffraction stacking. Localization was performed on the 472 resulting image functions in order to retrieve the coordinates of a seismic event. Two methods were used to achieve this: a statistical method, in which the image function is transformed into a probability density function; and a method that involves finding the maximum image value (see 2.3.4). In the statistical approach, the resulting 472 image functions were converted into probability density functions, and location uncertainties (σ_x, σ_y and σ_z) were computed. For comparison, seismic events were also located using the maximum value approach. A comparison of the located seismic events derived from the same image function but using the statistical and the maximum value approaches is shown in Figure 4.12.

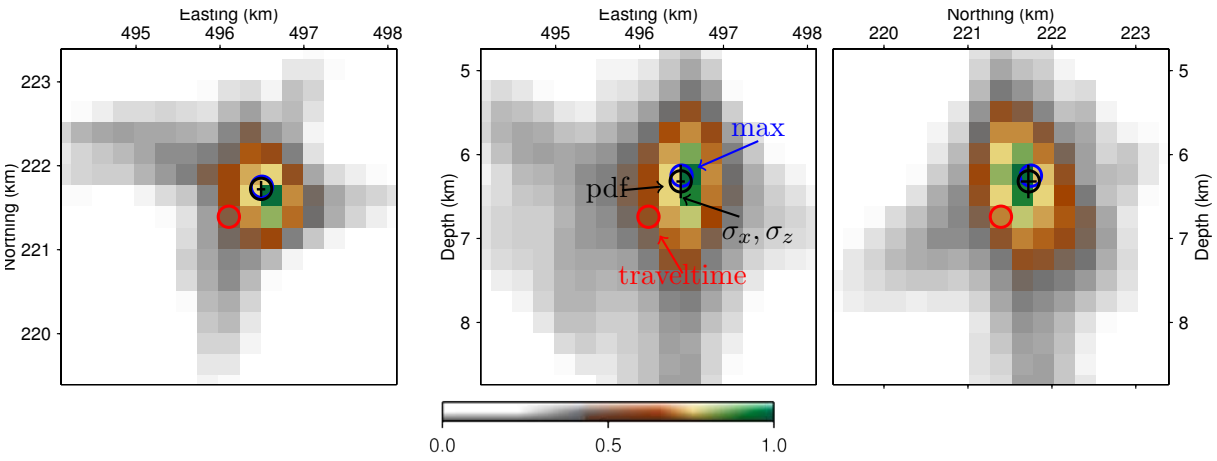

Figure 4.12: The estimated seismic event locations of the PS-image function (Figure 4.11) using the statistical approach (black) and the maximum value approach (blue). These estimated locations were compared with those computed using the travel-time tomography method (red). The uncertainties (one σ) are also shown.

The spatial uncertainty of the event localization was the only criterion to decide reliability of the results. Another parameter, such as the stacking amplitude, could also be considered for the same purpose. However, determining an appropriate amplitude threshold would be more difficult than determining an uncertainty threshold. A large uncertainty could be resultant from several sources, such as an inaccurate velocity model, noise on the recording seismograms, or a limited coverage of seismometer network. An example of an image function with large uncertainties ($\sigma_x = 0.95, \sigma_y = 2.49, \sigma_z = 1.489$;

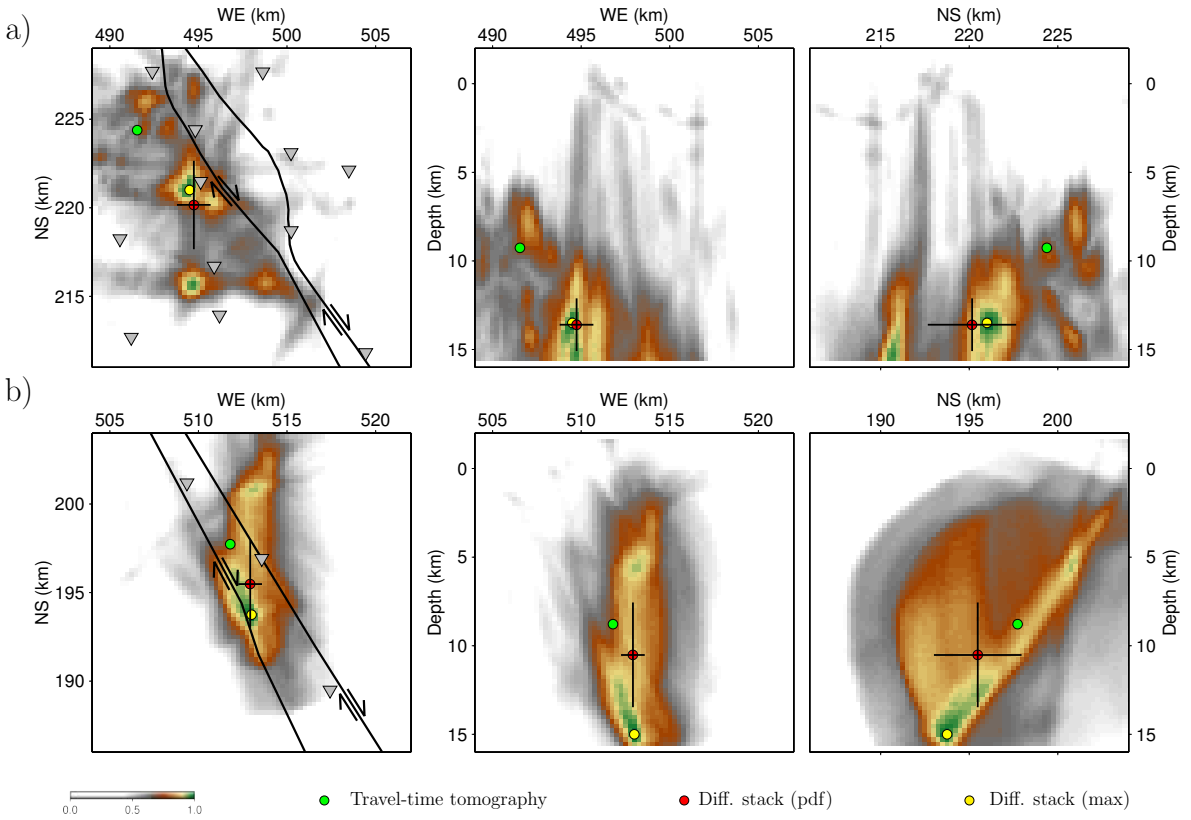

Figure 4.13: The plane view and cross-section image function of two seismic events located at (a) north and (b) south. Each image is resultant from the stacking of amplitudes along the corresponding particular axis; i.e., the plane view is generated by stacking the amplitudes along z-axis.

units are in km) is shown in Figure 4.13(a). This large uncertainty is suspected to be caused by a multi-peak image function. This image function is indicated by at least four clusters of coalescing amplitudes in which the travel-time tomography location (the green dot) is near to one of them. A huge separation between the location resultant from the diffraction stacking method and that computed by the travel-time tomography method can also be seen. Since the velocity model is accurate around the location of this seismic event, and the coverage of the seismometer network is broad, this large uncertainty must have resulted from the noisy data. Another example of an image function with a high uncertainty is shown in Figure 4.13(b). The high amplitude of the image function extends to the north from the maximum value (yellow dot) might be related to the seismometer network, while the multi-peak image function is introduced by noisy seismograms. Examination shows that the uncertainty is a reliable parameter to evaluate the accuracy of seismic event locations.

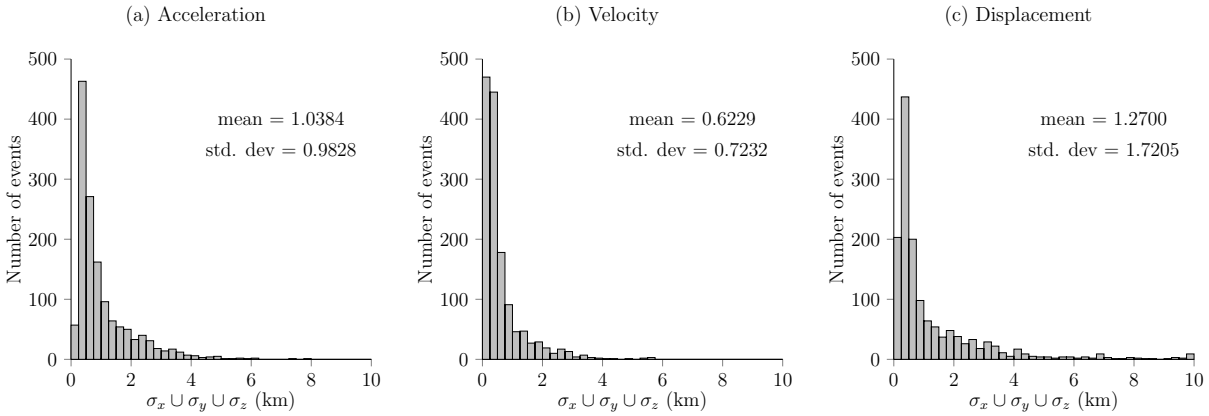

Figure 4.14: Histogram of uncertainties in the horizontal and vertical dimensions (σ_x, σ_y and σ_z) of the estimated event locations. The characteristic functions were computed from acceleration, velocity, and displacement seismograms.

The uncertainty of the located seismic event was used as a quantitative measure to examine the coalescence of the image of the seismic event location. An optimal focus is represented by a small uncertainty. On the other hand, a smeared or diffused image function would lead to high uncertainty. In a focused image function, the location of a seismic event determined by using different techniques (the maximum and statistical image function) would be close to each other, while in a diffused image function they would be dispersed.

In this work, the characteristic functions were computed from acceleration, velocity and displacement seismograms. To the resulted image functions, the location uncertainties were calculated. The results are shown in Figure 4.14. Then, an approriate type of seismogram which leads to the best results could be decided based on the location uncertainty. The use of the velocity seismogram is preferred because it resulted in the smallest mean and standard deviation (0.6229 and 0.7232 km). In the frequency range of local earthquakes, the waveform of the velocity seismogram is similar to the raw seismogram (before instrument correction); thus, localizing local earthquakes from raw seismograms might not degrade the quality of the resulting seismic location. Then, the diffraction stacking localization could be performed to the recorded seismograms without being preceded by the instrumental response correction.

Based on the results shown in Figure 4.14, it was decided that in order to achieve the best results, velocity seismogram could be used. Here, I introduce another parameter that can be used to evaluate the resulted image function. Horizontal location uncertainties

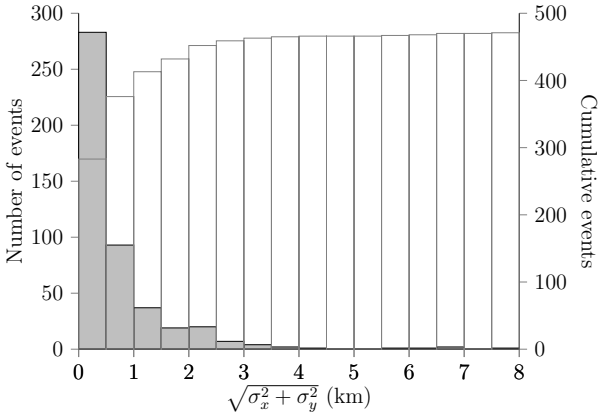

Figure 4.15: Histogram of total horizontal uncertainties of 472 seismic events.

were used to compute a total horizontal uncertainty $\sqrt{\sigma_x^2+\sigma_y^2}$. A result of calculating the total horizontal uncertainty to the 472 image functions is shown in Figure 4.15. From this histogram, it is seen that there are more than 275 seismic events (58%) with a total horizontal uncertainty of less than 0.5 km (or 2 grid nodes). Out of 472 seismic events, 377 (79.8%) have a total horizontal uncertainty of less than 1 km.

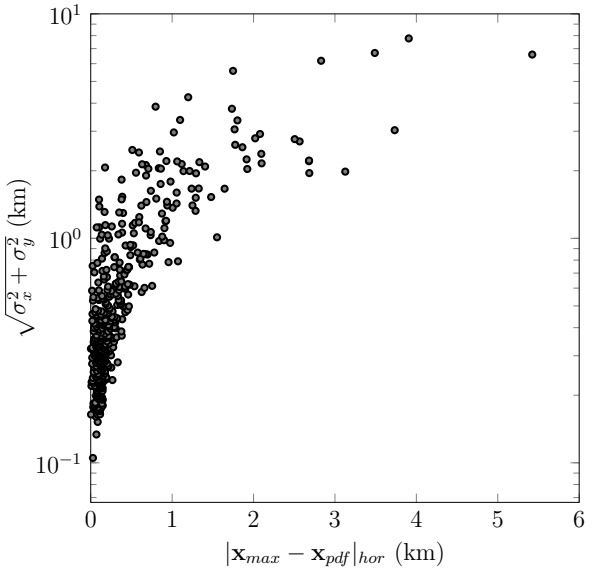

Figure 4.16: The crossplot between the distance of the statistical (pdf) and maximum (max) approches-derived event locations and the total horizontal uncertainty.

The consistency between locations computed by using the maximum (max) and statistical (pdf) approaches is shown by comparing the quantitative focusing measures ($\sqrt{\sigma_x^2+\sigma_y^2}$) with the horizontal distance between $\mathbf{x}_{pdf}$ and $\mathbf{x}_{max}$, $|\mathbf{x}_{max}-\mathbf{x}_{pdf}|$ (Figure 4.16). $\mathbf{x}_{pdf}$ and $\mathbf{x}_{max}$ are the seismic event locations estimated by the statistical and the maximum

approach, respectively. For events with small uncertainties, the distance between the statistical (pdf) and maximum (max) approaches-derived are typically small. For example, the distance between $\mathbf{x}_{pdf}$ and $\mathbf{x}_{max}$ for events with uncertainties lower than 1 km is 0.2 km (in average), which is less than the grid size (0.25 km). Note that the event locations computed by the maximum approach are located at the grid points. This finding means that if the uncertainty of a seismic event is less than 1 km, the location of the seismic event derived from the image function using the maximum and statistical approaches will be similar (very close to each other).

The located 472 events using two different approaches (the maximum and statistical image function) were compared by examining their uncertainties (Figure 4.17). Actually, the event location computed by the maximum image function does not have location uncertainty. Then, in this case, the location uncertainty was taken from the statistical approach. It can be observed that large uncertain seismic events are located in the southeastern part of the study area (around Sarulla Graben). This may be caused by a poor coverage of seismometers in this area, where seismometers were only installed between the Hutajulu and Tor Sibohi Faults (along the main Sumatran Fault). A dense network of seismometers, such as those installed in the northwest of the study area (the Tarutung basin), resulted in event locations with a small uncertainty. Thus, the location uncertainty derived from the statistical approach correlates with a relative position of seismic event to the seismic network.

Seismogram denoising using the Otsu thresholding method was then applied only to the seismograms that resulted in event locations with uncertainties greater than 1 km (see Figure 4.15). Since the number of seismic events with the location uncertainty of less than 1 km are 377, then Otsu denoising was only applied to seismograms associated with 95 seismic events. Figure 4.18 shows that Otsu thresholding was successful in removing noises that potentially introduced artifacts in the image function. These artifacts were also an indication that the focusing was unsuccessful, which would have resulted in seismic events with a very large uncertainty. After denoising, the image functions reveal better focus and the located seismic events derived from the statistical and the maximum value approaches become closer to each other.

Figure 4.19 presents the displacement of the located seismic events after applying seismogram denoising. In the northwest area, which coincides with the Tarutung Basin,

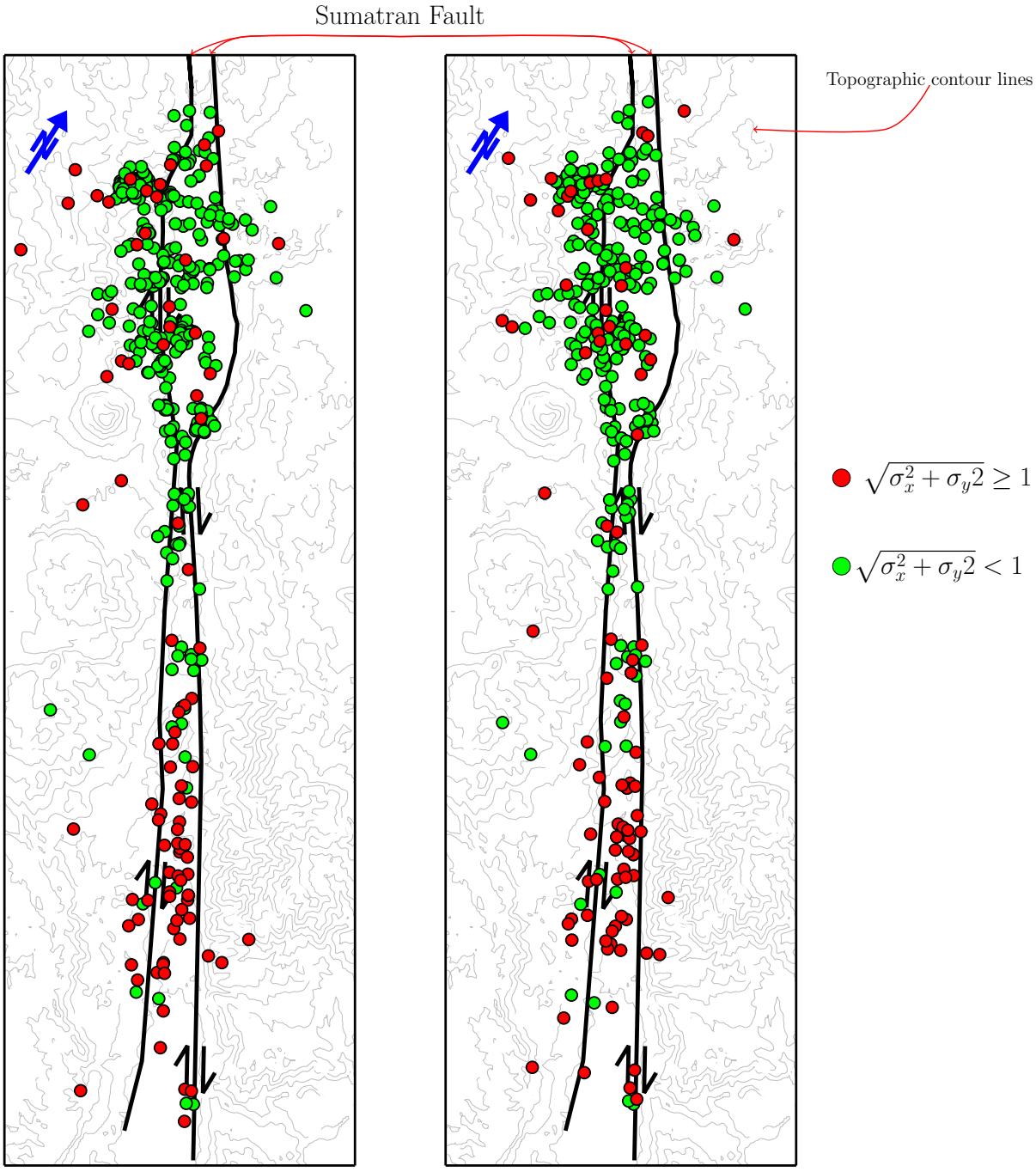

a) prob. den.func.(pdf) of image func. b) Maximum of image function (max)

Figure 4.17: Comparison of the 472 seismic events located by (a) the statistical and (b) the maximum value approaches from the unfiltered seismograms. Green points represent seismic events with uncertainties of less than 1 km and red points represent events with uncertainties of more than 1 km. Uncertainty values were derived from the statistical approach by converting an image function into a probability density function.

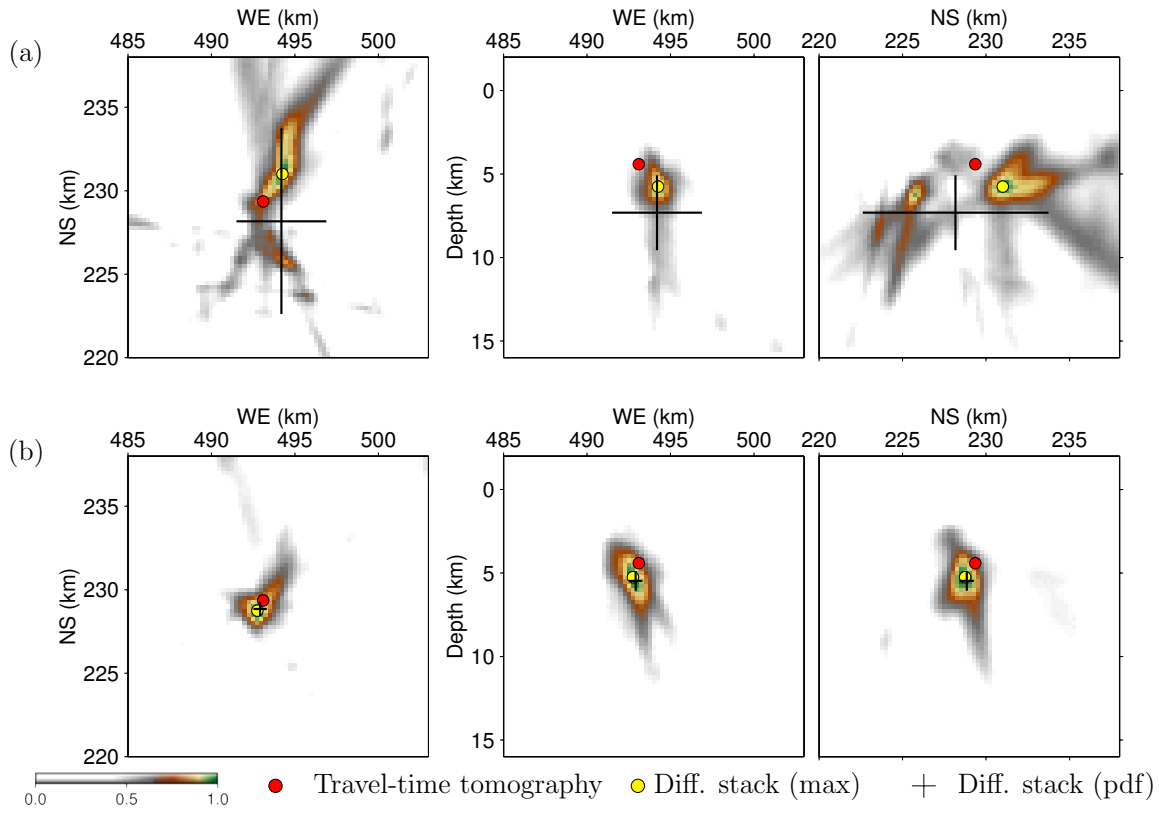

Figure 4.18: Image functions of (a) the raw seismograms and (b) seismograms filtered using Otsu thresholding. The improvements are indicated by lowering the uncertainties of the pdf seismic event location and the consistency between those resulting from travel-time-based and migration-based localization.

the seismic events resulting from raw seismograms (red), particularly those computed using the statistical approach, were displaced by a large distance after applying denoising; these approached the known western boundary fault (Hutajulu) (Figure 4.19(a)). The directions of the event location displacement might indicate that denoising was successful in improving the resulting event locations. The uncertainties of the located events were lowered, except for several event locations which are not paired (only one red dot), in the southeastern region in particular. Again, a successfull seismogram denoising was evaluated based on the location uncertainty. By ignoring located seismic events with a total horizontal uncertainty ($\sqrt{\sigma_x^2 + \sigma_y^2}$) of larger than 1 km, the total number of located seismic events now is 407. 377 seismic events were located from unfiltered velocity seismograms and additional 30 were obtained after applying seismogram denoising to velocity seismogram associated with 95 seismic events.

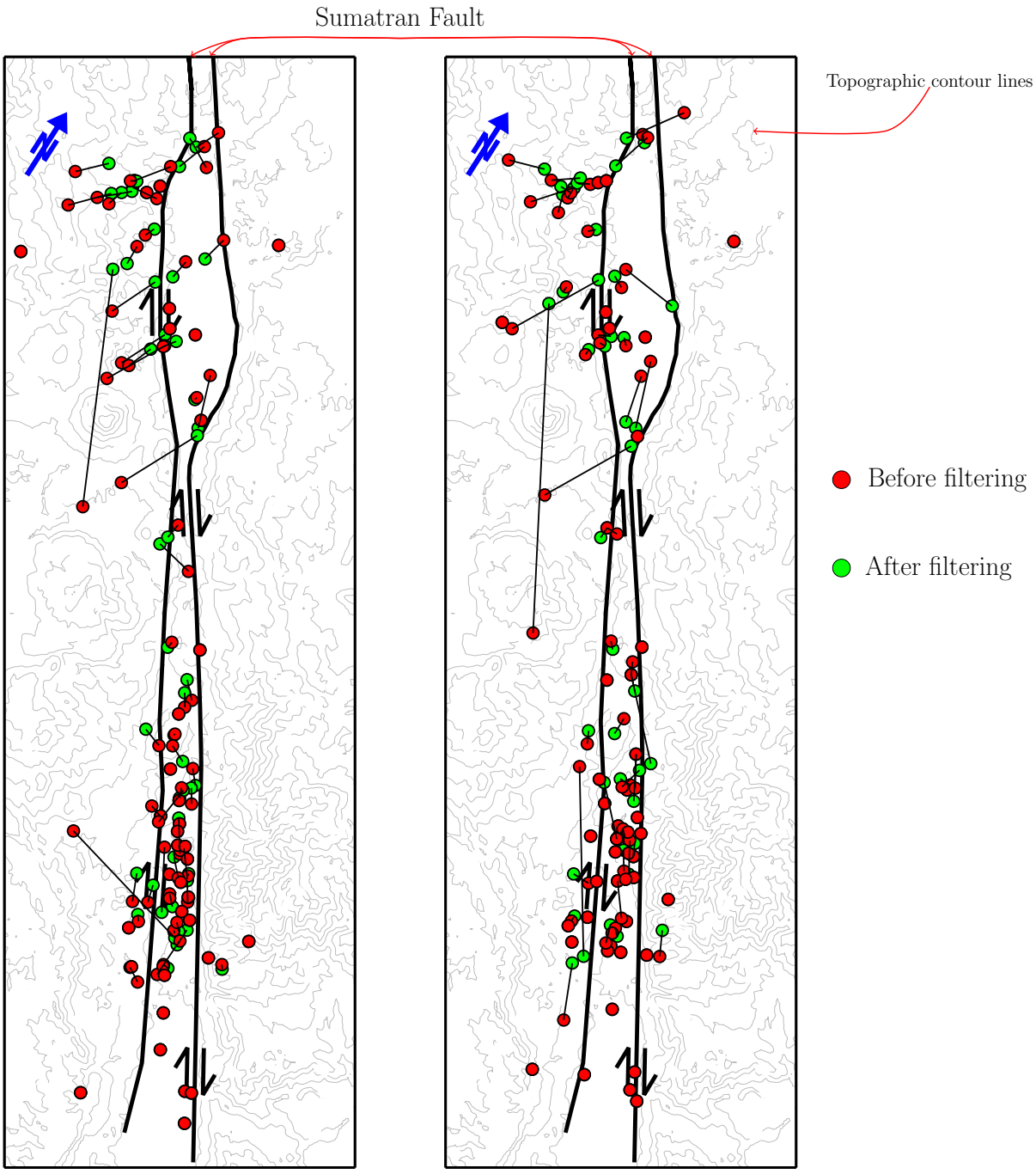

a) prob. den.func.(pdf) of image func. b) Maximum of image function (max)

Figure 4.19: 95 seismic event pairs resulted from unfiltered seismograms (red) and filtered seismograms (black). The black lines indicating a displacement of the event after filtering was applied to the seismograms.

4.4 Results

407 located seismic events are shown in Figure 4.20. Since their total horizontal uncertainties are less than 1 km, these results are considered reliable. Most of the seismic

events occurred around the western flank of the Sumatran Fault (the Hutajulu Fault). A cluster of seismic events (red circles) can also be seen in several places such as at the northwestern and southeastern boundary of the basin close to Ria Hot Springs and the Akbid (AK) travertines. Some seismic events form alignments striking NE-SW north of the Martimbang Volcano. The seismicity in the Tarutung Basin shows a more complex pattern as it is distributed not only at the surface trace of the Sumatran Fault but also scattered above the Tarutung Basin. To the south, another cluster of seismicities occur around both main fault strands close to Pianor Hot Springs, which seem to be associated with the activity of the active Hutajulu Fault.

A more detailed examination of several seismic events, were emphasized at some area denoted by A, B, C, D, and E (see Figure 4.20). A vertical distribution of seismic events were only presented for B, D and E. The vertical section of B, D and E reveal that seismic events are clustered into a narrow vertical channel which is possibly associated with a vertical fault. In box E, where 110 seismic events are located, the vertical fault is seen at the SE-NW section, which indicates that the strike's fault is SW-NE. The length of the rupture area is approximately 2 and 3 km in the horizontal and vertical axis, respectively. However, the strike of this fault is not consistent with the SE-NW Hutajulu Fault. From plain view, seismic events at cluster D organized in a narrow band striking N-S. As for box C, where 20 seismic events are located, a comparison of the vertical sections striking SE-NW and SW-NE shows that the distribution of the seismic events is restricted to a narrow vertical band (See section SE-NW). This suggests that the strike of the fault is SW-NE. The cluster of 38 seismic events in box B shows a vertical fault-like structure having a strike in the SN direction. Lastly, the distribution of seismic events in cluster A is collocated with the normal fault near travertine STP and PN. Further interpretation of the distribution of seismic event will be presented in the next chapter Discussion and Conlcusions.

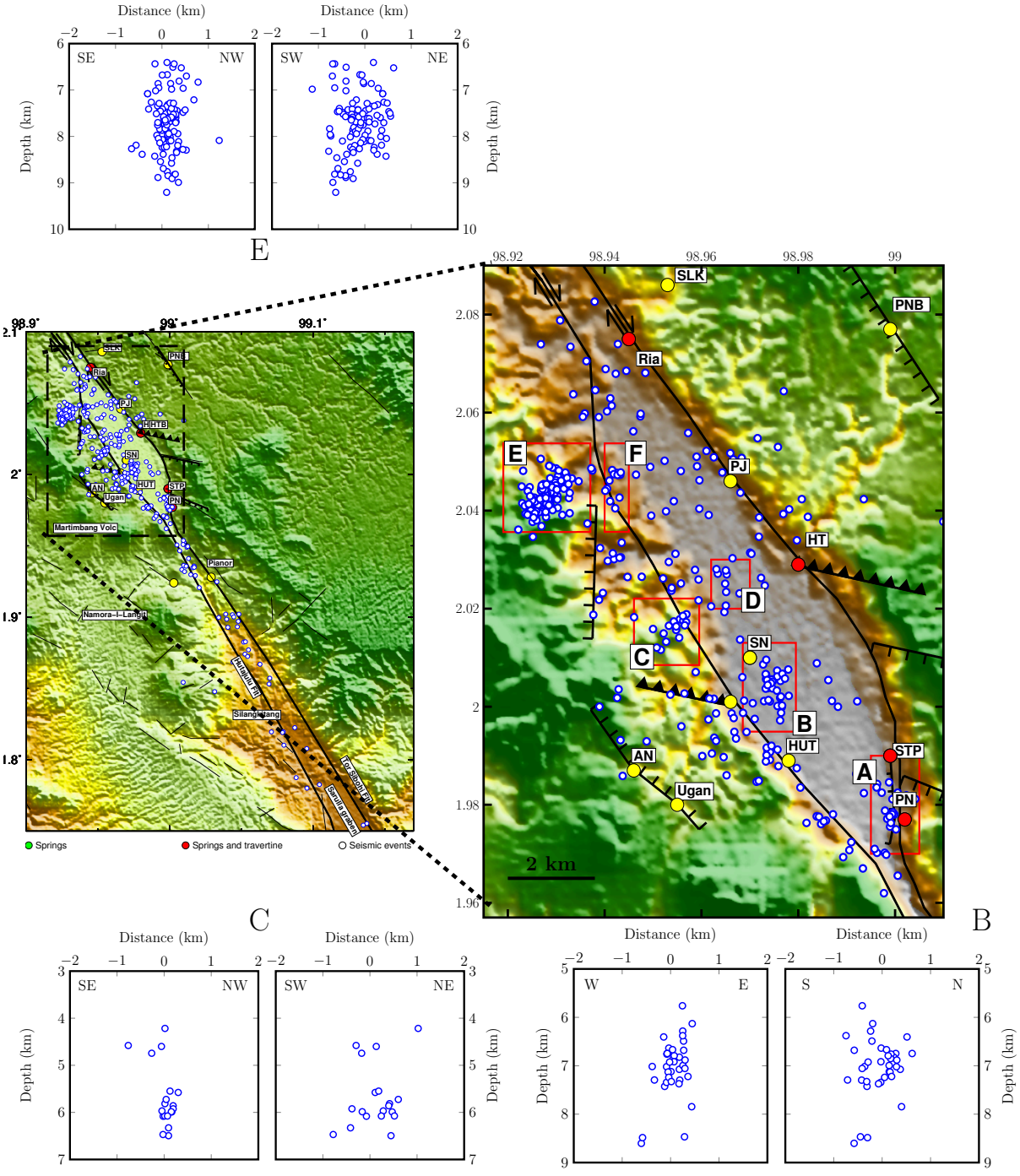

Figure 4.20: Distribution of seismic events located by the diffraction stacking method. Location of the basin boundaries, lineament, and hot springs are from Nukman & Moeck (2013), and the complex fault was derived from seismicity Muksin et al. (2014).

Chapter 5

Discussion and conclusions

5.1 Diffraction stacking workflow

I have proposed an alternative workflow for diffraction stacking localization which was tested on synthetic data and applied to real data collected over a nine-month period by a temporary seismic network around the Tarutung pull-apart Basin in northern Sumatra, Indonesia . The proposed workflow is as follows:

1. Calculate the Green Function Table (GFT) as a reference for potential travel times using parallelized code to reduce calculation time.

2. Apply Otsu Thresholding to the time-frequency amplitudes.

3. Extract the P- and S- phase characteristic functions from the filtered seismograms using polarization attributes of the multicomponent seismic records.

4. Compose an image function by computing the coherency function of each grid point based on the maximum imaging condition.

5. Combine the P- and S- image functions by extracting the largest eigenvalue from the covariance matrix.

6. Estimate the seismic event location from the image function.

To perform the diffraction stacking method based on the proposed workflow above, at least two GFTs are needed in which each corresponds to the P- and S- travel time tables. The P- and S- velocity models of the Tarutung Region resulting from the travel

time tomography (Muksin et al., 2013) were used to build the GFTs associated with the P- and S- waves. These GFTs were considered in estimating seismic event locations from both synthetic and real seismograms. Each GFT with a total grid of $241 \times 261 \times 73$ required approximately 13 hours of calculation time involving 890 cores to compute $241 \times 261 \times 73$ potential travel times, since all of the grid points represent potential locations of seismic events. In the diffraction stacking localization method, there are two main steps: preparing the GFT and creating the image function. Based on synthetic and real data application, the processing time required for computing the image functions is much lower than that required to compute the GFT. In this application, parallelized code was used for both the GFT creation and the image function computation since at present, most computers are equipped with multi-core processors.

The time-frequency denoising procedure based on the application of Otsu Thresholding has been shown to be effective in improving the accuracy of the located seismic events. The coherency of the image function derived from the filtered seismogram coalesced into one location; whereas in the image function derived from the unfiltered seismogram, the coherency function has several peaks, making the determination of seismic event locations much more difficult (see Figure 4.18). The seismic event locations resulting from the denoised seismogram show a plausible pattern since they follow known fault structures (see Figure 4.19).

As demonstrated in the synthetic examples, the recorded seismograms associated with a double-couple focal mechanism could not be processed to estimate the focal location with the diffraction stacking method. Due to a complex phase polarity of the onset of the P- and S- waves, the focal locations do not coincide with the maximum image function. To overcome this problem, a strategy using a new characteristic function instead of the original recorded seismogram was proposed. The new characteristic function was derived from the well-known AIC characteristic function (Akaike, 1973). A modified characteristic function (mAIC) was then developed to obtain reliable results independent of the choice of time window length. If the standard AIC method is applied, the length of the time window must be optimized by trial and error. Detection of P- wave arrivals with the standard AIC function requires exclusion of the S- arrival in the analyzed time window, unless the global minimum of the AIC curve coincides with the S-wave onset rather than the P-wave onset. As shown in Figure 2.18, the application of the new mAIC characteristic function

allows for the detection of both the P- and S-wave onsets without needing time-consuming tests to find the optimal time window to be analyzed. This feature is important in order to perform an automated detection of events in continuous recordings.

From the synthetic results, it is known that a unique event location could be estimated from the Z component of the seismograms associated with the CLVD source model (Figure 3.7[c]). The image function was computed from the waveforms consisting of P- and S-wave signals (Figure 3.2) by using the GFT derived from the P-wave velocity model. Nevertheless, in the resultant image function there is no indication of cross-talk artifacts. It seems that S-wave signals do not contribute to the calculated image function. The fact that the GFT was constructed using the same velocity model used in the forward modeling might be one possible explanation why the mixture between P- and S-wave signals did not happen. However, cross-talk artifacts cannot be avoided if the velocity model is not well-known, particularly in areas with complex geological structures (Artman et al., 2010). The proposed characteristic function was then split into P-phase and S-phase characteristic functions (CF^p and CF^s). Each was derived from the mAIC characteristic function by making use of the polarization attributes. The P- and S- image functions could then be computed from the P- and S- phase characteristic functions. The source location was estimated from the final image function by covariance analysis of the P- and S- image functions. The separate processing of the P- and S- waves was considered in order to mitigate the cross-talk between P- and S- signals due to inaccurate velocity models or low SNR.

The final image function is based on the largest eigenvalue of the covariance matrix between the P- and S- image functions. This approach provides a better focusing compared with the analysis of the original P- or S- image functions (Figure 4.11). The covariance analysis has successfully removed ambiguity in the P- image function. The improved image function increases the reliability of the seismic event location due to a smaller location uncertainty.

The seismic event location can be determined based on the maximum value of the image function (maximum approach) or from a deduced probability density function (statistical approach). For seismograms with high quality, both methods provided similar results as shown in Figure 4.16. However, in case of noisy seismograms, the statistical approach seems to be more robust than the maximum value approach (Table 3.2).

5.2 Discussion of results from Tarutung

By considering their horizontal uncertainties ($\sqrt{\sigma_x^2 + \sigma_y^2}$), 407 seismic events were considered as reliable results from a data set of 472 seismic events. 65 seismic events were excluded because of horizontal localization errors larger than 1 km, which is equal to four nodal grids since a grid size of 250 m was used. The rejected seismic event locations are mostly located in the southern part of the network which indicates that the failure of location determination was associated with the coverage of the seismic network. The distribution of seismic events resulting from the application of diffraction stacking is presented in Figure 5.1 (a). In general, the located seismic events are distributed along fault structures, near to hot springs and around an area of massive, fractured travertines.

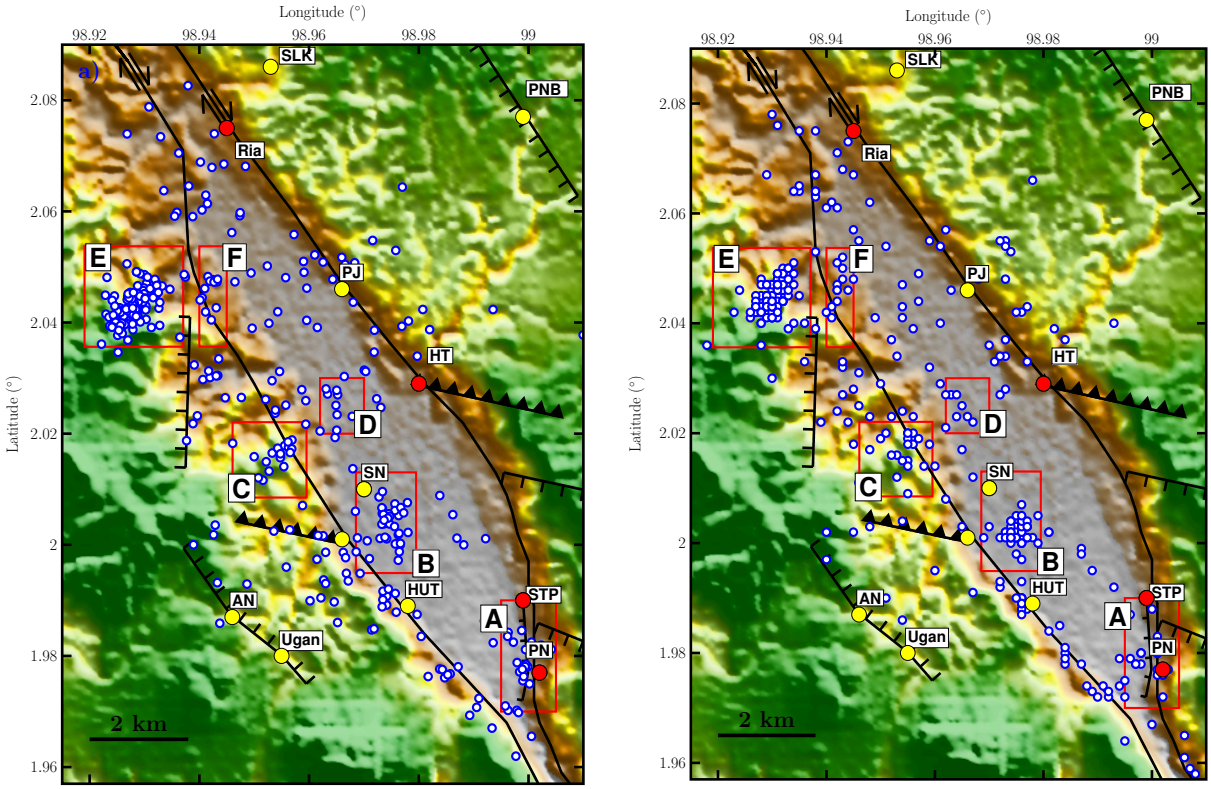

(a) Diffraction stacking

(b) Travel time tomography

Figure 5.1: Local seismicity of the study area derived from (a) diffraction stacking methods and (b) classical travel time tomography (Muksin et al., 2014) and relocation using the double-different. Seismic events are shown as white points with blue outlines. Hotspring and travertine deposits are indicated by black lines.

Figure 5.1 compares the event locations derived from the travel time based inversion and the diffraction stacking methods. Notice that the travel-time-based method consists

of the travel time tomography and the relocation using hypoDD software Muksin et al. (2013). This Figure then compares the diffraction stacking results with the relocated seismic events. In general, the event locations are consistent between those resultant from the travel-time-based method and diffraction stacking as they are located near the western fault boundary (Hutajulu Fault). A few seismic events are imaged at the eastern boundary (Tor Sibohi Fault) where prominent travertine deposits occur.

However, a more detailed examination indicates that there are differences between the results of the two methods at; for example, locations designated by A, B, C, D and E. In location A, near the travertines STP and PN, geological data indicate a normal fault striking N-S (Nukman & Moeck, 2013). The diffraction stacking results show more seismic events located above the normal fault. A lineament extending in the N-S direction in B and D are more obvious in the diffraction stacking results than in the travel-time based inversion. A cluster of seismic events can be identified at location C only by use of the diffraction stacking method. At location E, results from both methods indicate a cluster of seismic events in the SW-NE direction. At location F the travel-time based method provided more events than the diffraction stacking method. Furthermore, a N-S lineament is seen in Figure 5.1(b); whereas, in (a) the seismic events are located near the western fault boundary.

In conclusion, the application of the diffraction stacking method in local earthquake recordings from the Tarutung Basin located 407 seismic events which delineate four interesting lineaments. The lineament shown in location E is not new since it can also be seen in the travel-time-based results. Others lineaments, shown in B, C, and D, are more obvious in the diffraction stacking results (See Figure 5.2). The lineaments in B striking N-S represents extensional open fractures due to the clockwise block rotation within the actual stress field (Nukman & Moeck, 2013). Moreover, these lineaments likely connect the hotspring HUT, which are located above the active fault, with SN in the middle of the Tarutung Basin, approximately 2 km NNW from HUT. The occurrence of seismic events at cluster B are spatially and temporally very close each other (by examining the origin time resultant from the travel-time based method). The seismic events cluster in B could be a swarm indicating a development of network fractures. Thus, these seismic events might be related to the fluid flowing through this fracture network. In location D, other N-S alignment is seen that projects to the north reaching the hotsprings PJ at the

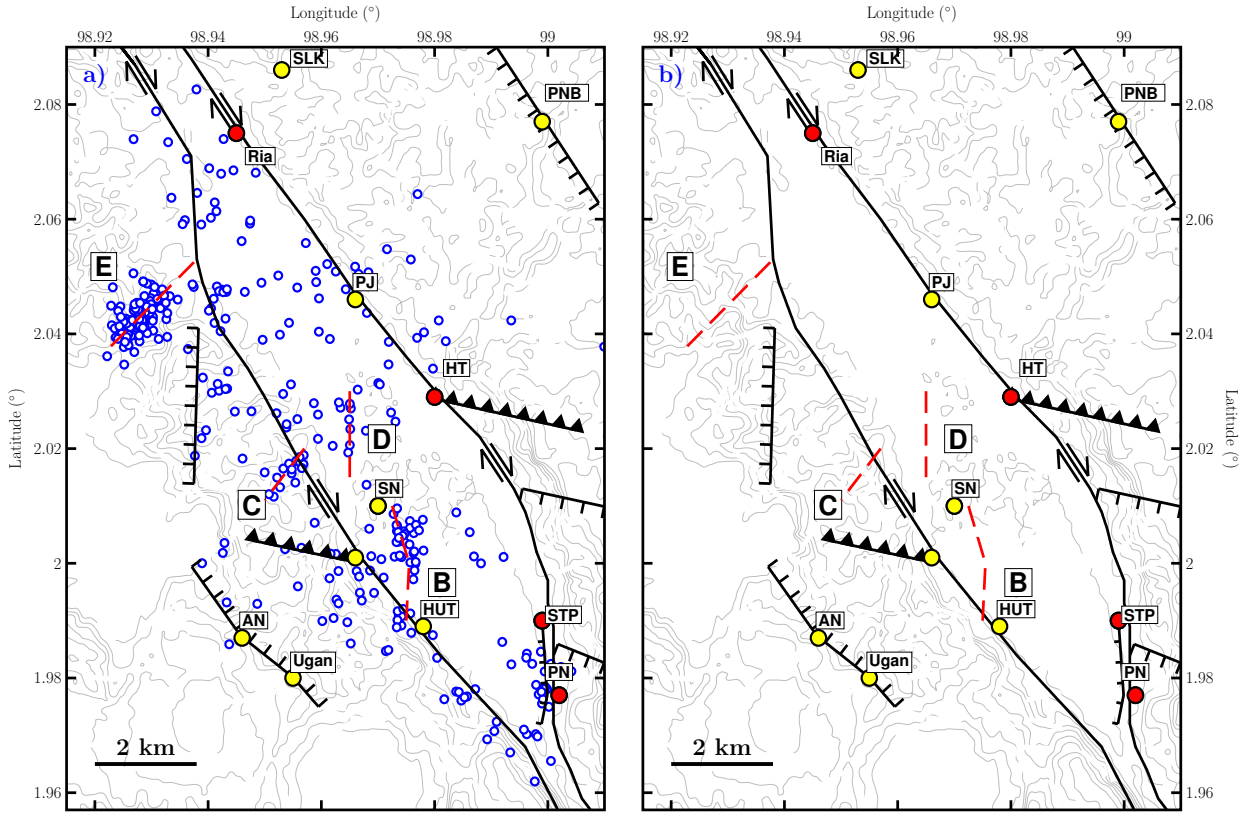

Figure 5.2: Map summarizing the geological structures discovered at the Tarutung Basin (Nukman & Moeck, 2013) and additional potential structures inferred from the distribution of seismic events as indicated by B, C, D and E. Hot springs (yellow) and travertines (red) locations originated from (Nukman & Moeck, 2013).

western fault boundary.

Figure 5.3 shows horizontal slice through the Vp model resulting from the travel time tomography (Muksin et al., 2013). The western part of the area is characterized by high Vp where the granite rocks from Sibolga Fm (Nukman & Moeck, 2013) were deposited. Superimposed on these depth slices are the event locations derived by the diffraction stacking method from depths 6.5 to 7.5 km, which reveal two clusters at locations E and B. The seismic events at cluster B and E are located at the boundary between high and low velocity. Near the location of E, collocated with the western fault boundary, the Vs image (Figure 5.3 [b]) shows lower velocity values. Since shear velocity is sensitive to fluid-filling pores, this low velocity value may indicate the presence of fluids or melts. Thus, these seismic clusters could be the result of the interaction between the western part of the study area characterized by a very tight and dry formation (Sibolga Granite), and the area characterized by more fluid-bearing or partial melts. The existence of partial

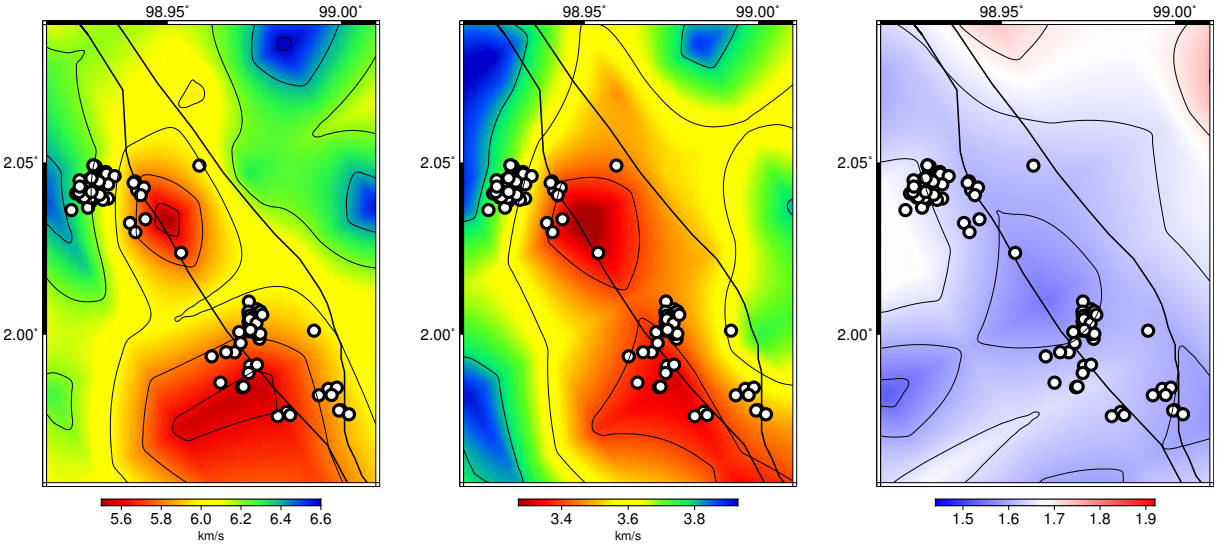

Figure 5.3: Depth slices of Vp, Vs and Vp/Vs models at a depth of 7 km (Muksin et al., 2013). The location of seismic events resultant from diffraction stacking at depths of 6.5-7.5 km are shown. White dots represent seismic events.

melts was not considered by previous studies (i.e., Niasari, 2015) due to a lack of surface manifestation such as fumaroles and acidic alteration (Nukman & Moeck, 2013). However, recent studies indicate a low velocity at shallow depths (less than 2 km), which may represent unconsolidated volcanic rock filling a collapse caldera (Ryberg et al., 2016). Thus, a low Vp, low Vs, and high Vp/Vs at deeper depths may indicate partial melted rocks as remains of previous eruptions. A frequent occurrence of earthquakes at the boundary between areas with low and high Vp/Vs has been studied by Zhao et al. (2002) and Koulakov et al. (2013).

5.3 Outlook

The method presented in my thesis was working correctly under known conditions when synthetic data were analyzed, and new information could be added in the application with real data from Indonesia. For the future, I see a large potential to make more benefit from applying the method to passive seismic data sets. A major advantage of the approach is that also weak signals can be included in the localization of seismicity even if picking is not possible because. Localization of microseismicity could be a potential application, where a large number of events with small magnitudes has to be considered. Such applications could be relevant for the monitoring of geological reservoirs, such as

in geothermal exploitation, the management of hydrocarbon reservoirs or underground storage systems.

The present version of my method is built around a Kirchhoff-type migration based on diffraction stacking. Alternative work flows could make use of other migration approaches such as time-reverse migration, or hybrid approaches where time-reverse and Kirchhoff migration are applied subsequently. The latter could be interesting in order to reduce processing time of the generally time consuming migration task.

A basic assumption of the approach is that the velocity model is already known before the migration method is applied. Future research could be carried out to develop a work flow which delivers both the velocity model and the source location from the full waveform analysis.

Bibliography

Aghayan, A., Jaiswal, P., & Siahkoohi, H. R., 2016. Seismic denoising using the redundant lifting scheme, *Geophysics*, **81**(3), V249–V260.

Akaike, H., 1973. Information theory and an extension of the maximum likelihood principle, in *2nd international symposium on information theory*, pp. 267–281, eds Petrov, B. & Csaki, F., Budapest Akademiai Kiado.

Aldiss, D. T., Whandoyo, R., Sjaefudien, A. G., & Kusjono, A., 1983. *Geological Map of Sidikalang Quadrangle (0618; Scale 1:250.000), Sumatra, Indonesia.*

Anikiev, D., Valenta, J., Staněk, F., & Eisner, L., 2014. Joint location and source mechanism inversion of microseismic events: benchmarking on seismicity induced by hydraulic fracturing, *Geophys. J. Int*, **198**, 249–258.

Apsden, J. A., Kartawa, W., Aldiss, D. T., Djunuddin, A., Whandoyo, R., Diatma, D., Clarke, M. C. G., & Harahap, H., 1982. *Geological Map of Padangsidempuan and Sibolga Quadrangle (0617-0717; Scale 1:250.000), Sumatra, Indonesia.*

Artman, B., Podladtchikov, I., & Witten, B., 2010. Source location using time-reverse imaging, *Geophys. Prosp.*, **58**, 861–873.

Baker, T., Granat, R., & Clayton, R. W., 2005. Real-time earthquake location using kirchhoff reconstruction, *Bull. seism. Soc. Am.*, **95**, 699–707.

Bellier, O. & Sébrier, M., 1994. Relationship between tectonism and volcanism along the great sumatran fault zone deduced by spot image analyses, *Tectonophysics*, **233**, 215–231.

Biondi, B. L., 2006. *3-D seismic imaging*, society of exploration geophysicist.

Bondár, I., Myers, S. C., Engdahl, E. R., & Bergman, E. A., 2004. Epicentre accuracy based on seismic network criteria, *Geophys. J. Int*, **156**, 483–496.

Briggs, R. W., Sieh, K., Meltzner, A. J., Natawidjaja, D., Galetzka, J., Suwargadi, B., ju Hsu, Y., Simons, M., Hananto, N., Suprihanto, I., Prayudi, D., Avouac, J.-P., Prawirodirdjo, L., & Bock, Y., 2006. Deformation and slip along the sunda megathrust in the great 2005 nias-simeulue earthquake, *science*, **311**, 1897–1901.

Brown, R. A., Lauzon, M. L., & Frayne, R., 2010. A general description of linear time-frequency transforms and formulation of a fast, invertible transform that samples the continuous s-transform spectrum nonredundantly, *IEEE transactions on signal processing*, **58**(1).

Canning, A. & Gardner, G. H. F., 1998. Reducing 3-d acquisition footprint for 3-d dmo and 3-d prestack migration, *Geophysics*, **63**(4), 1177–1183.

Chambers, K., Kendall, J. M., Brandsberg-Dahl, S., & Rueda, J., 2010. Testing the ability of surface arrays to monitor microseismic activity, *Geophys. Prosp.*, **58**, 821–830.

Chambers, K., Dando, B. D. E., Jones, G. A., Velasco, R., & Wilson, S. A., 2013. Moment tensor migration imaging, *Geophys. Prosp.*, pp. 1–18.

Chang, S. G., Yu, B., & Vetterli, M., 2000. Adaptive wavelet thresholding for image denoising and compression, *IEEE transactions on image processing*, **9**(9).

Claerbout, J. & Fomel, S., 2014. *Geophysical image estimation by example*, Stanford University.

Clarke, M. C. G., Ghazali, S. A., Harahap, H., Kusjono, A., & Stephenson, B., 1982. *Geological Map of Pematangsiantar Quadrangle (0718; Scale 1:250.000), Sumatra, Indonesia*.

Cohen, J. K. & Bleistein, N., 1979. Velocity inversion procedure for acoustic waves, *Geophysics*, **44**, 1077–1087.

Daubechies, I., 1990. The wavelet transform, time-frequency localization and signal analysis, *IEEE transactions on information theory*, **36**(5).

Diallo, M. S., Kulesh, M., Holschneider, M., & Scherbaum, F., 2005. Instantaneous polarization attributes in the time–frequency domain and wavefield separation, *Geophys. Prosp.*, **53**, 723–731.

Donoho, D. L. & Johnstone, I. M., 1994. Ideal spatial adaptation via wavelet shrinkage, *Biometrika*, **81**, 425–455.

Drew, J., White, R. S., Tilmann, F., & Tarasewicz, J., 2013. Coalescence microseismic mapping, *Geophys. J. Int*, **195**, 1773–1785.

Duncan, P. M. & Eisner, L., 2010. Reservoir characterization using surface microseismic monitoring, *Geophysics*, **75**(5), 75A139–75A146.

Fitch, T. J., 1972. Plate convergence, transcurrent faults and internal deformation adjacent to southeast asia and the western pacific, *J. Geophys. Res.*, **77**, 4432–4460.

Foulger, G. R., 1988. Hengill triple junction, sw iceland 2: Anomalous earthquake focal mechanisms and implications for processes within the geothermal reservoir and at accretionary plate boundaries, *jgr*, **93**, 507–523.

Gajewski, D. & Tessmer, E., 2005. Reverse modelling for seismic event characterization, *Geophys. J. Int*, **163**, 276–284.

Gajewski, D. J., Anikiev, D., Kashtan, B., Tessmer, E., & Vanelle, C., 2007. Source location by diffraction stacking, in *69th Annual Internat. Mtg., EAGE, Expanded Abstracts*, EAGE.

Gharti, H. N., Oye, V., Roth, M., & Kühn, D., 2010. Automated microearthquake location using envelope stacking and robust global optimization, *Geophysics*, **75**, M27–M46.

Grigoli, F., Cesca, S., Vassallo, M., & Dahm, T., 2013. Automated seismic event location by travel-time stacking: an application to mining induced seismicity, *Seism. Res. Lett.*, **84**(4), 666–677.

Grigoli, F., Cesca, S., Amoroso, O., Emolo, A., Zollo, A., & Dahm, T., 2014. Automated seismic event location by waveform coherence analysis, *Geophys. J. Int*, **196**, 1742 – 1753.

Gutenberg, B. & Richter, C. F., 1954. *Seismicity of the Earth and Associated Phenomena*, Princeton University Press, 2nd edn.

Hansen, S. M. & Schmandt, B., 2015. Automated detection and location of microseismicity at mount st. helens with a large-n geophone array, *Geophys. Res. Lett.*, **42**, 7390–7397.

Hickman, R. G., Dobson, P. F., van Gerven, M., Sagala, B. D., & Gunderson, R. P., 2004. Tectonic and stratigraphic evolution of the sarulla graben geothermal area, north sumatra, indonesia, *Journal of Asian Earth Sciences*, **23**, 435–448.

Hinze, W. J., 2003. Bouguer reduction density, why 2.67?, *Geophysics*, **68**(5), 1559–1560.

Houlié, N. & Montagner, J.-P., 2007. Hidden dykes detected on ultra long period seismic signals at piton de la fournaise volcano?, *Earth Planet. Sci. Lett.*, **261**.

Jousset, P., Haberland, C., Bauer, K., & Arnason, K., 2011. Hengill geothermal volcanic complex (iceland) characterized by integrated geophysical observations, *geothermics*, **40**, 1–24.

Julian, B. R., 1983. Evidence for dyke intrusion earthquake mechanisms near long valley caldera, california, *Nature*, **303**, 323–325.

Julian, B. R., Miller, A. D., & Foulger, G. R., 1997. Non-double-couple earthquake mechanisms at the hengill-grensdalur volcanic complex, southwest iceland, *Geophys. Res. Lett.*, **24**, 743–746.

Julian, B. R., Miller, A. D., & Foulger, G. R., 1998. Non-double-couple earthquakes, 1. theory, *Rev. Geophys*, **36**, 525–549.

Julian, B. R., Foulger, G. R., & Monastero, F., 2007. Microearthquake moment tensors from the coso geothermal area, in *Proceedings of 32nd Workshop on Geothermal Reservoir Engineering*, Stanford University.

Jurkevics, A., 1988. Polarization analysis of three-component array data, *Bull. seism. Soc. Am.*, **78**, 1725–1743.

Kao, H. & Shan, S.-J., 2004. The source-scanning algorithm: mapping the distribution of seismic sources in time and space, *Geophys. J. Int*, **157**, 589–594.

Kao, H. & Shan, S.-J., 2007. Rapid identification of earthquake rupture plane using source-scanning algorithm, *Geophys. J. Int*, **168**, 1011–1020.

Komatitsch, D. & Tromp, J., 2002. Spectral-element simulations of global seismic wave propagation-i. validation, *gji*, **149**, 390–412.

Koulakov, I., West, M., & Izbekov, P., 2013. Fluid ascent during the 2004–2005 unrest at mt. spurr inferred from seismic tomography, *Geophys. Res. Lett.*, **40**, 4579–4582.

Kubas, A. & Sipkin, S. A., 1987. Non-double-couple earthquake mechanisms in the nazca plate subduction zone, *grl*, **14**(4), 339–342.

Lakings, J. D., Duncan, P. M., Neale, C., & Theiner, T., 2006. Surface based microseismic monitoring of a hydraulic fracture well stimulation in the barnett shale, in *New Orleans Annual International Meeting, SEG, Expanded Abstracts*, SEG.

Langet, N., Maggi, A., Michelini, A., & Brenguier, F., 2014. Continuous kurtosis-based migration for seismic event detection and location, with application to piton de la fournaise volcano, la réunion, *Bull. seism. Soc. Am.*, **104**(1), 229 – 246.

Lay, T., Kanamori, H., Ammon, C. J., Nettles, M., Ward, S. N., Aster, R. C., Beck, S. L., Bilek, S. L., Brudzinski, M. R., Butler, R., DeShon, H. R., Ekström, G., Satake, K., & Sipkin, S., 2005. The great sumatra-andaman earthquake of 26 december 2004, *Science*, **308**, 1127–1132.

Lomax, A., Virieux, J., Voulant, P., & Berge-Thierry, C., 2000. in *Advances in seismic event location*, chap. Probabilistic earthquake location in 3D and layered models: introduction of a metropolis-Gibbs method and comparison with linear locations, pp. 101–134, Kluwer Academic publisher.

Lomax, A., Satriano, C., & Vassalo, M., 2012. Automatic picker developments and optimization: filterpicker-a robust, broadband picker for real time seismic monitoring and earthquake early warning, *Seism. Res. Lett.*, **83**, 531–540.

Maeda, N., 1985. A method for reading and checking phase times in autoprocessing system of seismic wave data, *Jishin*, **38**, 365–379.

Marsaglia, G. & Tsang, W. W., 1984. A fast, easily implemented method for sampling from decreasing or symmetric unimodal density functions, *SIAM J. Sci. and Stat. Comput.*, **5 (2)**, 349–359.

Montalbetti, J. F. & Kanasewich, E. R., 1970. Enhancement of teleseismic body phases with a polarization filter, *Geophys. J. R. astr. Soc*, **21**, 119–129.

Muksin, Bauer, K., & Haberland, C., 2013. Seismic vp and vp/vs structure of the geothermal area around tarutung (north sumatra, indonesia) derived from local earthquake tomography, *Journal of volcanology and geothermal research*, **260**, 27–42.

Muksin, U., 2014. A fault-controlled geothermal system in tarutung (north sumatra, indonesia) investigated by seismological analysis, Scientific technical report 14/14, GFZ German Research Centre for Geosciences.

Muksin, U., Haberland, C., Nukman, M., Bauer, K., & Weber, M., 2014. Detailed fault structure of the tarutung pull-apart basin in sumatra, indonesia, derived from local earthquake data, *Journal of Asian Earth Sciences*, **96**, 123–131.

Muraoka, H., Takashi, M., Sundhoro, H., Dwipa, S., Soeda, Y., Momita, M., & Shimada, K., 2010. Geothermal systems constrained by the sumatra fault and its pull-apart basins in sumatra, western indonesia, in *World Geothermal Congress*, pp. 1–9, Bali, Indonesia.

Niasari, S. W., 2015. *Magnetotelluric Investigation of the Sipoholon Geothermal Field, Indonesia*, Ph.D. thesis, Frei Universität.

Nukman, M. & Moeck, I., 2013. Structural controls on a geothermal system in the tarutung basin, north central sumatra, *Journal of Asian earth sciences*, **74**, 86–96.

Otsu, N., 1979. A threshold selection method from gray-level histograms, *EEE TRANSACTIONS ON SYSTREMS, MAN, AND CYBERNETICS*, **SMC-9**(1).

Park, J., Song, T. R. A., Tromp, J., Okal, E., Stein, S., Roult, G., Clevede, E., Laske, G., Kanamori, H., Davis, P., Berger, J., Braitenberg, C., Camp, M. V., Lei, X., Sun, H., Xu, H., & Rossat, S., 2005. Earth's free oscillations excited by the 26 december 2004 sumatra-andaman earthquake, *science*, **308**, 1139–1144.

Podvin, P. & Lecomte, I., 1991. Finite-difference computation of traveltimes in very contrasted velocity models: A massively parallel approach and its associated tools, *Geophys. J. Int*, **105**, 271–284.

Prawirodirdjo, L. & Bock, Y., 2004. Instantaneous global plate motion model from 12 years of continuous gps observations, *J. Geophys. Res.*, **109**(B08405).

Reid, H. F., 1913. Sudden earth-movements in sumatra in 1892, *Bull. seism. Soc. Am.*, **3**, 72–79.

Reshetnikov, A., 2013. *Microseismic reflection imaging*, Ph.D. thesis, Frei Universität.

Ross, A., Foulger, G. R., & Julian, B. R., 1999. Source processes of industrially-induced earthquakes at the geyser geothermal area, california, *Geophysics*, **64**(6), 1877–1889.

Ross, Z. E. & Ben-Zion, Y., 2014. Automatic picking of direct p, s seismic phases and fault zone head waves, *Geophys. J. Int*, **199**, 368–381.

Ryberg, T., Muksin, U., & Bauer, K., 2016. Ambient seismic noise tomography reveals a hidden caldera and its relation to the tarutung pull-apart basin at the sumatran fault zone, indonesia, *Journal of volcanology and geothermal research*, **321**, 73–84.

Schafer, R. W. & Rabiner, L. R., 1973. Design and simulation of a speech analysis-synthesis system based on short-time fourier analysis, *IEEE transactions on audio and electroacoustics*, **Au-21**(3).

Schleicher, J., Tygel, M., & Hubral, P., 1993. 3-d true amplitude finite-offset migration, *Geophysics*, **58**, 1112–1126.

Schneider, W. A., 1978. Integral formulation of migration in two and three dimensions, *Geophysics*, **43**, 49–76.

Sethian, J. A. & Popovici, A. M., 1999. 3-d traveltime computation using the fast marching method, *Geophysics*, **64**(2), 516–523.

Sieh, K. & Natawidjaja, D., 2000. Neotectonics of the sumatran fault, indonesia, *J. Geophys. Res.*, **105**(B12), 295–326.

Staněk, F., Anikiev, D., Valenta, J., & Eisner, L., 2015. Semblance for microseismic event detection, *Geophys. J. Int*, **201**, 1362–1369.

Steiner, B., Saenger, E. H., & Schmalholz, S. M., 2008. Time reverse modeling of low-frequency mictotremors: application to hydrocarbon reservoir localization, *Geophy. Res. Lett.*, **35**, L03307.

Stierle, E., Bohnhoff, M., & Vavryčuk, V., 2014. Resolution of non-double-couple components in the seismic moment tensor using regional networks—ii: application to aftershocks of the 1999 mw 7.4 izmit earthquake, *Geophys. J. Int*, **196**, 1878–1888.

Stockwell, R. G., Mansinha, L., & Lowe, R. P., 1996. Localization of the complex spectrum: the s transform, *IEEE transactions on signal processing*, **44**(4).

Takagishi, M., Hashimoto, T., Horikawa, S., Kusunose, K., Xue, Z., & Hovorka, S. D., 2014. Microseismic monitoring at the large-scale co 2 injection site, cranfield, ms, usa, *Energy Procedia*, **63**, 4411–4417.

Tarantola, A., 2005. *Inverse problem theory and model parameter estimation*, SIAM.

Thurber, C. H., 1983. Earthquake locations and three-dimensional crustal structure in the coyote lake area, central california, *J. Geophys. Res.*, **88**(B10), 8226 – 8236.

Tromp, J., Komatitsch, D., & Liu, Q., 2008. Spectral-element and adjoint methods in seismology, *Communications in computational physics*, **3**, 1–32.

Tryggvason, A. & Bergman, B., 2006. A traveltime reciprocity discrepancy in the podvin & lecomte *time3d* finite difference algorithm, *Geophys. J. Int*, **165**, 432–435.

Tselentis, G.-A., Martakis, N., Paraskevopoulos, P., Lois, A., & Sokos, E., 2012. Strategy for automated analysis of passive microseismic data based on s-transform, otsu's thresholding, and higher order statistics, *Geophysics*, **77**(6), KS43–KS54.

Vaezi, Y. & der Baan, M. V., 2015. Comparison of the sta/lta and power spectral density methods for microseismic event detection, *Geophys. J. Int*, **203**, 1896–1908.

van Trier, J. & Symes, W., 1991. Upwind finite difference calculation of traveltimes, *Geophysics*, **56**, 812–821.

Vavryčuk, V., 2015. Moment tensor decompositions revisited, *J Seismol*, **19**, 231–252.

Vidale, J., 1988. Finite-difference calculation of travel times, *Bull. seism. Soc. Am.*, **78**(6), 2062–2076.

Vinje, V., Iversen, E., & Gjoystdal, H., 1993. Traveltime and amplitude estimation using wavefront construction, *Geophysics*, **58**, 1157–1166.

Waldhauser, F. & Ellsworth, W. L., 2000. A double-difference earthquake location algorithm: Method and application to the northern hayward fault, california, *Bull. seism. Soc. Am.*, **90**, 1353–1368.

Weller, O., Lange, D., Tilmann, F., Natawidjaja, D., Rietbrock, A., Collings, R., & Gregory, L., 2012. The structure of the sumatran fault revealed by local seismicity, *Geophys. Res. Lett.*, **39**(L01306).

Zhao, D., Mishra, O. P., & Sanda, R., 2002. Influence of fluids and magma on earthquakes: seismological evidence, *Physics of the earth and planetary interiors*, **132**, 249–267.

Zhebel, O., 2013. *Imaging of seismic event. The role of imaging conditions, acquisition geometry and source mechanisms*, Ph.D. thesis, University of Hamburg.

List of Figures

List of Tables

Mathematical derivation of α domain

Recalling Eq. 2.7

$$\alpha(f', f) = \int_{-\infty}^{\infty} S(\tau, f) \exp\left[-i2\pi f'\tau\right] d\tau \tag{1}$$

S-transform is defined as (Eq. 2.3),

$$S(\tau, f) = \int_{-\infty}^{\infty} x(t) \frac{|f|}{\sqrt{2\pi}} \exp\left[-\frac{(\tau - t)^2 f^2}{2}\right] \exp\left[-i2\pi f t\right] dt \tag{2}$$

Inserting S-transform equation into α-equation would be obtained,

$$\alpha(f', f) = \int_{-\infty}^{\infty} \left\{ \int_{-\infty}^{\infty} x(t) \frac{|f|}{\sqrt{2\pi}} \exp\left[-\frac{(\tau - t)^2 f^2}{2}\right] \exp\left[-i2\pi f t\right] dt \right\} \exp\left[-i2\pi f'\tau\right] d\tau \tag{3}$$

$$\alpha(f', f) = \int_{-\infty}^{\infty} x(t) \exp\left[-i2\pi f t\right] \left\{ \int_{-\infty}^{\infty} \frac{|f|}{\sqrt{2\pi}} \exp\left[-\frac{(\tau - t)^2 f^2}{2}\right] \exp\left[-i2\pi f'\tau\right] d\tau \right\} dt \tag{4}$$

By introducing $T = \tau - t$, then

$$\alpha(f', f) = \int_{-\infty}^{\infty} x(t) \exp\left[-i2\pi f t\right] \left\{ \int_{-\infty}^{\infty} \frac{|f|}{\sqrt{2\pi}} \exp\left[-\frac{T^2 f^2}{2}\right] \exp\left[-i2\pi f'(T + t)\right] dT \right\} dt \tag{5}$$

$$\alpha(f', f) = \int_{-\infty}^{\infty} x(t) \exp\left[-i2\pi (f + f')t\right] \left\{ \int_{-\infty}^{\infty} \frac{|f|}{\sqrt{2\pi}} \exp\left[-\frac{T^2 f^2}{2}\right] \exp\left[-i2\pi f' T\right] dT \right\} dt \tag{6}$$

The window function in S transform is normalized Gaussian function,

$$w(t, f) = \frac{|f|}{\sqrt{2\pi}} \exp\left[-\frac{t^2 f^2}{2}\right] \tag{7}$$

$$\alpha(f', f) = \int_{-\infty}^{\infty} x(t) \exp\left[-i2\pi (f + f')t\right] W(f', f) dt \tag{8}$$

$$\begin{aligned}\alpha(f', f) &= W(f', f) \int_{-\infty}^{\infty} x(t) \exp\left[-i2\pi(f + f')t\right] dt \\ &= W(f', f) X(f + f')\end{aligned} \tag{9}$$

Program for determination of Otsu's threshold

The following code is program to compute an optimal threshold which could be used to separate signal and noise from time-frequency section. The C was written in C. The program uses library from seismic unix. To compile the code :

```
gcc -I$CWPROOT/include otsuthreshold.c -L$CWPROOT/lib -lsu -lpar -lcwp -o otsuthresho
```

.

The input are :

- S-spectra (in SU format data)
- minimum and maximum class of histogram of the S-spectra
- number of bins

The output of this program is optimal threshold.

```
#include "su.h"
#include "segy.h"
#include "header.h"

char *sdoc[] = {
"otsuthres",
"",
"",
"Potsdam, 13.06.16",
NULL};
```

```
segy tr;

int main(int argc, char **argv)
{

  int nt;
  float min, max;
  int nbins;
  float bin;
  int it;
  int *histogram;
  int j;
  int total=0;
  float sum;
  float sumB, varMax,mB,mF,varBetween;
  int wB, wF, threshold;

  initargs(argc, argv);
  requestdoc(1);

  if (!gettr(&tr)) err("reading file was failed..");
  if (!getparfloat("max",&max)) err("max=.. max s-spectra (for histogram)");
  if (!getparfloat("min",&min)) err("min=.. min s-spectra (for histogram)");
  if (!getparint("nbins",&nbins)) err("nbins=?  number of bins..");

  nt = tr.ns;
  bin = (max-min)/nbins;

  histogram = (int*) malloc(nbins*sizeof(int));
  memset (histogram, 0, nbins*sizeof(int));
```

```
//creating histogram
do {

  for (it=0; it<nt; it++){
     j = (tr.data[it]-min)/bin;
     j = j<0 ? 0 : j;
     j = j>nbins-1 ? nbins-1 : j;
     histogram[j]++;
     total++;
  }

} while (gettr(&tr));

//otsu:
//following is taken from:
////http://www.labbookpages.co.uk/software/imgProc/otsuThreshold.html
//*****************************************************************
sum = 0;
for (it=0 ; it<nbins ; it++) sum += it * histogram[it];

sumB = 0;
wB = 0;
wF = 0;
varMax = 0;
threshold = 0;

for (it=0 ; it<nbins ; it++) {
  wB += histogram[it];               // Weight Background
  if (wB == 0) continue;

  wF = total - wB;                 // Weight Foreground
  if (wF == 0) break;
```

```
    sumB += (float) (it * histogram[it]);

    mB = sumB / wB;            // Mean Background
    mF = (sum - sumB) / wF;    // Mean Foreground

    // Calculate Between Class Variance
    varBetween = (float)wB * (float)wF * (mB - mF) * (mB - mF);

    // Check if new maximum found
    if (varBetween > varMax) {
       varMax = varBetween;
       threshold = it;
    }
  }

////*********************************************************
  printf("t*: %10.4f\n",min+threshold*bin);

  free(histogram);

  return (CWP_Exit());
}
```

Acknowledgement

I would like to express my gratitude to all people who contributed to the work presented in this thesis. Foremost, I am grateful to my academic advisor Professor Michael Weber for accepting me as one of his PhD student since 2012 and for giving me supervision. I would like also to thank Dr. Klaus Bauer for giving me lots of advice, continuous supports, countless help, and also supervision. I would like to thank Prof. Charlotte Krawczyk for hosting me in GFZ-Potsdam. Special thanks also to Dr. Makky Jaya who brought me to involve in research with GFZ Potsdam team and for supervision you gave me between 2012-2014. I would like to thank Dr. Trond Ryberg and Dr. Christian Haberland for the feedback and discussion a couple of days before my defense.

I would like to acknowledge Indonesian Ministry of Higher Education for giving a scholarship to conduct PhD research. My great appreciation also for Professor Ernst Huenges for hosting me as PhD student in International Centre for Geothermal Research ICGR. Additionally, I would like to thank to Dr. Kemal Erbas and Professor David Bruhn for any kind of support and encouragement.

My great gratitude expressed to Dr. Rachmat Sule for endless series of supports particularly since 2005 when I was Bachelor student at ITB. Last but not least I would like to thank my parents for supporting spiritually.